Oxide Supported Transition Metal Chalcogenides for Solar Applications

A thesis submitted to the University of Manchester for the degree of Master of Philosophy in the Faculty of Science and Engineering

2019

Qiaotian Guan

School of Natural Sciences

Department of Materials

Contents

Final word count: 26440 words

List of figures

List of tables

List of Equations

List of abbreviation

2D	2-dimensional
ACN	acetonitrilelayer
ALD	atomic deposition
AM	air mass
BE	binding energy
CB	chlorobenzene
CBD	chemical bath deposition
CBO	conduction band offset
CIGS	$CuIn_xGa_{(1-x)}Se_2$
CVD	chemical vapour deposition
DC	direct current
DSSC	dye sensitised solar cell
EDX	energy dispersive X-ray spectroscopy
EJ	exajoule
FAT	fixed analyser transmission
FF	fill factor
FRR	fixed retard ratio
FTO	fluorine doped tin oxide
FWHM	full width at half maximum
HOMO	highest occupied molecular orbital
HSC	heterojunction solar cell
IPA	isopropanol
ITO	indium tin oxide
LINAC	linear accelerator
Li-TFSI	lithium bis-trifluoromethanesulfonimide
LUMO	lowest unoccupied molecular orbital
MPP	maximum power point
NMP	N-methylpyrrolidone
OR	orthorhombic
P3HT	poly(3-hexylthiophene)
PCE	power conversion efficiency
PES	photoelectron spectroscopy
PV	photovoltaic
RF	radio frequency
RTA	rapid thermal annealing
SEM	scanning electron microscope
Spiro-MeOTAD	2,2’,7,7’-tetrakis-(N,N-di-4-methoxyphenylamino)-9,9’-spirobifluorene
STC	standard test condition
TBP	4-tert-butylpyridine
TCO	transparent conducting oxides
TEM	transmission electron microscope
TMDC	transition metal dichalcogenides
UHV	ultra-high vacuum
UN	United Nation
UPS	ultraviolet photoemission spectroscopy
UV-Vis	ultraviolet-visible spectroscopy

VE	vacuum evaporation
XRD	X-ray diffraction
ZB	zinc blende

Abstract

Since the advent of the industrial revolution, emissions of CO_2 and other greenhouse gases have led to a substantial increase in global temperatures. As a result, and to avoid further warming, people have been seeking clean and renewable energy resources to reduce carbon emission. One of the options is to utilise solar energy by converting it directly to electricity using photovoltaic (PV) cells. In addition, solar energy can be used to catalyse the splitting of water to provide hydrogen as a fuel. Transition metal chalcogenides (TMC) materials exhibit great potential in photovoltaic and photocatalytic applications because of their low cost, abundance, and non-toxicity. In this project, TMC thin layers were deposited onto the surface of mesoporous/compact TiO_2 thin films on ITO glass using a dip-coating method. The effect of dip-coating time length on the performance of prototype cells based on SnS/TiO_2 structure was investigated. NMP and IPA were used as solvents of the TMC suspensions in the dip coating process and the different impact each solvent has to the dip coating process was investigated. MoS_2 + WS_2 which have been widely studied for photocatalytic water splitting were also studied following attachment to TiO_2 films. Here, it was found that oxidation of the TMC occurs in ambient conditions.

Declaration

No portion of the work referred to in the thesis has been submitted in support of an application for another degree or qualification of this or any other university or other institute of learning.

Copyright Statement

i. The author of this thesis (including any appendices and/or schedules to this thesis) owns certain copyright or related rights in it (the "Copyright") and s/he has given The University of Manchester certain rights to use such Copyright, including for administrative purposes.

ii. Copies of this thesis, either in full or in extracts and whether in hard or electronic copy, may be made **only** in accordance with the Copyright, Designs and Patents Act 1988 (as amended) and regulations issued under it or, where appropriate, in accordance with licensing agreements which the University has from time to time. This page must form part of any such copies made.

iii. The ownership of certain Copyright, patents, designs, trademarks and other intellectual property (the "Intellectual Property") and any reproductions of copyright works in the thesis, for example graphs and tables ("Reproductions"), which may be described in this thesis, may not be owned by the author and may be owned by third parties. Such Intellectual Property and Reproductions cannot and must not be made available for use without the prior written permission of the owner(s) of the relevant Intellectual Property and/or Reproductions.

iv. Further information on the conditions under which disclosure, publication and commercialisation of this thesis, the Copyright and any Intellectual Property and/or Reproductions described in it may take place is available in the University IP Policy (see http://documents.manchester.ac.uk/DocuInfo.aspx?DocID=24420), in any relevant Thesis restriction declarations deposited in the University Library, The University Library's regulations (see http://www.library.manchester.ac.uk/about/regulations/) and in The University's policy on Presentation of Theses

Acknowledgement

I'd like to show appreciation to my main supervisor Dr. Andrew Thomas for giving me guidance and support continuously during my two-year course, and my co-supervisor Dr. David Lewis and Dr. Zhu Liu for their help with my project. Thank you to Chun-ren, Rosie, Claudia, Qian Chen, Dong Wang and Tong Bie for all the assistance to finish my thesis. Thanks to all my friends who gave me comfort and courage when I was struggling.

I would also like to say thank you to my family who supported my decisions and paid my tuition fees generously.

1 Introduction

1.1 Energy crisis and greenhouse effect

The increasing world population is demanding an increasing supply of energy. In the modern world, most of the energy supplies come from fossil fuels, which emit carbon dioxide to the atmosphere during combustion processes. The increasing CO_2 concentration in the atmosphere had already led to a 0.6°C increase in the global temperature by the end of 20th century, due to the "greenhouse effect"[1]. At the UN Climate Change Conference held in Paris in 2015, 195 countries agreed to reduce emissions of CO_2 and other greenhouse gases, and the goal were set to limit global temperature increase to below 2°C[1]. To achieve this aim, new energy technologies which provide clean, environment-friendly, renewable and low-cost energy need to be developed as replacement of fossil fuels[2].

1.2 Solar energy

Solar energy is an ideal replacement of fossil fuels due to its availability and richness. According to the report of United Nations Development Programme in the 2000 World Energy Assessment, the annual potential of solar energy was 1,575–49,837 exajoules (EJ). This is several times larger than the total world energy consumption which was 559.8 EJ in 2012[3]. One of the most commonly used approaches to collect and utilise solar energy is to convert it into electricity using solar cells.

1.3 Solar cells

A solar cell, or a photovoltaic cell, is a device which directly converts the energy of light into electricity through the photovoltaic effect[4]. Solar cells can be fabricated from various materials, such as amorphous silicon, crystalline silicon, CdTe, $CuIn_xGa_{(1-x)}Se_2$ (CIGS), III-V, and II-VI semiconductors. Solar cells are usually classified into first,

second and third generation. First-generation solar cells are made of silicon. They are relatively highly efficient with respect to their price, which makes them currently the most widely used solar cells for residential use. However, the recycling of used PV panels will become a challenge for waste treatment plants in the future[5]. Second-generation solar cells are called thin film solar cells because they are composed of thin layers of semiconductor materials only several micrometres in thickness[6]. The materials that are selected for making second-generation solar cells usually include amorphous silicon, CdTe and CIGS. Thin film solar cells have high efficiency, but the manufacturing costs are very high. Therefore, with respect to their price, the efficiency is low. Additionally, the toxicity of materials commonly used for producing thin film cells is a severe problem considering the potential damage they might do to the environment. Third-generation solar cells refer to the cells still in the stage of research and not yet commercially applied. Third-generation solar cells are made from varieties of new materials, for instance, nanostructured materials, organic dyes, and conductive polymers[6].

1.4 Transition-metal-chalcogenides for solar applications

As mentioned in Section 1.3, commercial solar cells nowadays have already reached a good light to electricity conversion efficiency, but the materials are usually either toxic or non-recyclable. In recent years, TMCs have received significant interest due to their unique properties. TMCs exhibit great potential in the photovoltaic applications because of their low cost, abundance, and non-toxicity. Moreover, the stability of TMCs allow the solar cells based on them to have potentially a relatively long lifespan, compared to other PV materials (e.g. organic photovoltaics and lead perovskites)[7]. Classic TMC photovoltaics centred on the Cd(S,Se) family, as well as CIGS, which have already been proven in the laboratory to exhibit better performance, but the use of

cadmium is not ideal due to its toxicity[8]. CIGS has a low toxicity, however, in terms of the world-wide supply, or the sustainable international availability of In, Ga and As has always been a concern[7]. On the other hand, binary TMC materials (e.g. SnS) are non-toxic, low-cost, and composed of earth-abundant elements. The solar cells based on them also have a high theoretical conversion efficiency of 20%[9]. Nevertheless, the efficiencies of the cells based on simple binary TMCs are very limited in practice, due to the low quality of the thin TMC films and the unfavourable band offset between the TMC film and other components of a solar cell. Additionally, in a solar cell, TMC is usually applied as absorber layer due to its narrow and adjustable band gap, which is beneficial to light absorption. However, forming an effective interface between the TMC absorber layer and TiO_2 is still a difficult task.

This project aims to study the interfacial properties of TMC-based solar cells, and hopefully provide insight in order to improve their performance. In this project, we attempted to produce a prototype solar cell with acceptable light-to-electricity conversion efficiency, based on binary TMC light absorber including SnS and MoS_2, and mesoporous TiO_2 buffer layers, and to characterise the chemistry and electronic structure of the TMC-oxide interface.

2 Literature Review

2.1 Photovoltaic cells

A solar cell, or a photovoltaic cell, is a device which directly converts the energy of light into electrical energy through the photovoltaic effect[4,10]. A PV energy conversion procedure in a solar cell consists of two essential steps. The first step is the absorption of light by the semiconductor material and the generation of electron-hole pairs within the material, and the second step is the separation of electrons and holes and their migration to the corresponding terminals for the generation of a photocurrent[11].

2.2 p-n junction

2.2.1 Doping and extrinsic semiconductors

Doping is a process that impurities are implanted in semiconductor materials to create extrinsic semiconductors, in order to distinguish them from intrinsic semiconductors such as pure silicon[12]. By doping group V atoms with pure silicon, n-type semiconductors are formed. As shown in Figure 1, when a silicon atom is substituted by a phosphorous atom, four out of the five valence electrons in the substitutional phosphorous atom are used to form covalent bonds with the four silicon atoms adjacent to the phosphorous atom. Therefore, one valence electron of the substitution P atom is left free as a charge carrier. The impurity phosphorous atoms are called donors as they donate electrons. P-type semiconductors are manufactured by doping pure silicon with trivalent atoms, such as boron atoms. The formation of covalent bonds between the substitutional boron atom and the four adjacent silicon atoms demands four valence electrons from the boron atom. However, a boron atom possesses only three valence electrons, which results in a hole being left to be filled by an electron. Hence, in p-type

semiconductors, holes are the charge carriers[13]. The impurity B atoms are referred to as acceptors.

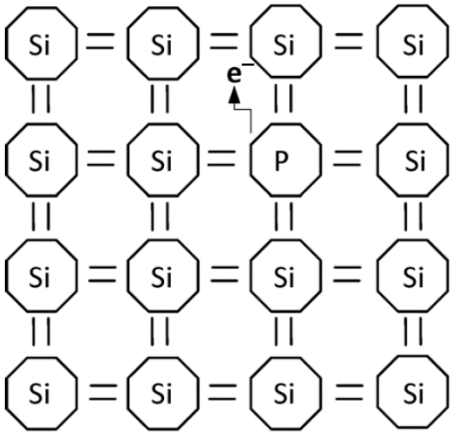

Figure 1 A sketch showing the substitution of a phosphorous atom in silicon[12].

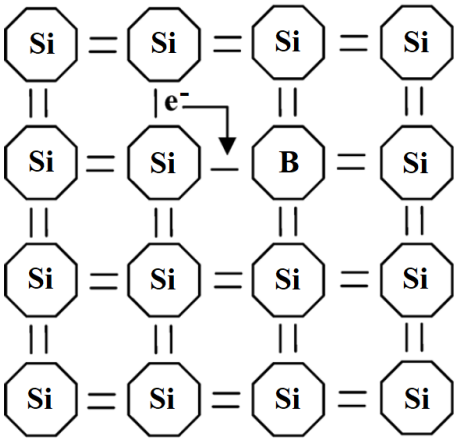

Figure 2 A sketch showing the substitution of a boron atom in silicon[12].

2.2.2 p-n junction

It is the special electronic property of a p-n junction which allows the implantation of the separation of photogenerated electron-hole pairs. A p-n junction is formed when p-type and n-type semiconductors are placed in contact with each other[13]. In the very thin contact area, the free electrons in the n-type region pass through the p-n material interface to the p-type region and recombine with the holes. Therefore, the impurity acceptor atoms within the contact area accept electrons to form negative ions. Similarly, the donor atoms near the interface lose the electrons, and as a result, they become

positive ions. As a result, a thin-layer region called “depletion region”, which is free of electrons and holes, is formed across the interface[14]. The separated distribution of positive ions and negative ions induces a built-in electrical voltage in the depletion region.

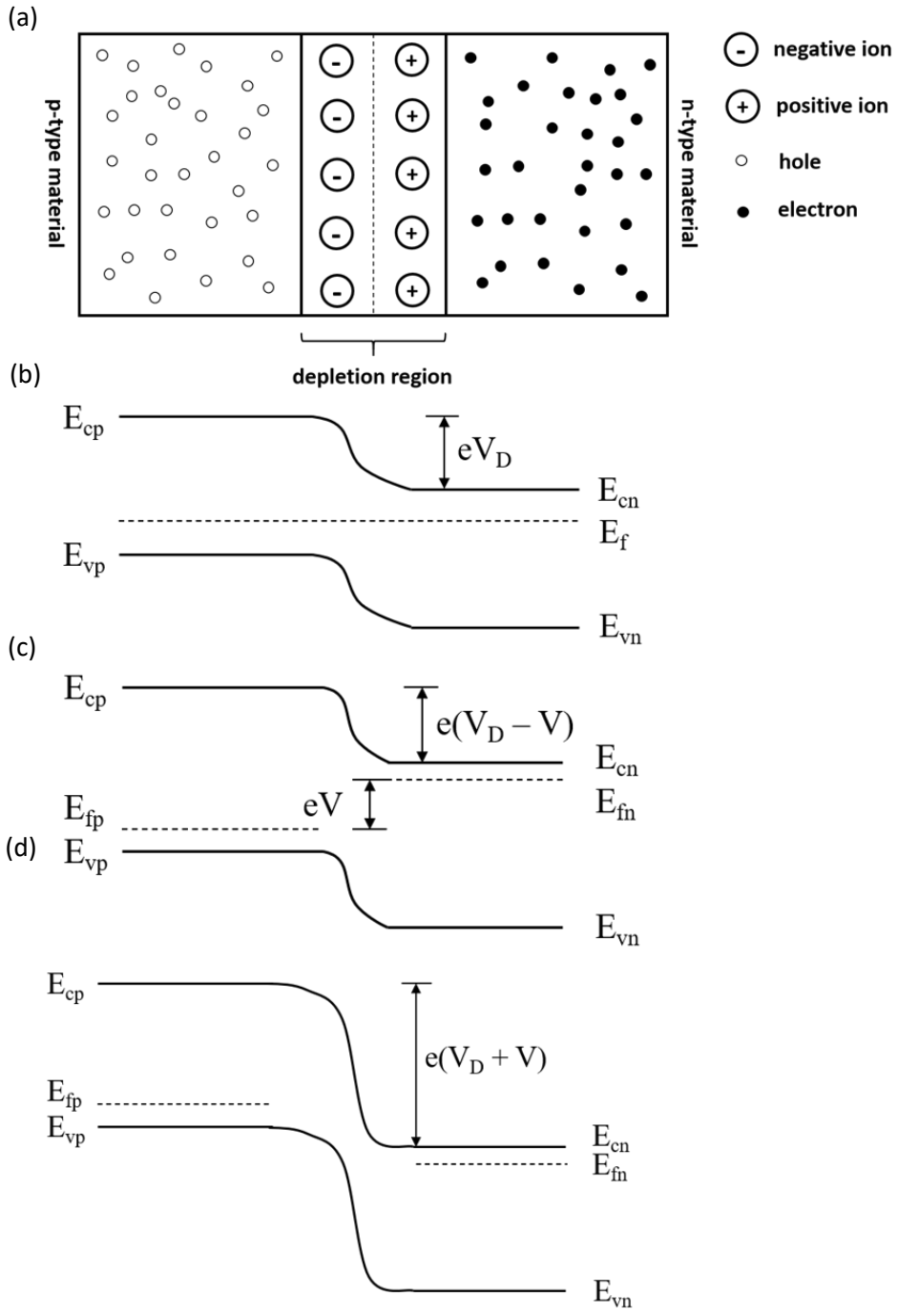

Figure 3 (a) A schematic presentation of a p-n junction and its depletion region. Band diagram of a p-n junction for (b) equilibrium, (c) forward bias and (d) reverse bias.

2.3 Construction and working principles of solar cells

The structure of a typical p-n junction solar cell is shown in Figure 4(a) and the band diagram of a typical silicon solar cell is shown in Figure 4(b). The function of energy conversion of a solar cell is based on the electrical and electronic characteristics of the p-n junction under illumination. As shown in Figure 4(b), when light which carries sufficient energy reaches the p-n junction, photons are absorbed by the semiconductor and electron-hole pairs are generated within the junction (Figure 4(b)). The incident light breaks the thermal equilibrium condition of the junction. The photogenerated electrons are gathered in the n-type side while the holes are collected in the p-type side. Once the photogenerated electrons migrate to the n-type side, they are prevented from moving further across the depletion region of the p-n junction due to the barrier potential of the junction. At the same time, the photogenerated holes in the p-type side cannot move across the junction, either. As a result of the separation of photogenerated electrons and holes, a photo-voltage is set up. By connecting the p-type section and n-type section through an external circuit, a photocurrent can be generated[15–18].

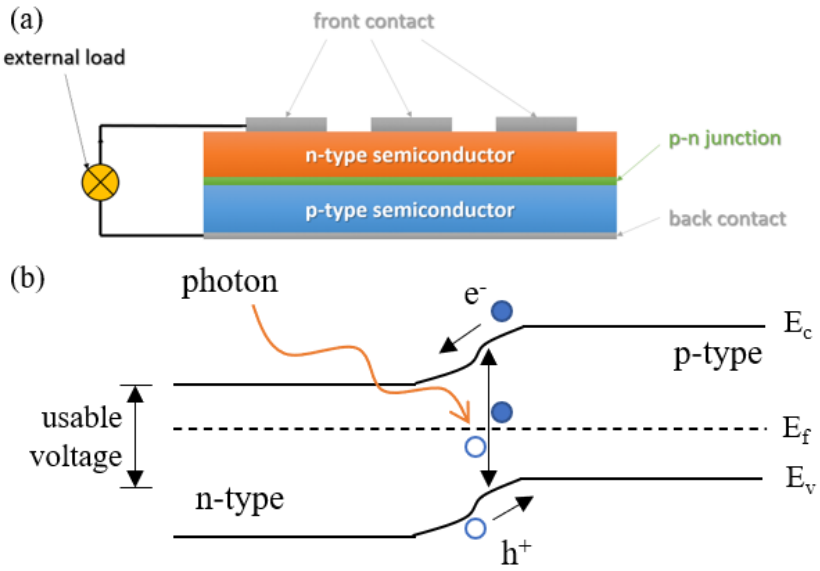

Figure 4 (a) The structure of a typical PV cell. (b) Band diagram of a typical silicon PV cell under illumination[18].

2.4 Shockley-Queisser limit

For a single p-n junction solar cell, there is a maximum theoretical efficiency known as the Shockley-Queisser limit[19]. According to the calculation of W. Shockley and H. J. Queisser, a maximum efficiency of 30% was given for a solar cell based on semiconductor material with a 1.1 eV band gap under standard test condition. The occurrence of Shockley-Queisser limit is a result of the inevitable energy losses in the process of conversion from solar energy to electricity. The Shockely-Quiesser model focuses on several considerations, including blackbody radiation, recombination, spectrum losses and impedance matching[19]:

All substances with a temperature > 0 K emit electromagnetic radiation through the black-body radiation effect[20]. 7% of all the energy falling on the solar cell is lost in the form of radiation, when the cell is assumed to be operated at room temperature[19].

Recombination of electron-hole pairs induce emitting of photons, which leads to energy losses. In Shockley-Queisser's model, the recombination rate is dependent on the voltage across the cell[19].

Spectrum losses cover a predominant portion of all the energy losses in the process of solar-electricity conversion. Only photons carrying energy higher than the bandgap of the semiconductor can be absorbed by the material and be used to generate electron-hole pairs. Therefore, semiconductors with small bandgaps allow better light absorption. However, not all the photons absorbed by the semiconductor materials can be transferred directly to electricity. Once a photon having energy larger than the bandgap is absorbed by the semiconductor, a proportion of the energy carried with the photon can be used to excite electrons across the band gap[21]. The remaining proportion of the energy ($hv - E_g$) is transferred into the kinetic energy of the excited electron, which is then lost as heat due to 'lattice scattering'[21]. Therefore, small-bandgap semiconductors

may have higher photon absorption, but a greater proportion of the photon energy will be lost in the form of heat and thus cannot be converted to electricity. Semiconductors having large bandgaps may absorb fewer photons, but a greater proportion of the energy of the absorbed photons can be converted to electricity. According to Shockley and Queisser's calculation, the optimum bandgap giving a maximum conversion efficiency of 33.7% is 1.34 eV for a single p-n junction PV cell[22].

The resistance of the external load will also influence the fill factor (FF). More energy can be lost due to inappropriate impedance matching. The maximum theoretical FF calculated based on the Shockley-Queisser model is 86.5%[19].

2.5 Dye sensitised solar cells

Unlike the conventional silicon-based solar cells introduced in the above section, in a dye sensitised solar cell (DSSC), the function of light absorption is not directly accomplished by the p-n junction, but the dye molecules instead[23]. The structure of a DSSC and the electron transport processes are shown in Figure 5(a) and (b), respectively. As shown in Figure 5(a), the dye molecules adsorbed on the TiO_2 film absorb photons and get excited, after which the electrons are injected into the conduction band of TiO_2[24]. The injected electrons migrate through the TiO_2 thin film and then TCO (transparent conducting oxides) glass to the external circuit and do useful work. Finally, the electrons are collected by the electrolyte at the counter electrode, and subsequently absorbed to regenerate the dye molecules[24].

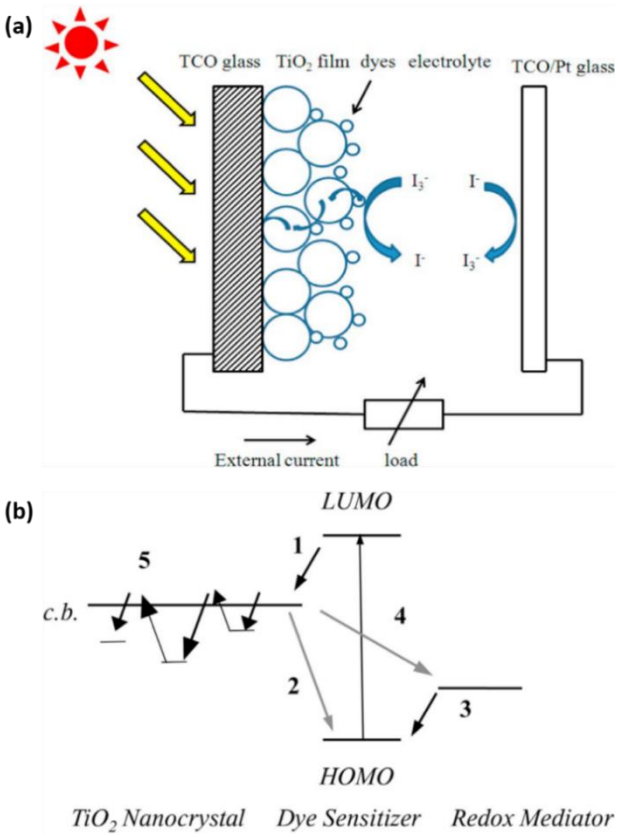

Figure 5 (a) A sketch of the structure of a DSSC. (b) Schematic illustration of electron transfer processes in a DSSC. Electrons are injected into the conduction band (c.b.) of TiO_2 (1), migrate through multiple traps to the TCO glass (5). A redox couple regenerates dye sensitiser (3). (2) and (4) represents two dominating pathways to lose electrons, which are loss with the dye cation or with the redox couple respectively[24].

DSSCs are not the only type of solar devices which separate the function of light absorption and charge carrier separation. Some small bandgap inorganic semiconductor materials can also act as a light absorber when coupled with other semiconductors with larger bandgaps[25].

2.6 SnS-based solar cell

2.6.1 Structure and polymorphism of SnS

Tin monosulfide exists in three different types of crystal structures: orthorhombic (herzenbergite), zinc blende (wurtzite) and NaCl (Sphalerite)[26]. Among the three crystal structures, SnS(OR) and SnS(ZB) exist at room temperature, while the NaCl structure SnS exists only at elevated temperature[27]. The crystal structures of SnS(OR) and SnS(ZB) are shown in Figure 6. Figure 6(a) shows that SnS(OR) has a layer structure,

where adjacent layers are bound to each other by Van der Waals force, and Sn−S chemical bonds only exist within each layer. The unique layered structure of SnS(OR) allows it to be prepared as a 2D material with unique properties[28]. SnS(ZB), on the other hand, has the wurtzite structure as shown in Figure 6(b), and as a result, it cannot be prepared as a 2D material.

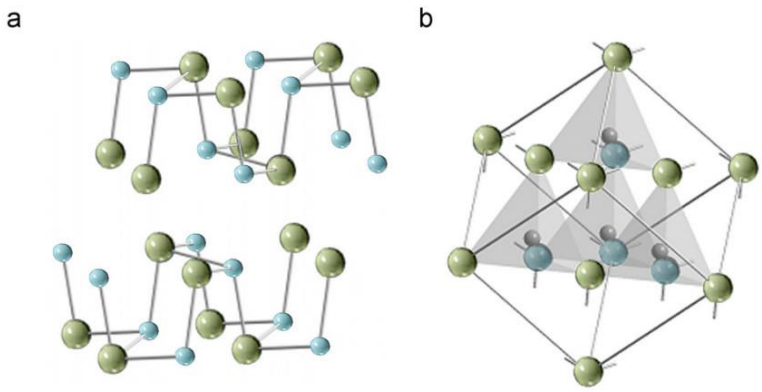

Figure 6 The crystal structure of (a) SnS(OR) (b) SnS(ZB)[29].

SnS(OR) is the most commonly investigated and reported[30–35] 2D structure, due to the simplicity of its synthesis process[29]. It is the predominant phase in SnS films prepared by methods involving vacuum evaporation[36], spray pyrolysis[37], chemical bath deposition[38,39], and electrochemical deposition[40]. ZB structure and NaCl structure SnS thin films can only be synthesised on specific substrates under suitable physical conditions[29].

2.6.2 Tin sulfide in photovoltaic applications

Tin sulfide has attracted much attention as a candidate material for photovoltaic applications. SnS has a direct optical energy band gap of ~ 1.3 eV[32] (the band gap varies with the synthesis route) which is close to the optimum value and an absorption coefficient $\alpha > 10^4$ cm^{-1}, which is much larger than that of silicon[41]. It shows p-type conductivity due to the easy formation of Sn vacancies and its electrical properties can be modified by doping[31,42,43]. SnS is non-toxic, which is another desirable property

compared to other absorber materials commonly used in solar cells, such as $CuIn(Ga)Se_2$ and CdTe. Additionally, tin and sulfur are elements which are abundant in nature and of very low cost[31,42,43].

SnS-based solar cells have a high theoretical conversion efficiency of 20%[9]. However, the efficiency of SnS-based solar cells produced recently usually vary within a range of 0.2% – 3%[43–47]. This is very low compared to solar cells based on other light absorbers, such as perovskites and doped silicon. Many researchers have investigated the factors which lead to this unexpected low efficiency. The poor quality of SnS thin films is considered to be one of the key reasons for the low efficiency of SnS-based solar cell[9]. The poor quality is usually a result of secondary phases (e.g. SnS_2 and Sn_2S_3) produced in the process of synthesis[9]. Secondary phases enlarge the band gap energy and lower the absorption coefficient of the absorber film. Additionally, compositional changes due to the existence of secondary phases may lead to a conductivity type inversion, either p-type or n-type[48]. The poor quality of SnS thin film is sometimes due to the instability of Sn^{2+}. Sn^{2+} can be oxidised to Sn^{4+} and form SnO_2 when the film is exposed to air. Another reason for the low efficiency of SnS-based solar cells is that, during the synthesis process of polycrystalline SnS, the formation of grain boundaries is inevitable. These grain boundaries will act as recombination centres which boost the electron-hole recombination rate and result in low efficiency[41]. However, in 2013, Lee and Aron proposed that, the key factor which limits the efficiency of SnS-based thin film solar cells, may be the band alignment between SnS absorber layer and other layers of the cell, rather than the poor quality of SnS films[49]. Previous reports[50] had shown that even a high-quality single-phase SnS film could have very limited conversion efficiency. The authors predicted the band alignment between SnS and other materials commonly used in solar cells based on electronic structure calculations, using a hybrid non-local

density function. The calculated ionisation potential of SnS (4.7 eV) was much lower than that of other absorber materials, which results in a mis-alignment with the back contact and the buffer layer[49]. In order to overcome the efficiency limit of SnS-based solar cells, many researchers have attempted to improve the quality of SnS thin film and optimise the solar cell structure, as discussed below.

Chemical bath deposition (CBD) is the synthetic method most commonly selected due to the simplicity. M. T. S. Nair and P. K. Nair successfully obtained good-quality SnS thin films with thicknesses of up to 1 μm[51]. Two different chemical baths were prepared for the deposition of SnS films. Bath X was composed of:

- 1 g of $SnCl_2 \cdot 2H_2O$ dissolved in 5 ml of acetone
- 8 ml of 1 mol/l thioacetamide in deionised water
- 10 ml of 4 mol/l NH_3 (aq)
- 12 ml of 50% triethanolamine

Bath Y has the same composition, except that the amount of thioacetamide is half the amount in Bath X. SnS films were deposited in both Bath X and Bath Y at 60°C for 5 hours. The film obtained from Bath X had a thickness of 0.55 μm while the one obtained from Bath Y had a thickness of 0.30 μm. The report showed, a small change in the composition of the chemical bath will lead to a variation in the thickness of SnS thin films[51].

In 2007, D. Avellaneda *et al.* reported that, another possible reason for the low conversion efficiency of SnS-based solar cells is difficulty in fabricating SnS films with sufficient thickness[52], so that only a small portion of light can be absorbed by the thin film. The authors attempted to integrate thicker SnS films by increasing the deposition time and immersion number, however, the maximum thickness that could be achieved

was 500 nm. In 2009, different properties of zinc blende (ZB) SnS and orthorhombic (OR) SnS for solar application were investigated[44]. Two different chemical baths were prepared for the deposition of zinc blende SnS(ZB) and SnS(OR) layers. The photovoltaic cell structure shown in Figure 7 was built. The existence of the two phases was confirmed by XRD[44]. The influence of the thickness of SnS(ZB) and SnS(OR) layers on the performance of the whole photovoltaic structure was evaluated by a current-voltage (*J*-*V*) measurement. The thickness of SnS(ZB) layer was fixed at 0.05, 0.1 and 0.2 µm, while the thickness of SnS(OR) was varied gradually from 0.05 to 0.5 µm. The theoretically evaluated short circuit current density J_{SC} at each fixed thickness of SnS(ZB) is shown in Figure 8 as a function of the thickness of SnS(OR). The curves shown in Figure 8 indicate that the influence of SnS(ZB) on the current density is negligible when the thickness of SnS(OR) layer exceeds 0.25 µm. The authors presume that the negligible effect of SnS(ZB) layer is a result of the 1.2 eV band gap of SnS(OR) which is much smaller than the 1.71 eV band gap of SnS(ZB)[53]. Therefore, most charge carriers were generated in the SnS(OR) layer rather than the SnS(ZB) layer. Figure 9 shows the *J*-*V* characteristics of the photovoltaic devices when the thickness of SnS(OR) layer is 0.25, 0.35, and 0.5 µm, while the thickness of SnS(ZB) is fixed at 0.1 µm. Calculation of solar cell parameters indicate that this photovoltaic structure exhibits the best performance when SnS(OR) is controlled at a thickness of 0.5 µm[44].

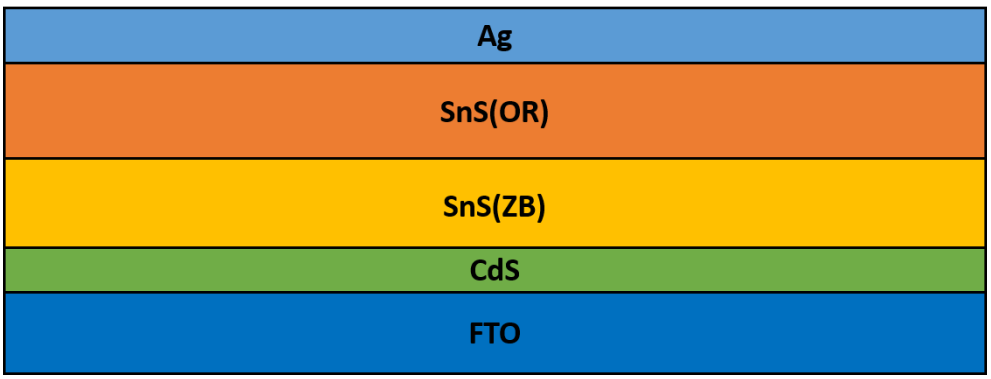

Figure 7 Schematic presentation of the stacking of the photovoltaic device[44]

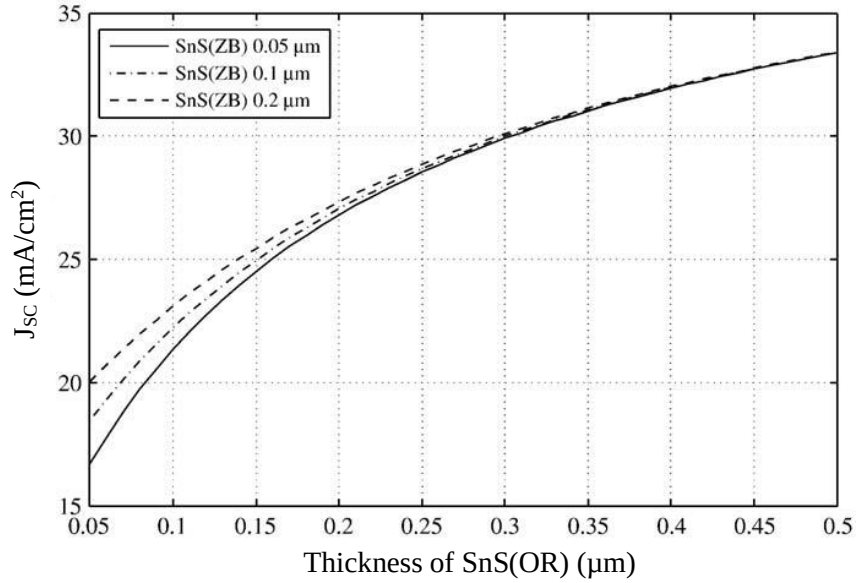

Figure 8 Theoretically predicted short circuit current density, J_{SC}, as a function of the thickness of SnS(OR) layer when the thickness of SnS(ZB) layer is fixed at 0.05, 0.1, and 0.2 μm, respectively[44].

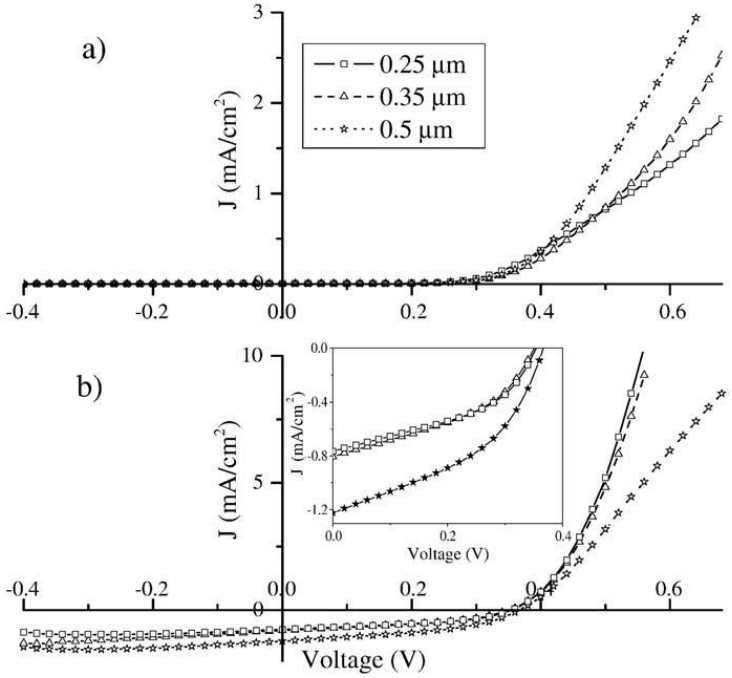

Figure 9 *J-V* curves of photovoltaic structures built at SnS(ZB) thickness of 0.1 μm and SnS(OR) thickness of 0.25, 0.35 and 0.5 μm[44].

Y. Wang *et al.* investigated the photovoltaic behaviour of SnS/TiO_2 heterostructure[54]. To build a photovoltaic structure, a porous TiO_2 thin film was deposited on an FTO substrate, followed by chemical bath deposition of an SnS thin layer onto the porous TiO_2 layer. Then, a Pt back contact was deposited on the surface of the other FTO substrate slide and placed facing the SnS layer. By doing this, a heterostructure (FTO/Pt

+ SnS/TiO_2/FTO) was built. However, under 1 sun (100 mW/cm^2) light illumination, the as-fabricated device showed negligible photovoltaic response and the conversion efficiency was < 0.02%[54]. The authors reckoned that the poor conversion efficiency could be a result of the poor conductivity between SnS and TiO_2. Therefore, to improve the conductivity of the device, electrolyte was added to build a heterostructure of FTO/Pt + electrolyte + SnS/TiO_2/FTO. An improved photovoltaic behaviour (Figure 10) was observed after adding the electrolyte.

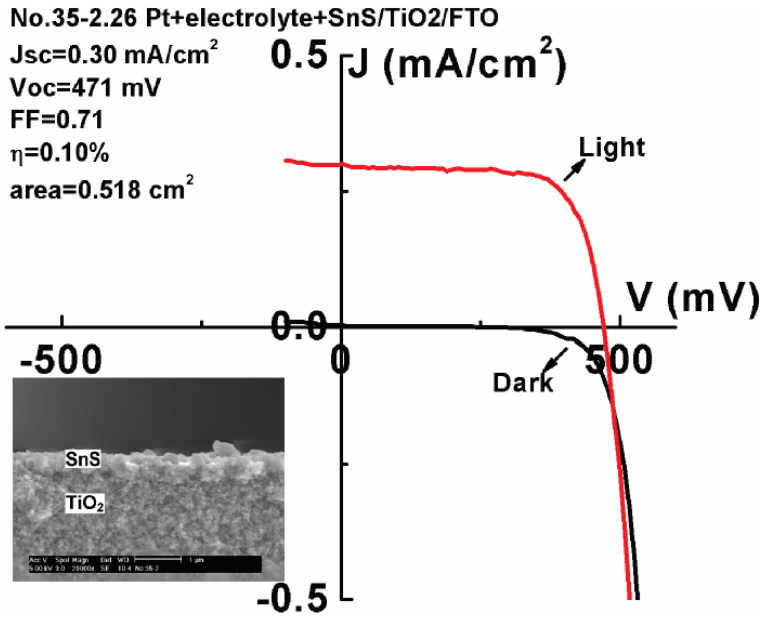

Figure 10 *J-V* curves of the SnS/TiO_2 solar cell in the dark and under illumination. The embedded SEM image shows the cross section of SnS/TiO_2 heterojunction[54].

Under 1 sun illumination, the device with this heterostructure exhibited a high open-circuit voltage of 471 mV, a short-circuit current density of 0.30 mA/cm^2, an improved efficiency of 0.10% and a FF of 0.71[54]. A photovoltaic structure without the existence of SnS layer was also fabricated to confirm whether the existence of SnS is beneficial to the improvement of the solar cell parameters. Under the same illumination, the photovoltaic structure without the SnS layer showed only a conversion efficiency of 0.03%, which indicates that the presence of SnS layer improves the performance of the as-built photovoltaic structure.

Table 1 Dimensions of TiO_2 materials used in the photovoltaic cells and the conversion efficiency of the cells based on each type of TiO_2, respectively[45].

TiO_2 type	Particle size (nm)	Surface area ($m^2 \cdot g$)	Conversion efficiency
Nanocrystalline TiO_2	10	87.8	0.03%
P25 nanoparticles	20 – 50	55	0.05%
Well-ordered mesoporous TiO_2 films with regularly packed TiO_2 nanocrystals	N/A	107.7 – 127.2	0.13%
Spherical TiO_2 electrode	N/A	60	2.8%

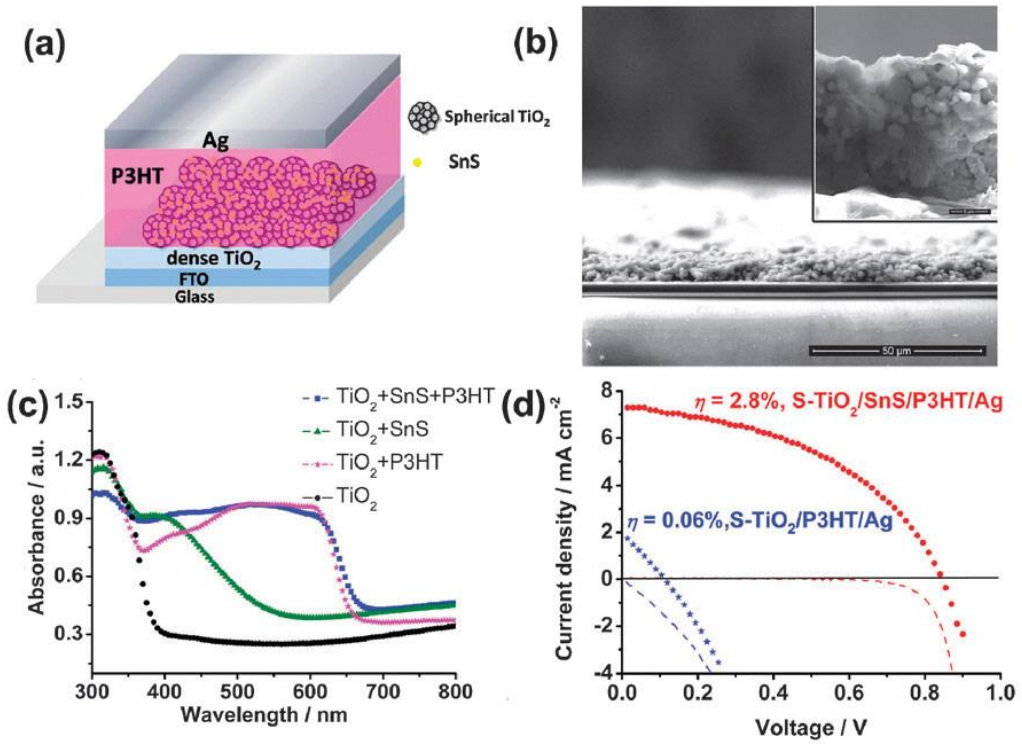

Figure 11 (a) Schematic presentation of SnS-HSCs; (b) SEM image of the cross section of SnS-HSCs, the inset scale bar 5 μm; (c) UV-Vis absorption spectra for each structure; (d) *J-V* characteristics of HSCs with and without SnS layer[45].

In 2012, W. Guo *et al.* reported a highly efficient inorganic-organic heterojunction solar cell (HSC) based on SnS-sensitised TiO_2 electrodes[45]. An HSC device based on a structure which was composed of TiO_2–SnS–P3HT–Ag was successfully fabricated. The structure of the cell is shown in Figure 11(a). Figure 11(b) shows the SEM image of the cross section of the HSC. It is shown in Figure 11(b) that the as-synthesised TiO_2 particles are well preserved and the polymer P3HT evenly and completely fill the pores

among the spherical TiO_2 film. Figure 11(c) is the UV-Vis absorption spectra of four different photovoltaic structures. It shows that the absorption of the TiO_2–SnS–P3HT structure ranges from 400 to 650 nm, while that of the TiO_2–P3HT structure ranges from 500 to 650 nm. It implies that the SnS layer enhances the light absorption in the range of 400 – 500 nm. The measurement of photovoltaic characteristics was done under ambient atmosphere. The *J-V* curves obtained are shown in Figure 11(d). A calculation based on the *J-V* characteristics shows that the photovoltaic structure without the SnS absorber layer exhibits a conversion efficiency of only 0.06%, while the presence of SnS layer raises the power conversion efficiency to 2.8%. Other factors which influence the performance of the TiO_2–SnS–P3HT structure were also investigated. It is found that, as the SnS deposition time increases from 1 h to 3 h, the conversion efficiency of HSCs is improved from 2.33% to 2.81%. However, the efficiency drops to 2.15% when the deposition time was set to 4 h. Then, the authors used other types of TiO_2 material for the fabrication of TiO_2 layers. The dimensions of the TiO_2 materials used for the fabrication of TiO_2 layers and the conversion efficiency obtained accordingly are summarised in Table 1. Table 1 shows that the efficiency obtained varies dramatically with the dimensions of TiO_2 particles used for the fabrication of the buffer layers, which indicates that the nanostructures of TiO_2 electrodes have a huge impact on the performance of the HSCs produced in this research. The authors presume that the reason for the lower efficiency observed when the deposition time for SnS film exceeds 3 h, is that the pores of TiO_2 films are blocked by SnS. Therefore, P3HT is unable to fill in these blocked pores, leading to a reduced efficiency.

Spray pyrolysis is another technique commonly used for the synthesis of SnS thin films. The research in spray pyrolysis of SnS for solar application has been led by N. K. Reddy

and K. T. R. Reddy, who attempted to deposit SnS by spray pyrolysis[42] and also investigated the physical properties of sprayed Sn_xS_y films. Sn_xS_y films were deposited on Sb-doped tin oxide-coated glass substrates at various substrate temperatures within the range of 100 – 450 °C[31]. EDX was carried out for compositional analysis of the Sn_xS_y films synthesised. It was found from the EDX results that, when the substrate temperature is under 300 °C, the Sn_xS_y films were sulfur-rich in composition. When the substrate temperature is over 375 °C, the Sn/S ratio will rise to a value of > 1.23 due to the re-evaporation of sulfur. However, when the temperature lies in the range, 300 – 375 °C, the films deposited are nearly stoichiometric, with an elemental Sn/S ratio of 1.03. The phases of the as-fabricated SnS thin film were confirmed by XRD analysis. According to the authors, XRD profiles of layers grown at different temperatures indicated that the layers grown at temperatures < 200 °C were amorphous in nature, while those formed in a temperature range of 200 – 300 °C show peaks that correspond to Sn_2S_3 and SnS_2 phases. However, only one XRD profile of an SnS thin film synthesised at a substrate temperature of 350 °C is shown in the report. The profile indicates that single-phase SnS was obtained at a substrate temperature of 350 °C. For growth temperatures > 375 °C, the films exhibited reflections corresponding to SnO_2 and Sn−O−S. Overall, this study demonstrated that high-quality single phase SnS thin films could be produced by spray pyrolysis at a substrate temperature of around 350 °C, while temperatures that were too high or too low lead to amorphous or other secondary phases.

These sprayed SnS thin films were then investigated for solar cell applications[43]. In order to build the photovoltaic structure, a solution composed of 0.1 M $SnCl_2$ and 0.1 M n,n-diethyl thiourea were sprayed onto the surface of SnO_2 coated glass substrates which were preheated to 350 °C. After the SnS film was deposited, a CdS film with a

thickness of ~0.6 µm was grown onto the SnS thin film and doped with 2 at. % indium. Finally, a thin layer of indium as the top contact was loaded on the CdS thin film. The as-fabricated solar device exhibited a conversion efficiency of 1.3% with a quantum efficiency of 70%. The limited thickness of SnS (0.6 µm) is identified as the reason for the low power conversion efficiency.

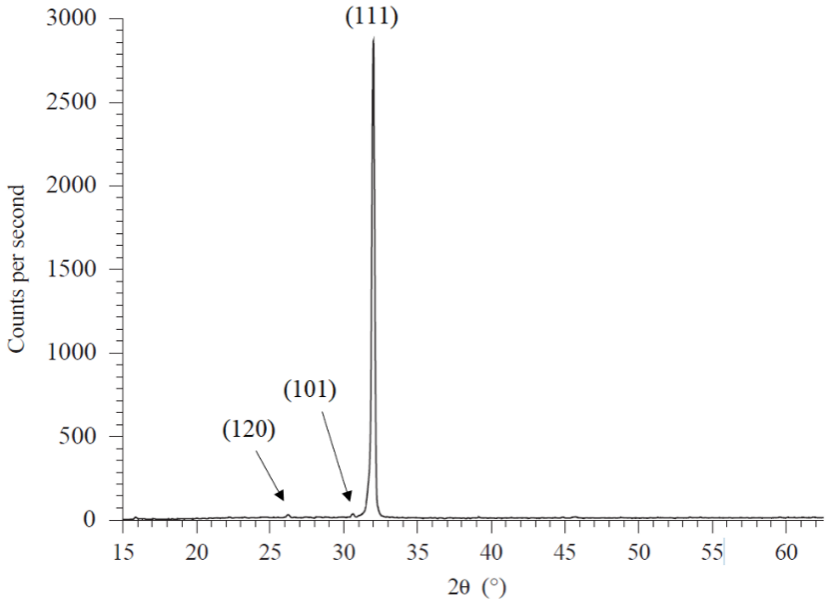

Figure 12 XRD pattern of a SnS film prepared by electron beam evaporation. The peaks from higher degree to lower degree correspond to (111), (101) and (120) reflections and the intensity difference between the peaks indicate preferential orientation[38].

Electron beam evaporation is sometimes used for synthesis of high-quality SnS thin film. A. Tanuševski and D. Poelman investigated the optical and photoconductive properties of SnS prepared by electron beam evaporation[38]. The XRD profile of the SnS thin film produced is shown in Figure 12. The most intense peak at 2θ = 31.6° corresponds to the (111) reflection, while the other two minor peaks at angles 2θ = 26.4° and 2θ = 30.8° corresponds to (120) and (101) reflections, respectively. Their work revealed that SnS crystals synthesised using electron beam evaporation exhibits preferential orientation[38]. J. Y. Kang *et al.* introduced an SnS seed layer to control the preferential orientation of SnS absorber layers[55]. The report illustrated the importance

of the preferred orientation of SnS crystals and offered a route to control it. The importance of preferred orientation of SnS crystals origins from the unique lattice structure of SnS and the vulnerability of the interlayer. As shown in Figure 13(c) and Figure 6(a), the unit cell of orthorhombic SnS has a long b-axis and consists of two weakly bonded layers in which atoms are strongly bonded. The interlayer is perpendicular to the b-axis. The interlayer is vulnerable since Sn impurity atoms can easily occupy the interstitial sites within the interlayer. Therefore, as shown in Figure 13(b), when the SnS thin film has a preferred orientation of (101), the Sn impurities distributed along the interlayer will probably form a shunt path. However, if the SnS crystals are stacked along a preferred orientation of (040), as shown in Figure 13(a), the interlayer shunt path will be disconnected from the substrate and a high conversion efficiency can be obtained.

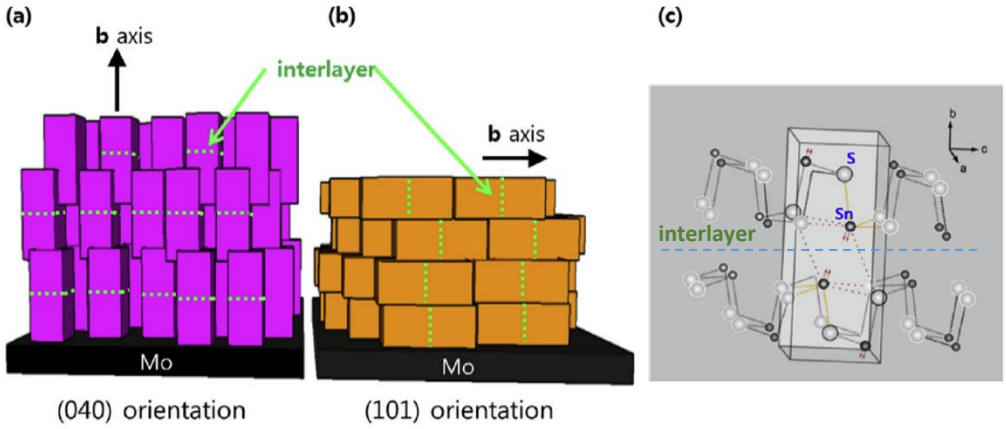

Figure 13 Schematic presentation of the SnS thin films with (a) b-axis perpendicular[55], (b) b-axis parallel to the Mo substrate surface[55], and (c) the lattice structure of SnS unit cell[35].

In this work, the authors prepared two different types of metal Sn precursor: a Sn film deposited on SnS seed layer with a thickness from 100 – 300 nm and a pure metal Sn film. The SnS seed layer was deposited on the surface of a Mo sputtered soda-lime glass substrate using electron beam evaporation, followed by the deposition of Sn metal using DC magnetron sputtering. A rapid thermal annealing (RTA) process was done then, for

the sulfurization of the Sn precursors. The whole annealing process includes two steps: the low temperature (240 °C) S-soaking step and the high temperature (400 °C) sulfurization step[55].

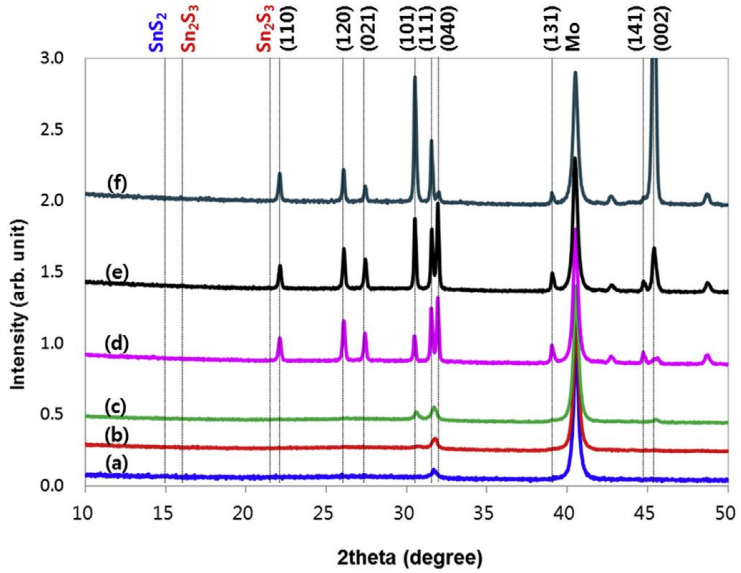

Figure 14 XRD patterns; (a), (b) and (c) correspond to the as-deposited SnS seed layers with a thickness of 100, 200, and 300 nm, respectively. (d), (e) and (f) correspond to the SnS absorbers grown on 100, 200 and 300 nm thick seed layer, respectively[55].

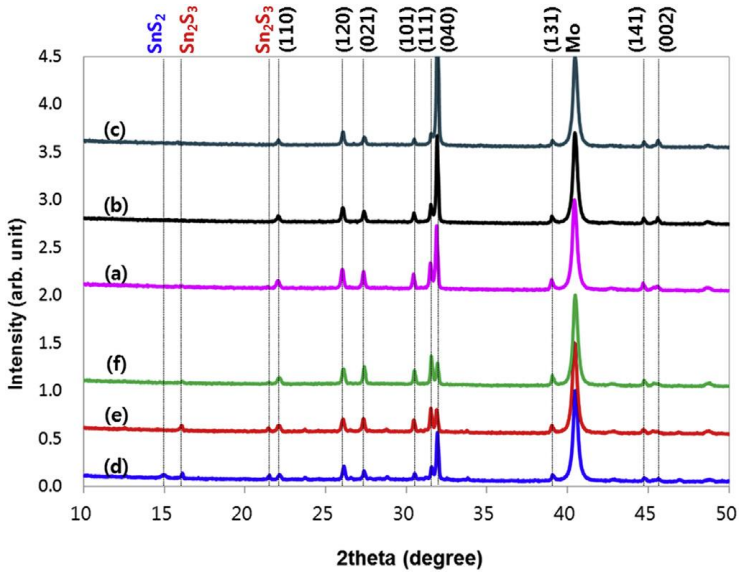

Figure 15 XRD patterns; (a), (b), and (c) correspond to the seeded SnS absorbers and (d), (e), and (f) to the non-seeded SnS absorber with varying sulfurisation time for 10, 20, and 30 minutes, respectively[55].

In the S-soaking step, sulfur atoms were delivered to the precursor through a S vapour supplied by the RTA system, and then crystalline phases of SnS and other secondary phases (e.g. SnS_2 and Sn_2S_3) were formed. In the sulfurisation step, the crystalline tin

sulfides were heated at an elevated temperature for 10 – 30 minutes to coarsen the fine SnS crystals and reduce the number of secondary phases. Figure 14 shows the XRD profiles of the as deposited 100, 200, and 300 nm SnS seed layers and the SnS absorbers grown on each seed layer, respectively. These XRD profiles indicate that high-quality single phase SnS crystals were obtained for both seed layers and SnS absorbers grown on the seed. It is also clear that the (040) orientation was preferentially obtained when a thin seed layer is deposited beforehand, but with the seed layer thickness increasing, the absorbers prefer a (101) orientation. Simultaneously, with the seed layer getting thicker, the (101)/(040) or (002)/(040) peak ratio of both the seed crystal and the absorber crystal become larger, which indicates the existence of an epitaxial relation between the crystal planes of the absorber and the seed layer. In other words, in the formation process of the SnS absorber layer, the seed layer is a nucleation centre and the orientation of the absorber layer is controlled by it. The effect of the sulfurisation time was also discussed. Figure 15 shows the XRD profiles of both the seeded and non-seeded SnS absorbers when the sulfurisation time is 10, 20, and 30 minutes. It can be seen from the XRD profiles that the (040) peak intensity of the seeded SnS absorber increases dramatically as the sulfurisation time varies from 10 to 30 minutes, while the same tendency is not seen in the SnS absorber that grew without a seed layer. It again shows that the crystal growth of the absorber layer is determined by the seed layer. The SEM and TEM images further show the relation between the seed layer and the absorber layer. As shown in Figure 16(d), the seed layer in the precursor is mostly incorporated into the absorber layer after sulfurisation (Figure 16(e)). This implies that the seed layer functions as a nucleation layer which controls the crystal growth preference of the SnS absorber layer. The grain size difference is shown in the TEM images (Figure 17). The seeded absorber has a smaller grain size and apparent grain

boundaries, while the non-seeded absorber appears in form of coarse grains as large as the film thickness[55].

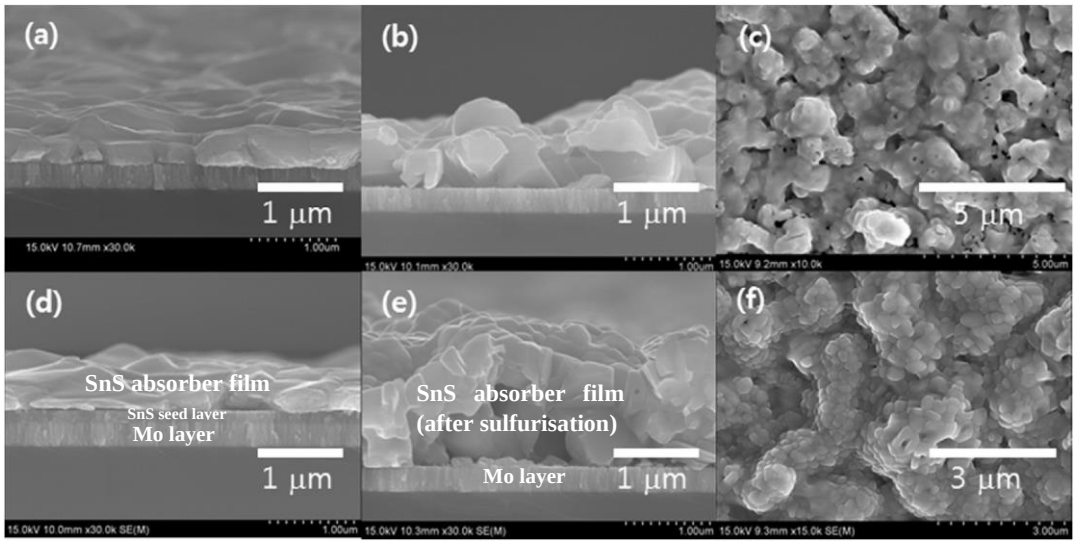

Figure 16 SEM images of (a) Sn/Mo (tilted cross-section view), (b) cross-section view and (c) planar view of Sn/Mo after sulfurisation, (d) Sn/100 nm seed/Mo (cross-section view), (e) cross-section view and (f) planar view of Sn/100 nm seed/Mo after sulfurisation[55]. Each layer in (d) and (e) is labelled in order to clarify their composition and function.

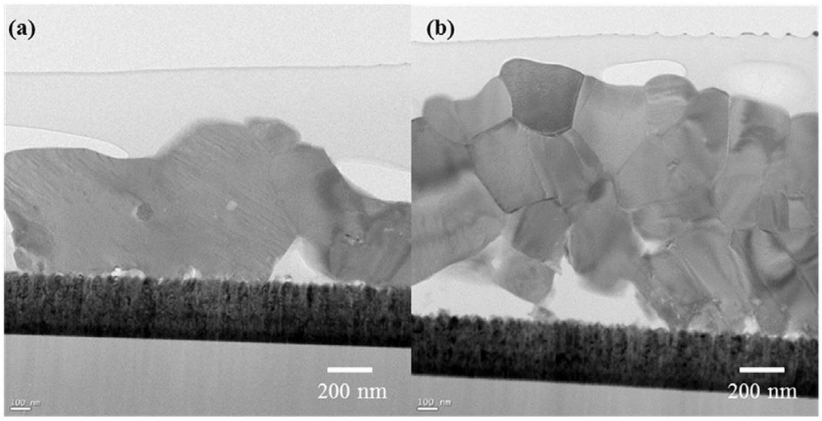

Figure 17 TEM images which show the grain structure of the (a) non-seeded absorber layer and (b) seeded absorber layer[55].

The solar parameters extracted from the *J-V* curve of the solar cells fabricated with the two types of absorber layers were compared in the graph shown in Figure 18(a). The solar cells with seeded absorber layer have better results in all performance parameters listed, compared to the cells without the seed. The improved performance of the solar cells with seeded absorber layer confirms that ordering of the film leads to improved efficiency. This work also suggested that, grain boundaries are not always detrimental

to the performance of SnS-based solar cells, and that for polycrystalline SnS absorber layers in solar applications, it is important to achieve a (040) preferred orientation to disconnect the shunt path to the substrate along the interlayer.

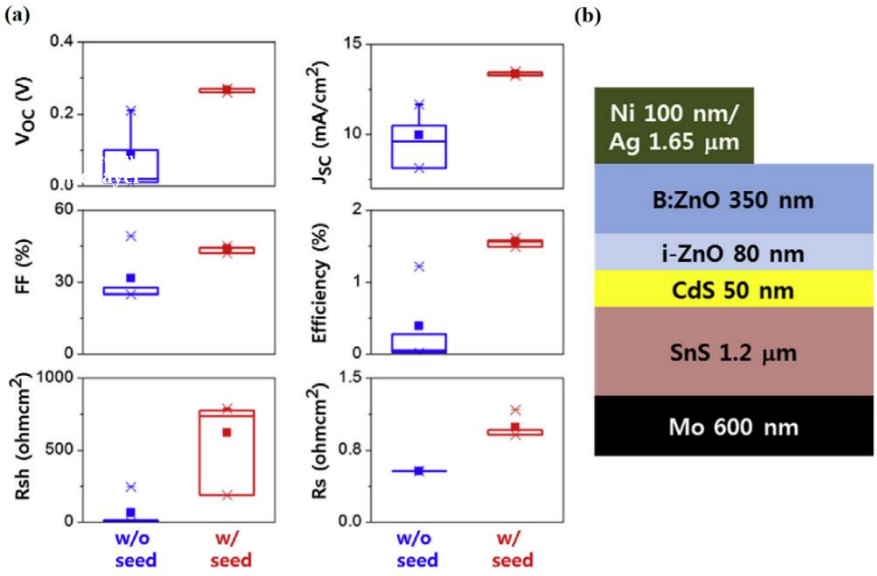

Figure 18 (a) Solar cell parameters of the two cells based on different absorber layers. The filled square corresponds to a mean value of 25 – 75 percentile box plots. Rsh and Rs refers to shunt resistance and series resistance, respectively. (b) Stacking structure of the solar cell investigated[55].

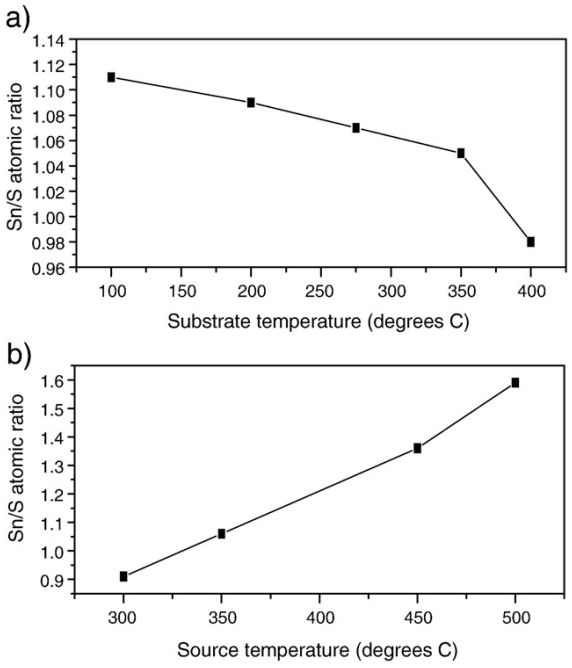

Figure 19 (a) A plot of Sn/S atomic ratio as a function of the substrate temperature (the source temperature was kept constant at 300 °C and deposition time constant at 2 min). (b) A plot of Sn/S atomic ratio as a function of source temperature (the substrate temperature was kept constant at 300 °C and deposition time constant at 2 min)[36].

Thermal evaporation is often used for the deposition of thick SnS films. R. W. Miles *et al.* investigated the properties of SnS thin films deposited on either soda-lime glass or FTO using thermal evaporation method, with a source temperature in the range of 300 – 600 °C and substrate temperature from 100 to 400 °C[36]. Figure 19 shows the variation of Sn/S ratio with the source temperature and substrate temperature. It is observed that the films become more S-rich with decreasing substrate temperature, and with increasing source temperature. Y. Kawano *et al.* further discussed the impact of growth temperature on the properties of SnS films prepared by a thermal evaporation method[47]. A SnS thin film based solar cell was fabricated with a stacking structure of Al/ZnO:Al_2O_3/ZnO/CdS/SnS/Mo/soda-lime glass[47]. Mo was coated as the back electrode by radio frequency (RF) sputtering, after which a SnS thin film was thermally evaporated onto the Mo coated soda-lime glass substrate. The growth temperature varied from 100 to 250 °C while the deposition time was fixed at 120 minutes. After the deposition of SnS absorber, other parts of the structure were deposited using various deposition methods[36]. The planar and cross-sectional view of the SnS thin films in Figure 20 shows that, as the growth temperature varies from 100 to 225 °C, the thickness of SnS films obtained decreases from approximately 8 µm to less than 2 µm, while the S/Sn ratio stays almost constant at around 1.04. Moreover, the crystal grains varied from thin flake-like shape to larger non-flake-like grains. There is difficulty in identifying between SnS and Sn_2S_3 by XRD due to peak overlap. Therefore, in order to identify compounds such as Sn_2S_3 in the absorber film, Raman scattering measurements were conducted. Figure 21 depicts the Raman spectra of the SnS absorber fabricated at different growth temperatures. When the temperature was increased from 100 to 150 °C, a Sn_2S_3 peak was found in the spectra. However, when the SnS absorber film was heated up to temperatures over 175 °C, the Sn_2S_3 peak disappeared, which implies a high

quality SnS absorber film is obtained at temperatures > 175 °C in case of thermal evaporation. The electronic properties of the SnS absorber layers grown at various temperature were also evaluated. It was found that a growth temperature of 200 °C, contributes to dense and large crystal grain sizes and the highest Hall mobility, which leads to a power conversion efficiency of 2.53%.

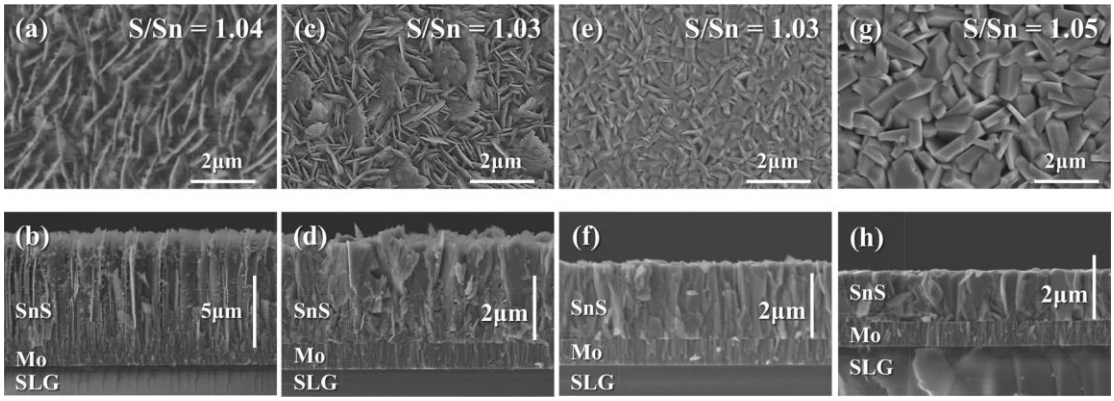

Figure 20 SEM images of planar and cross-sectional view of SnS films prepared by thermal evaporation at growth temperature of (a,b) 100, (c,d) 150, (e,f) 200, and (g,h) 225 °C[47].

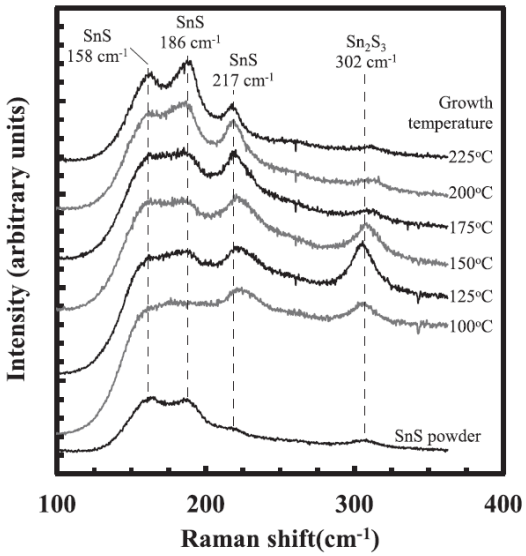

Figure 21 Raman spectra of SnS films prepared at growth temperatures from 100 to 225 °C[47].

In 2014, P. Sinsermsuksakul *et al.* made a breakthrough in overcoming the efficiency limitations of SnS based solar cells and successfully improved the conversion efficiency to a new record of 4.36%[41]. A solar cell based on a p-SnS/n-Zn(O,S) heterojunction was fabricated; the structure of the device is shown in Figure 22(a). The authors summarised four details which were carefully controlled in order to reach this

high efficiency. First, SnS films were annealed to reduce grain boundaries. Secondly, the conduction band offset between the SnS absorber layer and Zn(O,S) buffer layer was adjusted by tuning the composition of Zn(O,S). In order to reach the optimised efficiency, heterojunction solar cells usually need to have a "spike" type conduction band offset (CBO). A spike-type CBO means that the conduction band minimum of the n-type buffer layer is slightly higher than the conduction band minimum of the p-type absorber layer, and in this case, the recombination rate at the p-n junction can be reduced. As long as the positive CBO is controlled below 0.4 eV, the photoelectrons generated in the p-type absorber layer can still surmount the small energy barrier at the junction and be collected in the n-type layer[41]. However, devices produced under these conditions show negligible efficiency (Figure 23), as a result of the high conductivity of the Zn(O,S) buffer layer. Therefore, thirdly, to recover the performance of the SnS-Zn(O,S) diode, the Zn(O,S) layer was doped with nitrogen to trap the free electrons to reduce the conductivity[56]. Finally, a SnO_2 was inserted between the absorber layer and buffer layer, since the authors previously discovered that an oxidised SnS surface could significantly increase the open circuit voltage of the solar cell. This SnO_2 layer can be fabricated by either exposing SnS film to an oxidising agent or atomic layer deposition (ALD). This report revealed that, one of the keys to increasing the power conversion efficiency of SnS-based solar cells is to suppress the recombination of photogenerated electrons and holes.

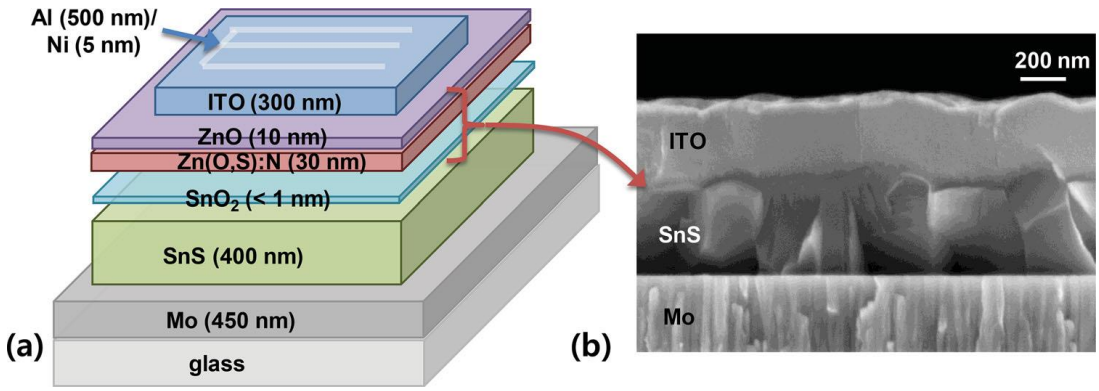

Figure 22 (a) Stacking structure of the SnS-based solar device. (b) A cross-sectional view of an actual cell with SnS annealed in H_2S[41].

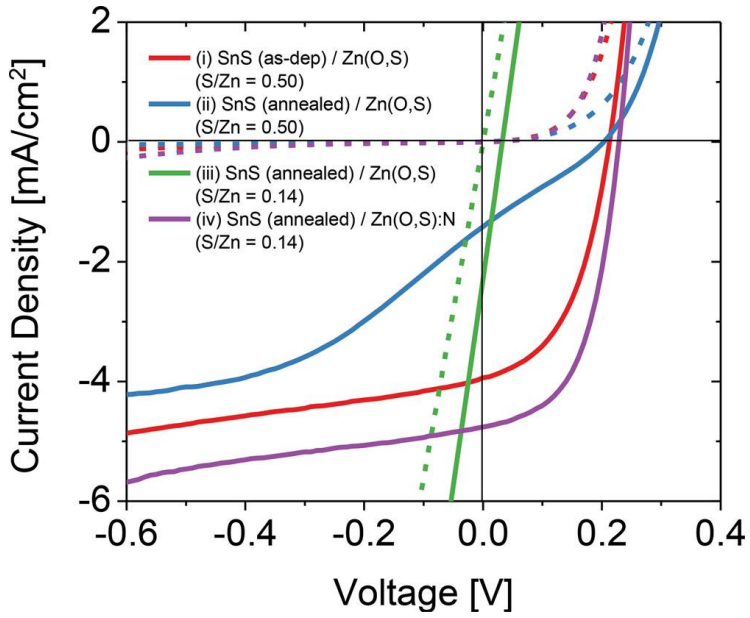

Figure 23 *J-V* characteristics under dark (dashed line) and low illumination (solid line) of solar devices composed of i) as-deposited SnS with Zn(O,S) (S/Zn = 0.50), ii) H_2S annealed (400 °C) SnS with Zn(O,S) (S/Zn = 0.50), iii) H_2S annealed (400 °C) SnS with Zn(O,S) (S/Zn = 0.14), and iv) H_2S annealed (400 °C) SnS with nitrogen-doped Zn(O,S):N (S/Zn = 0.14)[41]

S. Di Mare *et al.* reviewed recent achievements in the area of SnS-based solar cell research and summarised the perspectives and limitations of SnS-based solar cell[9]. In the review, they listed the best PCEs of SnS-based solar cells reported in literature. The results are reproduced in Table 2 below. It was also claimed in the review that a factor which limits the potential of SnS-based solar cell are issues due to irreproducibility caused by oxidation, which means that the efficiency of SnS-based solar cells drops rapidly after several runs.

Table 2 List of PCE results on SnS-based solar cells[9].

SnS deposition	Buffer layer	PCE
Chemical bath deposition[54]	TiO_2 porous thin film	2.81%
Spray pyrolysis[43]	CdS:In	1.3%
Thermal evaporation[32]	CdS	1.6%
Thermal evaporation[47]	CdS	2.5%
RF-sputtering[57]	$Zn_{1-x}Mg_xO$	2.1%
Pulsed-CVD[58]	Zn(O,S)	2.9%
VE(vacuum evaporation) [59]	Zn(O,S)	3.88%
ALD[41]	Zn(O,S)	4.36%

2.6.3 Summary

In conclusion, SnS possesses properties desired for solar cells, including a direct band gap of 1.3 eV, an absorption coefficient of 10^4 cm^{-1} in the visible light range[50] and non-toxicity. However, the application of SnS-based solar cell in practice is still facing challenges.

The first challenge is to overcome the efficiency limitation. According to reports recently published, the highest conversion efficiency obtained for SnS-based solar cells, obtained in 2014 is only 4.36%, which is too low while silicon-based solar panels can reach an efficiency ranges from 15%–17%[60]. The low efficiency of SnS-based solar devices arises due to a variety of reasons. One problem is secondary phases (e.g. Sn_2S_3) formed in the synthesis process. The Sn_2S_3 phase is unfavourable for solar cells due to its high resistance of over 10^5 Ω·cm, so the phase boundaries may act as recombination centres[47]. Besides phase boundaries, grain boundaries within the polycrystalline SnS can also function as recombination centres and result in low conversion efficiency. However, some researchers found SnS grain boundaries are actually tin-rich regions. Tin enrichment within the grain boundaries can form shunt paths when they are aligned perpendicularly to the surface of the substrate. A SnS seed layer before the deposition

of SnS absorber layer allows control of orientation of as-synthesised SnS crystals. Adjusting the orientation results in growth of SnS grains parallel to the surface of the substrate. Thus, the shunt path is disconnected and the efficiency will be improved. Although, the poor conversion efficiency of SnS-based solar cells was initially blamed on the poor film quality, including excessive secondary phases and grain boundaries, the intrinsic reason for the low conversion efficiency is probably the unique electronic structure of SnS. Sinsermsuksakul *et al.* mentioned in the report that, a "spike" like band offset is usually desired in case of solar cells, since it reduces recombination at the heterojunction between the absorber layer and buffer layer[46]. Additionally, the morphology of the buffer layer was also found to have impact on the performance of the cell. A solar cell based on a spherical TiO_2 electrode was found to be more efficient compared to the solar device based on nanocrystalline TiO_2, P25 nanoparticles and mesoporous TiO_2 films.

The approaches to improve the performance of SnS-based solar cells are summarised below:

- Annealing to reduce grain boundaries and secondary phases
- Controlling the orientation of SnS crystals to disconnect the shunt path along the grain boundaries
- Optimising the band offset by tuning the band position of the buffer layer

The second challenge is the irreproducibility of SnS-based solar cells, which means that the conversion efficiency of the solar cell degrades rapidly with time. In solar device applications, sulfur in SnS usually undergoes a self-oxidation process with the aid of photogenerated holes. To date, no effective solutions to the irreproducibility have been found and very few investigations have been done to seek possible solutions.

2.7 MoS_2-based solar cells

2.7.1 Structure of MoS_2

MoS_2 has three phases: a metallic 1T phase, and semiconductor 2H and 3R phases. Figure 24 shows the crystal structure of MoS_2 in each phase. The 2H-phase is the dominant form in which MoS_2 exists in nature because of better stability compared to 1T and 3R phases. Therefore, this review mainly focuses on the physical and chemical properties of 2H phase MoS_2 and its application in the solar cell field. The 2H-phase MoS_2 monolayer possesses a lamellar S−Mo−S structure with a thickness of ~ 0.7 nm, as shown in Figure 25. Each layer of MoS_2 consists of a hexagonal plane of Mo atoms and two hexagonal planes of S atoms modulated by covalent interactions in a trigonal prismatic form[61]. Adjacent layers are joined by van der Waals forces[61], as a result of which these weakly jointed layers can be exfoliated and synthesised as 2D materials with unique properties.

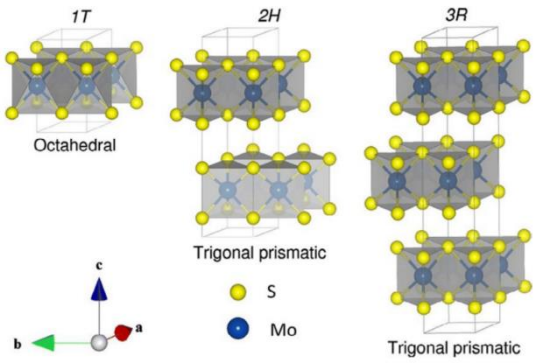

Figure 24 Schematic presentation of the crystal structures of MoS_2 in 1T, 2H and 3R phases, respectively[61].

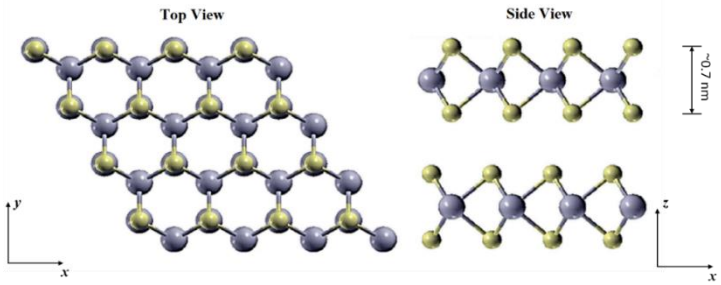

Figure 25 Schematic presentation of top view (left) and side view (right) of MoS_2 (2H and 3R phases) layers[62].

2.7.2 Preparation of 2D-MoS_2 nanosheets

2.7.2.1 Exfoliation

The successful exfoliation of graphene from bulk graphite by the "Scotch tape method" paves way for the fabrication of most 2D-structure materials such as MoS_2[63]. However, it is unsuitable for large-scale fabrication of 2D nanosheets because of the difficulties in controlling the sheet size and layer number[64]. Therefore, exfoliation through chemical approaches becomes the mainstream used to synthesise 2D-MoS_2 nanosheets. Through different methods, the composition of the MoS_2 layers obtained can be different. In 2011, H. Zhang's group reported that they successfully synthesised a high-yield single-layer MoS_2 film with 1T phase as the predominant phase using a lithium intercalation method[65]. Recently, a solvent-based exfoliation method, through which 2H phase MoS_2 was obtained, was first reported[66]. Chemical exfoliation provides an approach to produce large amount of 2D MoS_2 nanosheets. However, the sonication process will significantly reduce the size of the nanosheets obtained, and may induce defects in the structure and limit the application[64].

2.7.2.2 CVD synthesis

Chemical vapour deposition (CVD) is unable to produce MoS_2 nanosheets in as large scale as chemical solvent-based exfoliation, however, CVD allows the precise control of the thickness and size of the thin 2D-MoS_2 film fabricated. The precursors commonly used for the CVD of MoS_2 are Mo based compound powder[67,68], deposited Mo based film[69,70], ammonium thiomolybdates film[71] and MoS_2 powder[72].

2.7.3 MoS_2 in solar cell application

MoS_2 has great potential in solar cell applications[73], benefit from its good optical and electronical properties. Monolayer MoS_2 has a direct bandgap of 1.8 eV[74], while bulk MoS_2 has a bandgap of ~ 1.2 eV[75]. Because of the small bandgap MoS_2 possesses, it is

a good light absorber. Additionally, by adjusting the layer number, the bandgap of the MoS_2 can be modified, and the band alignment of the components in a MoS_2 solar cell can be therefore optimised[74].

However, it is difficult to produce large-scale continuous monolayer MoS_2 with good uniformity, and as a result, the development of monolayer MoS_2 based solar cells is limited. Therefore, compared to monolayer MoS_2, bulk MoS_2 has a greater potential in the field of solar cell application, due to the simplicity of forming thicker thin films[76–78] and the better light absorption ability[73]. In 2015, L. Hao *et al.* investigated the electrical and photovoltaic characteristics of MoS_2/p-Si junctions fabricated using magnetron sputtering technique[73]. MoS_2 thin films were deposited on p-type (100)–oriented silicon substrates using DC magnetron sputtering technique. The stacking structure of the photovoltaic device fabricated by the authors is shown in Figure 26. A *J-V* measurement of the Pd/MoS_2/p-type Si/In under dark condition was carried out and the result is shown in Figure 27. A dramatic increase of the current density is observed when the applied voltage is over 0.2 V, which indicates a rectification. The calculated rectifying ratio (I_+/I_-) measured at ± 0.5 V is approximately 42[73]. Figure 28 shows the *J-V* curves of the PV cell under both darkness and an illumination of 15 $mW \cdot cm^{-2}$. According to the calculation of the authors, the FF and PCE are 42.4% and 1.3%, respectively[73].

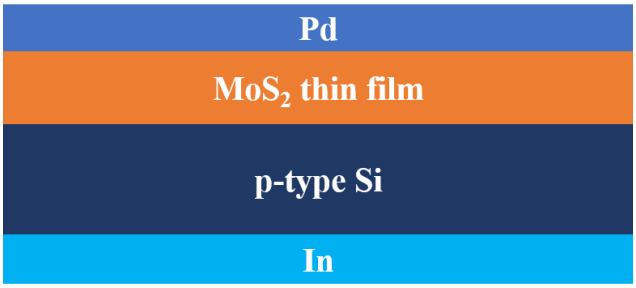

Figure 26 Schematic presentation of the stacking structure of the MoS_2/Si PV device.

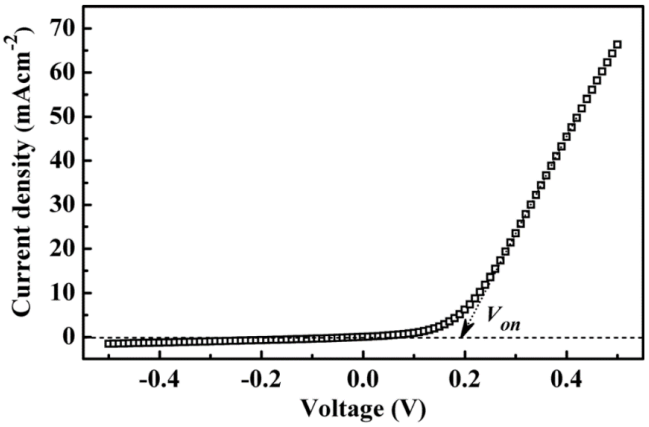

Figure 27 *J-V* characteristics of the n-MoS_2/p-Si junction[73].

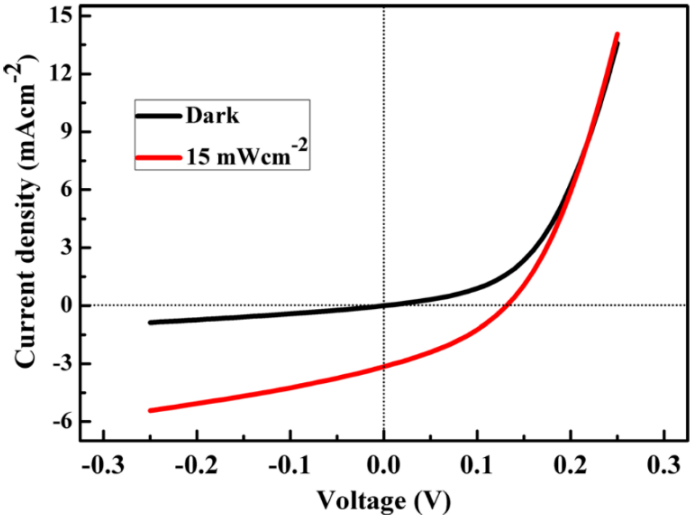

Figure 28 *J-V* characteristics of the MoS_2/p-Si PV device[73].

M. Tsai *et al*. successfully deposited monolayer MoS_2 layer on p-type Si substrates using CVD and obtained a solar cell with maximum PCE of 5.23%[79]. Figure 29 shows the stacking structure of the solar cell. A large size MoS_2 monolayer with a thickness ~ 0.65 nm synthesised using CVD method was transferred to the surface of the p-Si substrate and on top of it is an Al thin film. However, compared to Al/p-Si Schottky solar cells, the performance of the Al-contacted monolayer MoS_2/p-Si solar cell is improved only by a small amount[79] with a V_{OC} going from 0.38 to 0.41 V, J_{SC} from 21.66 to 22.36 mA/cm^2, and *FF* from 56.02% to 57.26%[79]. Therefore, even though the as-fabricated PV device shows an impressive PCE of 5.23%, the contribution of the MoS_2 monolayer to the PV device remains unknown.

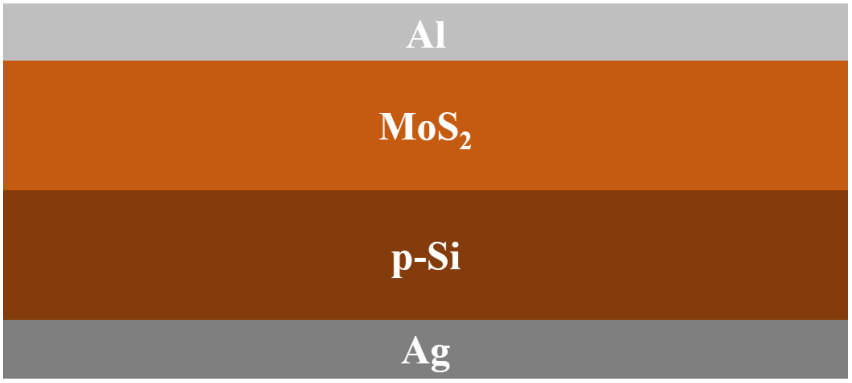

Figure 29 Schematic presentation of the stacking structure of CVD MoS_2 monolayer PV device.

MoS_2 is sometimes applied in solar cells as an "inorganic sensitiser[80]" or counter electrode[81]. T. Du *et al.* reported a heterostructure solar cell based on mesoporous TiO_2 substrate and MoS_2 "inorganic dye". As shown in Figure 30(a), mesoporous TiO_2 was deposited on FTO conducting glass, after which nanoscale MoS_2 was grown in the mesoporous TiO_2 three-dimensional network using CBD method[80]. A Pt-coated FTO was then placed on the MoS_2/TiO_2 heterostructure to act as counter electrode and I^-/I_3^- electrolyte was used for hole transport[80]. Figure 30(b) shows a schematic presentation of the band diagram of the as-fabricated cell. To allow the migration of photogenerated electrons to the substrate, the conduction band minimum of MoS_2 "inorganic dye" must be higher than the TiO_2 substrate. The valence band maximum of MoS_2 is also supposed to be higher than that of the TiO_2 substrate so that the photogenerated holes will stay in MoS_2 and then be extracted to the electrolyte. However, as a result of the large number of defects at the junction of MoS_2 nanosheets and TiO_2 substrate, recombination can occur. As a result, the efficiency of "inorganic dye" sensitised solar cells is limited[80]. Calculations suggested that the layer number has an impact on the position of the conduction band of MoS_2, while the valence band is unaffected[80]. As the layer number increase, the conduction band minimum of MoS_2 will shift to a lower position. Therefore, in order to maintain the band offset between the MoS_2 "inorganic dye" and the TiO_2 substrate, the layer number of MoS_2 requires to be controlled to within a few

layers. Figure 31 shows the UV-Vis absorption spectra of the porous TiO_2 thin film on the FTO glass, the as-prepared MoS_2/TiO_2 heterostructure and the MoS_2/TiO_2 heterostructure annealed at 300 °C. The UV-Vis absorption spectra testify that the sensitisation of pure TiO_2 by MoS_2 is effective and further enhanced by an annealing process at 300 °C. The authors presume that this further enhancement is due to that the small fragments distributed disorderly reform as larger crystals.

Calculations based on the *J-V* measurement results have shown that a PCE of 1.08% was reached[80]. Compared to organic DSSCs, the PCE of the solar device reported is very low. It is mentioned in the report that it is intrinsically difficult to reach comparable efficiencies with DSSCs based on "inorganic dyes", because unlike "inorganic dyes", organic dyes have the advantages of a better charge carrier transport between the dye molecules and the TiO_2 substrates, since organic dyes are chemically bonded to TiO_2 surface through the conjugated system between electron-donating group of dye and O^- of TiO_2[80]. In the report, the authors also attempted to deposit MoS_2 on the surface of bare FTO and a compact TiO_2 layer using the same method. It was found that, unlike mesoporous structured TiO_2 substrates, FTO and compact TiO_2 are unable to provide nucleation sites for the growth of MoS_2 nanosheets[80].

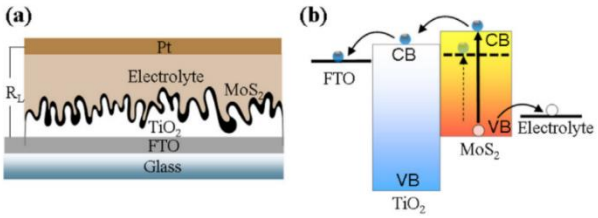

Figure 30 Schematic presentation of (a) the structure a solar cell based on mesoporous TiO_2 substrate and MoS_2 "inorganic dye", and (b) band alignment of each component of the solar cell[80].

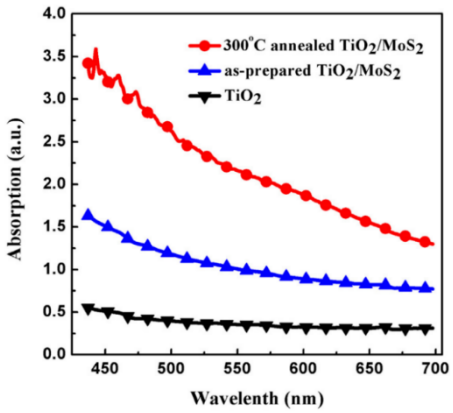

Figure 31 UV-Vis absorption spectra from 400 nm to 700 nm for pure porous structured TiO_2 thin film on FTO glass, as-prepared MoS_2/TiO_2 heterostructure and MoS_2/TiO_2 heterostructure annealed at 300 °C[80].

2.7.4 WS_2

WS_2 possesses similar electrical and optical properties to MoS_2, as a result of which WS_2 also has the potential in the area of photovoltaic applications. The crystal structure of WS_2 is also similar to that of MoS_2, as shown in Figure 32. It usually exists in nature in two phases: 1T metallic phase and 2H semiconducting phase. Monolayer 2H-phase WS_2 has a bandgap of ~ 2 eV, while bulk 2H-phase WS_2 has a bandgap of 1.35 eV[82].

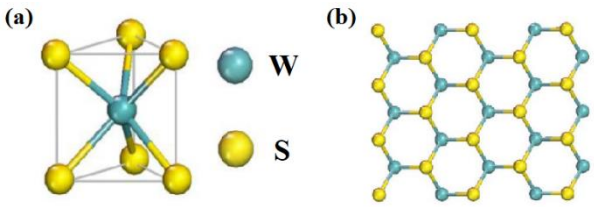

Figure 32 (a) Crystal structure of 2H-WS_2 unit cell. (b) Planar view of WS_2 monolayer[83].

S. Behura *et al.* fabricated a solar cell based on WS_2/p-Si heterojunction using CVD method[84]. The device exhibited a J_{SC} of 8.4 μA·cm^{-2}, a V_{OC} of 16.34 mV, and a *FF* of 26%, which are poor solar cell parameters compared to the solar cell based on MoS_2/p-Si heterojunction mentioned above[73,79,84].

2.7.5 Summary

In summary, both MoS_2 monolayer and bulk material have great potential in PV applications[73,79,80]. Tsai *et al.* successfully loaded monolayer MoS_2 onto the surface of

p-Si substrate. This MoS_2/p-Si heterostructure reached a high power conversion efficiency of 5.23%, while the effect of MoS_2 to performance of this heterostructure remains unknown[79]. MoS_2 can be also used as "inorganic dye" in DSSC devices[80]. However, the efficiency of the DSSCs based on inorganic dyes like MoS_2 are intrinsically difficult to reach an efficiency as high as DSSCs based on organic dyes, because inorganic dyes are unable to form chemical bonds with TiO_2 substrates as organic dyes do. WS_2 also possesses the potential to be applied in PV cells as light absorber. However, it is not as widely investigated as MoS_2.

3 Techniques

3.1 XPS (X-ray photoelectron spectroscopy)

3.1.1 Introduction

XPS is usually used for characterising the chemical composition and chemical states of the surface of solid specimen due to the very high surface sensitivity, although it can also be used for the characterisation of gases and liquids. XPS is a photoelectron spectroscopy (PES) technique. Ultraviolet photoemission spectroscopy (UPS) is another type of PES that is very widely used. UPS is usually used for the determination of the valence band structure. Generally, PES refers to the techniques based on the application of photoelectric effect[85] observed by Hertz and then thoroughly explained and manifested by Albert Einstein and his well-known photoelectric equation (Equation [1])[4].

$$E_{kmax} = h\nu - e\Phi_0 \qquad [1]$$

where E_{kmax} is the maximum kinetic energy of the photoelectron, $h\nu$ is the energy of incident photon, and $e\Phi_0$ is the work function which is related to the specimen surface.

Einstein suggested that electrons are able to surmount the potential barrier of the specimen surface and ejected into vacuum when sufficient energy is absorbed by the electrons[4]. It should be noticed that, in Equation [1], the kinetic energy of the photoelectron is referred to as a maximum value. This is because the energies required for electrons of different states to escape from the surface are different. Compared to electrons in the valence band, the inner-shell electrons are more tightly bound to the nucleus. Therefore, to escape from the constraint of the nucleus, core level electrons must absorb more energy than valence electrons. The binding energy can be considered as the energy needed to delocalise the electrons in a specific core level from the nucleus. In effect, it is a measure of how tightly an electron is bound in the emitting atom. The introduction of the term for binding energy, E_B, allows the kinetic energy of a photoelectron to be expressed by the following equation:

$$E_k = h\nu - E_B - e\Phi_0 \qquad [2]$$

Or in terms of binding energy,

$$E_B = h\nu - E_k - e\Phi_0 \qquad [3]$$

The kinetic energy of a photoelectron can be measured by an electron energy analyser in XPS, which makes the calculation from Equation [3] easy, since $h\nu$ is usually of a fixed value and $e\Phi_0$ is related to the surface of specimen. The XPS instrument also measures the number of photoelectrons emitted from the surface at a particular kinetic energy, and this intensity is proportional to the concentration of the element at the surface[86]. XPS spectra are then obtained by analysing the energy distribution of the photoelectrons escaping from the surface of specimen under illumination with photons of known energy.

3.1.2 Surface sensitivity of XPS

For an electron of intensity I_0 emitted at a depth of d below the surface, the intensity is attenuated according to the Beer-Lambert law[87]. Therefore, after the electrons are ejected to the vacuum, their intensity will depend upon:

$$I_S = I_0 e^{-\frac{d}{\lambda}} \quad [4]$$

where I_S is the intensity of the emitted electrons after escaping from the surface of the sample, I_0 is the initial intensity of the electrons, d is the depth from which the electrons are emitted, and λ is the inelastic mean free path of an electron in a solid (i.e. the average distance that an electron will travel before being scattered)[87].

The sampling depth can be defined by Equation [4], as the depth from which 95% of all photoelectrons are scattered before reaching the surface, so that the sampling depth is always equal to 3λ. For the most commonly used X-ray source, Al K_α radiation, λ is in the range of 1 – 3.5 nm. Therefore, only the electrons which originate within tens of Ångström below the specimen surface can escape without energy loss and therefore contribute to the peaks in the spectra. The photoelectrons originating from deeper positions below the specimen surface will undergo inelastic collisions with atoms in the solid. These photoelectrons increase the spectral background or contribute to secondary emission. This is the most important reason for the high surface sensitivity of XPS.

3.1.3 Basic principles of photoemission in XPS

As mentioned in the section above, XPS is a characterisation technique based on the photoemission process induced by soft X-rays. Photoemission refers to the process in which a photon of energy hv liberates an electron from an atom. Photoemission will change the state of the atom which absorbed a photon to the final state which can be considered as one where an electron is removed from the initial state of a system[88].

Therefore, the binding energy of an electron can be given by the energy difference between the initial state and final state. This is Koopman's theorem[89]:

$$E_B = E_i^N - E_f^{N-1} \quad [5]$$

where E_f^{N-1} is the energy of final state, and E_i^N is the energy of the initial state.

However, the E_B calculated based on Koopman's Theorem is usually 10 – 30 eV out, since Koopman's Theorem ignores the screening effects and the relaxation of ions following the photoemission process.

Figure 33 shows the X-ray photon induced emission process of an electron from the *1s* orbital of a carbon atom. The vacancy which results from the photoemission process, will then be filled by an electron from a higher energy level, which leads to either X-ray fluorescence or the emission of a secondary electron, namely an Auger electron, as described in more detail in Section 3.1.4.

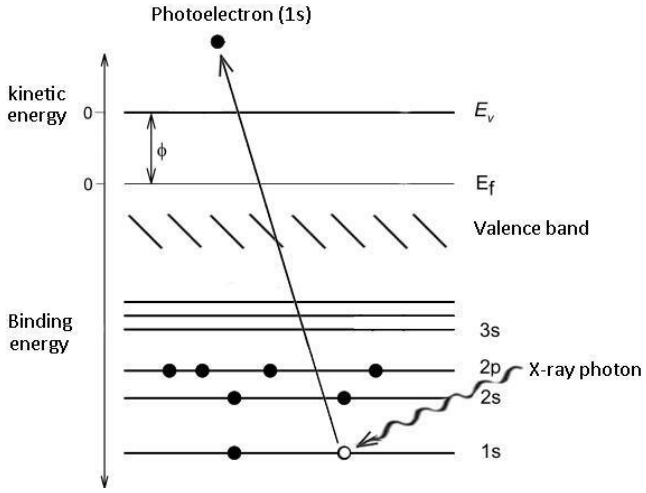

Figure 33 Schematic illustration of photoemission process[90].

The kinetic energy of the photoelectrons ejected is associated with the binding energy of the electrons. Considering the instrumental terms involved in the whole process from the photoemission to the detection of photoelectrons by the detectors, the relationship between the kinetic energy and binding energy is described by the following equation:

$$E_k = h\nu - E_B - E_R - e\phi_0 - \delta E \quad [6]$$

where E_R is the recoil energy which is a minor component of the calculation (0.01 – 0.1 eV). The value of E_R is always less than the uncertainties and therefore it is ignored. δE is the term that reflects the electrostatic charging of the specimen which will reduce the kinetic energy of the electrons ejected. This will cause a shift of the peak position towards higher binding energy. Fortunately, in most cases, the electrostatic charging is uniformly distributed across the specimen surface. Therefore, this shift of the peak position can be readily corrected by referring to a known standard peak position, for instance Au *4f*. However, since most samples which have been exposed to air are covered with a layer of adventitious hydrocarbon, it is convenient to calibrate for charging by correcting the C *1s* line to 285.0 eV for adventitious hydrocarbon[91].

3.1.4 Auger electrons

Following the emission of an electron from a core-level, a vacancy will be left in the corresponding orbital. An electron from a higher energy level may fall into the orbital to fill that vacancy and simultaneously energy will be released in this process, either in the form of photon, or more usually for low atomic number elements by emission of a secondary electron called an Auger electron. This process is called the Auger effect. A schematic presentation of the Auger effect is shown in Figure 34. Auger peaks are usually observed as broad peaks at low binding energies. They always appear at specific kinetic energies, since the kinetic energy of an Auger electron is only dependent on the

energy difference between the core level and the level from which the filling electron originated[92].

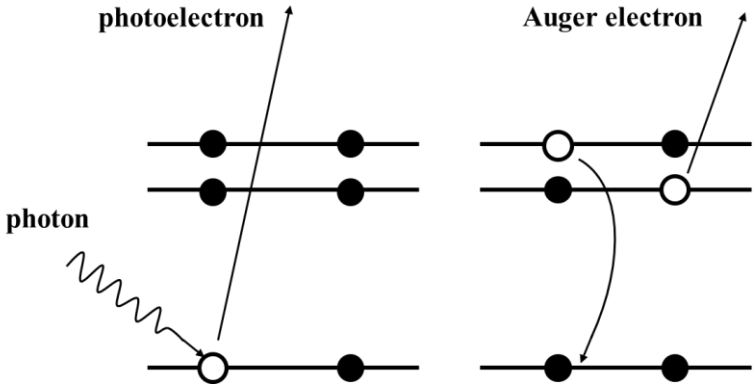

Figure 34 Schematic presentation of Auger effect.

3.1.5 Chemical shifts

The binding energy of a photoelectron is an intrinsic material property, and unrelated to the energy of the incident X-ray photon[88]. However, the exact binding energy of an electron is related not only to the orbital from which it is emitted, but also the chemical environment such as the oxidation state of the atom[88]. Atoms with a higher positive oxidation state usually show a higher binding energy since Coulombic interaction between the nucleus and the photoelectron is stronger compared to neutral atoms[88]. For instance, Figure 35 shows a simple representation of the electronic structures of Li atoms in (a) lithium metal and (b) lithium oxide. In Li-metal, the electrons in the *2s* orbital can be considered as freely dispersed within the metal. These *2s* electrons can screen the core hole caused by the photoemission process. However, in lithium oxide, in a simple ionic model, the *2s* electrons of lithium are donated into the *2p* shell of oxygen atom to form a complete $2p^6$ configuration. Therefore, without the screening effect from the *2s* electrons, the 1s electrons in Li atom of lithium oxide are more tightly bound to the nucleus, resulting in a higher binding energy for the *1s* electron in lithium oxide compared to lithium metal, and therefore a "chemical shift" is observed between

the two compounds[88]. Conversely, the binding energy of the O *1s* orbital for O^{2-} will shift slightly to lower binding energy relative to solid atomic O.

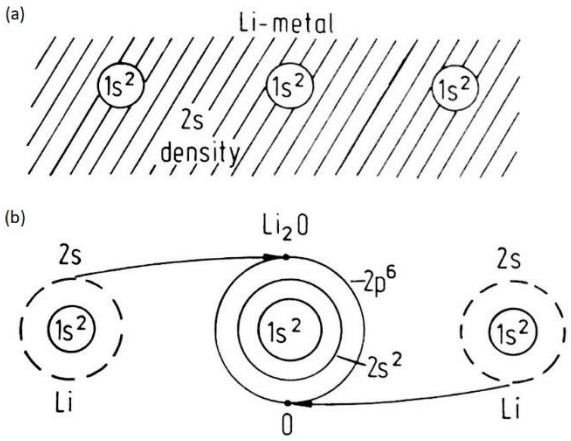

Figure 35 Schematic drawing of the electron configurations of lithium metal and lithium oxide[88].

Chemical shifts make it possible to identify the oxidation state of an atom, which makes XPS a powerful tool for the analysis of the surface chemistry of the material[88].

3.1.6 Satellites

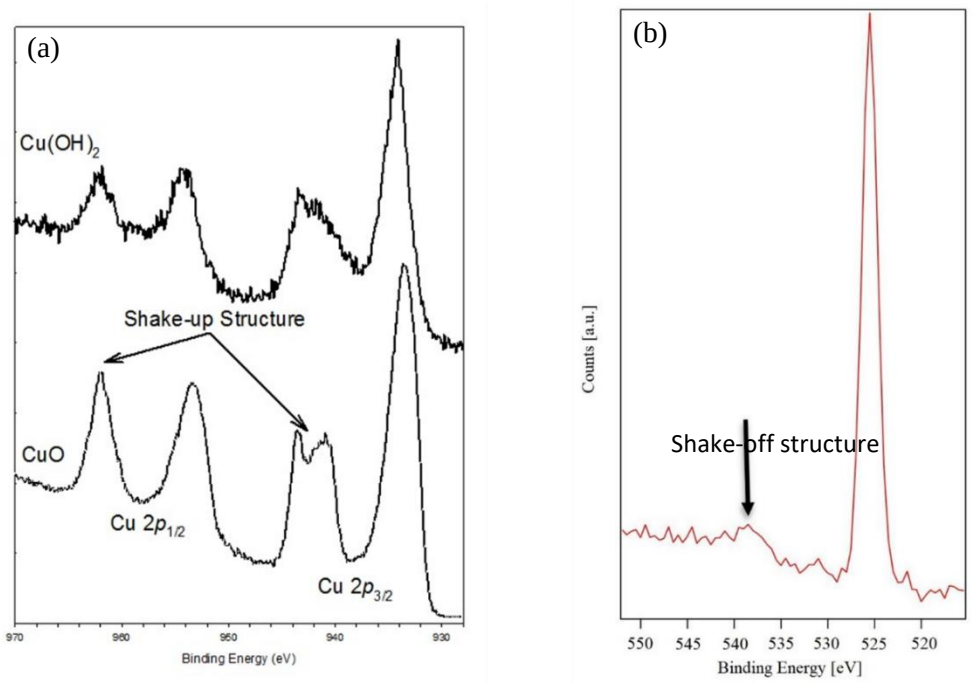

Figure 36 Example of (a) a shake-up structure (in Cu *2p* spectra of copper (II) hydroxide and copper (II) oxide)[93], and (b) a shake-off structure (in O *1s* spectra of a TiO_2 sample).

There are two main types of satellites. One type is X-ray satellites. X-ray satellites are a result of the emission from non-monochromatic X-ray sources[94]. The other type of

satellite originates from the material being analysed and include shake-up and shake-off satellites. They occur when outgoing photoelectrons undergo characteristic energy losses in the process of being ejected[95]. For some materials, there is a finite possibility that an ion can be left at a specific excited state which is several eV above the ground state when an electron is emitted from the core-level. The energy required to excite the ion from the ground state to the excited state is donated from the kinetic energy of an outgoing photoelectron. Therefore, the kinetic energy of the photoelectron detected by the instrument will be lower, and therefore, the binding energy will appear to be higher. Shake-up peaks can be found when a valence electron is excited to a higher unoccupied state by an outgoing electron (Figure 36(a)), for instance, an interband transition or excitation of a plasmon mode. The ejected electron loses a specific amount of kinetic energy in this process, which leads to a secondary peak at a higher binding energy than the main line[93]. Shake-off features can be observed when the valence electron is excited into the continuum rather than a defined energy level. Shake-off features (Figure 36(b)) usually appear as a broadening of the core level peak or contribute to a rise of the elastic background just above the core level peak.

3.1.7 Spin-orbital splitting

Spin-orbital splitting is an important method in assisting peak identification. The photoemission from any orbital where the angular quantum number $l > 0$ will not give rise to a single photoemission peak, but a doublet (as shown in Figure 37). Spin-orbital splitting is a final state effect. The removal of an electron at a certain level (e.g. *3p* or *3d*) will leave an electron in an unpaired state. This unpaired electron may align its spin parallel or anti-parallel to its orbital angular momentum, resulting in two possible final

states which arise due to the coupling between orbital angular momentum l and the electron spin s. The coupling is given by the symbol j, whose value is given by:

$$j = |l \pm s| \quad [7]$$

The total angular momentum number j for an electron in a p orbital can be either 1/2 or 3/2, since for p orbitals, l is 1 and s is ±1/2. For d orbitals, the value of j is either 3/2 or 5/2, since l = 2 for d-electrons.

The peaks also have specific intensity ratios dependent on the degeneracy of the two possible final states[88].

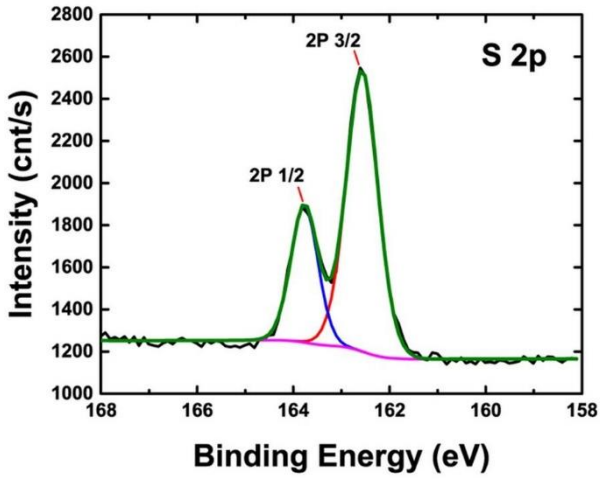

Figure 37 Example of doublet peaks due to spin-orbit coupling[96].

The degeneracy of one state can be calculated by:

$$g_J = 2j + 1 \quad [8]$$

where g_J is the degeneracy of the final state, and j is the total angular momentum number.

The intensity ratio between the peaks is actually the ratio between the degeneracy of the two possible final states, so the ratio between the doublet peaks is:

$$g_J\left(j=\frac{1}{2}\right):g_J\left(j=\frac{3}{2}\right)=1:2 \quad [9]$$

The intensity ratios between either *d* orbital peaks or *f* orbital peaks can be calculated using the same method.

3.1.8 X-ray sources

3.1.8.1 Lab based X-ray sources

On conventional non-monochromatic XPS apparatuses, X-rays are usually generated by a twin anode source within a system as shown in Figure 38. Electrons are thermally emitted from a heated filament and focused on the anode. Electrons collide with the anode material and induce the emission of X-ray. When a thermally generated electron hits on the anode material, an electron in the K shell may be excited to a higher energy level leaving a hole in the K shell. If an electron jumps down from L shell to fill in the hole, a Kα transition will occur. For an Al Kα X-ray source, the energy of a photon is 1486.6 eV which is high enough to excited core-level electrons in most materials commonly seen, and with a narrow linewidth of 0.85 eV[97].

In order to achieve higher resolution, the X-ray needs to be monochromated before probing the sample. A monochromator is made of a piece of quartz crystal and the structure is shown in Figure 39. The monochromatisation depends on the dispersion of X-ray energies by diffraction at a quartz crystal, as predicted by Bragg's Law[95]. A quartz crystal is toroidally bent to focus the monochromated X-ray on the sample[95].

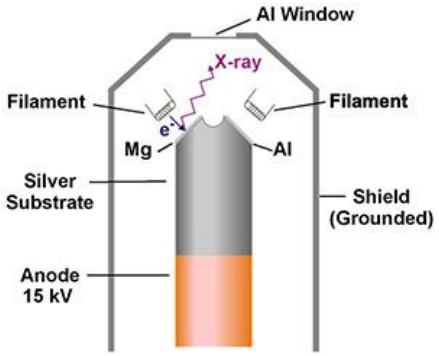

Figure 38 Schematic presentation of the structure of a Mg/Al twin-anode X-ray source[97].

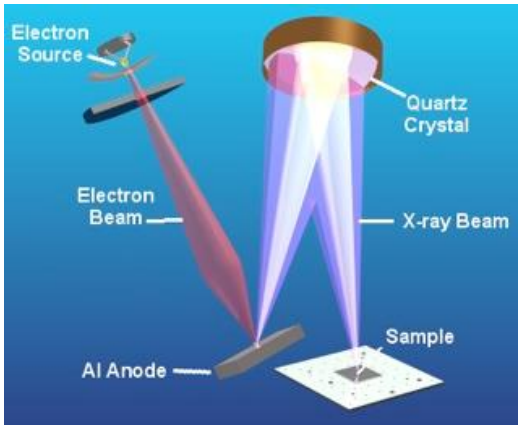

Figure 39 Schematic presentation of the structure of an X-ray monochromator[97].

3.1.8.2 Synchrotron radiation

Synchrotron radiation will be emitted along the tangential direction when charged particles travel along a circular orbit at a speed close to the speed of light. The synchrotron radiation has extremely high intensity and a wavelength range from infrared to hard X-ray spectrum.[98] Synchrotron radiation is generated in large facilities where several beamlines are arranged tangentially around a storage ring, as shown in Figure 40. Electrons are generated on a heated filament in the electron gun, and then accelerated by an electric field along a linear accelerator (LINAC). The primarily accelerated electrons will enter a booster synchrotron and be further boosted to relativistic speeds, and then be injected into the storage ring.

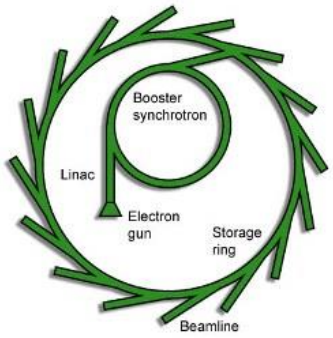

Figure 40 Schematic presentation of a synchrotron[99].

Modern storage rings consist of bending magnets to force the electrons into a circular orbit, and insertion devices in the straight sections. The latter force the electrons into a curved trajectory and are used to enhance the intensity of the emitted radiation. The radiation produced ranges from infrared to hard X-rays and is emitted in a well-defined arc tangentially to the ring. Beamlines are therefore placed around the ring and the radiation passes down the beamline. Various focussing mirror and optics are used to focus and monochromate the radiation. The major advantages of synchrotron radiation over lab-based sources are the fact that the wavelength of radiation is continuous so that photon energies can be chosen as required, i.e. the radiation is tuneable. In addition, the intensity of the light is much higher, although this may lead to problems with beam damage to the sample, particularly at the energies used for photoelectron spectroscopy. In this project, a portion of the experimental data shown in Chapter 5 was collected on Beamline I09 at Diamond Light Source, UK. Beamline I09 is designed for investigations of atomic and electronic structures of surfaces and interfaces. It can be used for photoelectron spectroscopy experiments and allows to access more absorption edges[100]. I09 provides both soft X-ray (230 – 2000 eV) and hard X-ray (2.1 – 18 keV). The end-station is equipped for ion sputtering and heating up to 1500K, which allows the in-situ preparation.

3.1.9 XPS instrumentation

Usually, ultra-high vacuum (UHV) (less than 10^{-9}mbar) is required in the XPS spectrometer to ensure the longest possible mean free path of the photoelectrons from the sample to the analyser, and to avoid contamination of the sample[92]. The sample is usually introduced through a pre-chamber with a load lock system which is linked to the external environment. The pre-chamber is then closed and pumped to low vacuum. When the pressure in the pre-chamber is low enough, the sample will be transferred into the main ultra-high vacuum chamber. The surface of the sample is then irradiated by soft X-rays.

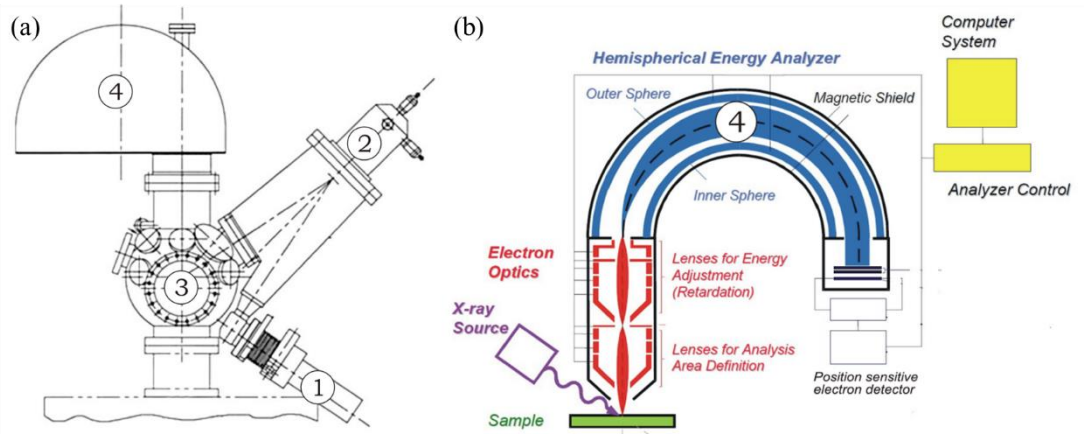

Figure 41 (a) A sketch of the XPS spectrometer: (1)X-ray source, (2)monochromator, (3)UHV chamber, and (4)hemispherical mirror analyser. (b) A schematic of operation of multichannel hemispherical analyser. Electrons are dispersed across the detector array based upon their kinetic energy[92].

Figure 41 shows the key parts of the XPS spectrometer. The part marked 1 is the X-ray source which generates X-rays with a certain energy. The X-ray enters a monochromator (the part marked 2 in Figure 41) which allows the production of X-ray beams with well-defined wavelength distribution. The incident X-rays are monochromatised by reflection from bent quartz crystals[92]. The electrons are then excited by the monochromatised X-ray which is focused onto the specimen surface. These excited photoelectrons travel through an electrostatic transfer lens system and then enter a hemispherical energy analyser (Part 4 in Figure 41(a)). As shown in Figure

41(b), a hemispherical analyser usually consists of a multi-element electrostatic input lens, a hemispherical deflector with entrance and exit slits, and an electron detector[92]. The electrostatic lens is employed to decelerate the electrons to the pass energy and focus them onto the entrance slit. A voltage is applied between the outer hemisphere and inner hemisphere of the deflector to provide the electrons passing through the analyser with a centripetal force. When a voltage of a particular value is applied, only the electrons which carry the "pass energy" are able to travel all the way through the analyser and be refocused back to the exit slit. The lenses for energy adjustment and the hemispherical energy analyser can be operated in two different modes, Fixed Analyser Transmission (FAT) or Fixed Retard Ratio (FRR)[101]. The difference between these two modes is the relationship between the pass energy ΔE which influences the energy resolution and the retarding potential E. In FAT mode, the pass energy of the analyser is fixed, and the retarding lenses play the role of decelerating the electrons so that the kinetic energy of the electrons passing through the analyser is fixed. By scanning the retarding potential of the lenses and counting the electrons detected by the detector, an XPS spectrum is obtained. This mode keeps a constant resolution over the entire spectrum. In FRR mode, the retarding potential of the lenses are also scanned while the ratio between the pass energy ΔE and retardation potential E is kept constant. Therefore, with the increase of the retardation potential, the resolution becomes lower due to the enlarged ΔE. This mode is typically used for Auger spectra, where intensity is more important than resolution[86].

The resolution of the hemispherical analyser $\Delta E/E$ is given by

$$\frac{\Delta E}{E} = \frac{0.63W}{R} \qquad [10]$$

where *W* is the entrance slit width and *R* is the radius of the analyser. This shows that for FAT mode, the resolution increases with larger analyser radius and smaller slit width.

3.2 Solar cell testing

3.2.1 Solar cell I-V characteristics and I-V curves

Solar cell *I-V* characteristic curves are a graphical description of the operation of a solar cell. They show how the current varies with the cell voltage, under defined operating condition and temperature[102,103]. Figure 42 shows an *I-V* characteristic curve of a typical silicon-based solar cell under standard test conditions.

3.2.2 Solar cell parameters

As seen in Figure 42, when the cell is in the open circuit condition, the voltage across the cell will reach a maximum, known as open-circuit voltage (V_{OC}). When the cell is in a short-circuited condition, which means the voltage across the cell reaches zero, the current flowing through the external circuit reaches a maximum, the short-circuit current[102] (I_{SC}). The I_{SC} of a specific solar cell is dependent on the intensity and the spectrum of the incident light. The I_{SC} is also dependent on the area of the solar cell. In order to get rid of the dependence on the solar cell area, short circuit current density (J_{SC}) is often used to describe the maximum current delivered by the solar cell[102]. Besides the intensity and the spectrum of the incident light, J_{SC} is also related to the optical properties of the solar cell base materials, such as the light absorption characteristics.

The V_{OC} is dependent on the photocurrent density (J_{ph}).

$$V_{OC} = \frac{k_B T}{q} \ln\left(\frac{J_{ph}}{J_0} + 1\right) \approx \frac{k_B T}{q} ln\left(\frac{J_{ph}}{J_0}\right) \qquad [11]$$

where the approximation is effective since J_{ph} is much larger than J_0. In Equation [11], k_B is the Boltzmann constant, T is the temperature, q is the charge[11]. Because the value of J_{ph} is relatively stable, the variation of J_0 is the dominating factor which affects the value of V_{OC}. J_0 can be referred to as a recombination parameter whose value is dependent on the recombination in the p-n junction[104]. Therefore, the value of V_{OC} actually reflects the amount of recombination in the solar cell[105–107].

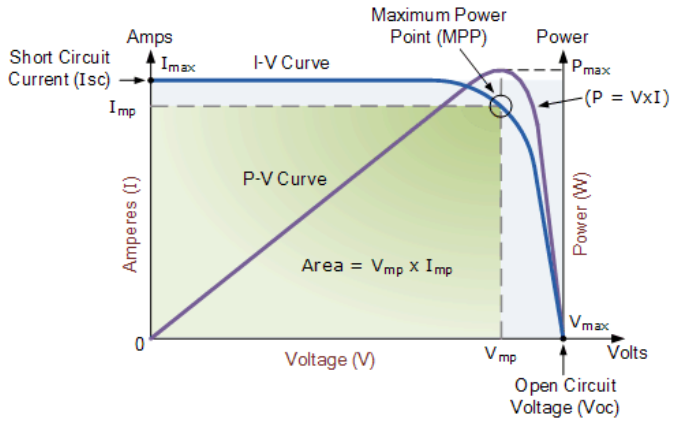

Figure 42 *I-V* characteristic curve of a silicon-based solar cell operating under standard test conditions (STC). The green rectangular area shows the maximum power possibly delivered by the solar cell under the condition. The *I-V* curve is marked in blue while the relationship between the power and the voltage is shown in the purple curve[102].

The power delivered by a solar cell equals the product of the voltage and the current, which can also be expressed as the area of the rectangle defined by the voltage axis, current axis and a point on the *I-V* curve, excluding short circuit and open circuit conditions. As shown by the purple curve in Figure 42, the power delivered by the solar cell increases with voltage across the cell and then reaches a maximum, after which the power output drops rapidly. The current and voltage which give the maximum power output are known as I_{mp} and V_{mp}, respectively. The point at which the cell delivers the maximum power is referred to as the maximum power point (MPP).

The fill factor is the ratio between the maximum power output and the product of I_{SC} with V_{OC}.

$$FF = \frac{I_{mp}V_{mp}}{I_{SC}V_{OC}} \quad [12]$$

In practice, the FF is often lower due to the presence of parasitic resistive losses.

The power conversion efficiency (PCE), η, is defined as the ratio between the maximum generated power and the input energy[108].

$$\eta = \frac{P_{max}}{P_{in}} = \frac{I_{mp}V_{mp}}{P_{in}} = \frac{I_{SC}\,V_{OC}\,FF}{P_{in}} \quad [13]$$

where P_{in} is the incident power.

The PCE is the key indicator of the performance of a PV cell. The PCE is primarily limited by the energy losses in the light absorption process and the recombination process of photogenerated electrons and holes, which means the efficiency can be improved by both enhancing light absorption and reducing recombination. The operating temperature of a solar cell is another factor which influences the PCE, since higher temperatures can change the properties of the semiconductor material, resulting in a slight increase in current, but a much larger decrease in voltage[109].

In this project, the solar cell parameter measurement was carried out by a solar simulator with a Xenon arc lamp under the AM1.5 condition (illumination intensity 100 mW/cm^2, cell temperature 25 °C).

4 Experimental

4.1 Preparation of TMC suspensions

For SnS suspensions: 0.5 g SnS powders (96%, Sigma-Aldrich) were diluted in 25 ml of 99.5% N-methyl pyrrolidone (NMP) and the mixture was sonicated in an Elmasonic P water bath at 37 kHz, 30% power for 24 h.

For MoS_2 suspensions: 0.4 g MoS_2 powders (98%, Alfa Aesar) were mixed into 20 mL NMP or 20 mL isopropanol (IPA), and then sonicated in a water bath at 37 kHz for 24 h. The same synthesis process was repeated to prepare WS_2 suspensions. In the process of sonication, all the suspensions were sealed in vials to avoid being exposed and oxidised by air.

4.2 Preparation of mesoporous/compact TiO_2 thin layer

An ITO-glass substrate (Ossila, 20 $\Omega \cdot sq^{-1}$) was placed in 2% Hellmanex solution and sonicated for 10 minutes. It was then cleaned in sequence using acetone and deionised water, and then treated in UV-Ozone for 15 minutes. To prepare the compact TiO_2 layer, the 0.1 M and 0.3 M precursor solutions were prepared by dissolving 100 µL and 300 µL titanium diisopropoxide bis(acetylacetonate) (75 wt%, in isopropanol, Sigma-Aldrich) in 2 mL 1-butanol, respectively. After being stirred for 30 minutes at a speed of 600 r/min, the 0.1 M precursor was spin-coated at a speed of 4000 r/min for 60 seconds onto the cleaned ITO substrate. The coated ITO substrate was then dried at 125 °C for 10 minutes. The same process was repeated for the 0.3 M precursor solution. The ITO-glass coated with TiO_2 precursor were then sintered in a furnace with a 30 min ramp from room temperature to 500 °C, and the temperature was held at 500 °C for 30 min, followed by natural cooling to room temperature. After the compact layer was formed, TiO_2 paste (Dyesol, 18NR-T) was diluted in ethanol at a 1:4 mass ratio and

stirred to a gel state. The gel-state paste was spin-coated at 5000 r/min for 30 seconds onto the compact TiO_2 layer. The thin film was dried at 125 °C for 10 min and the film was sintered again to 500 °C roughly in the formation of mesoporous TiO_2[110].

4.3 Deposition of TMCs on TiO_2 substrate

The deposition of TMC materials onto the TiO_2 substrate was done by simply soaking mesoporous/compact TiO_2 thin films in the as-prepared TMC suspensions at room temperature for differing times from 3 hours to one week.

4.4 Fabrication of solar cells based on SnS/TiO_2 structure

After the deposition of TMC materials onto the TiO_2 substrate, a thin layer of Spiro-MeOTAD(2,2',7,7'-tetrakis-(N,N-di-4-methoxyphenylamino)-9,9'-spirobifluorene)[111] was deposited as hole transport material. First, a Li-TFSI solution was prepared by dissolving 520 mg Li-TFSI in 1 mL acetonitrile (ACN). 40 mg Spiro-MeOTAD powders was added into 0.5 mL of 99.8% chlorobenzene (CB) and mixed with the as-prepared Li-TFSI solution and 15 µL 4-tert-butyl pyridine (TBP). The obtained mixture was stirred until it became an even solution, which was then spin coated onto the SnS/TiO_2 structure at a speed of 4000 r/min for 30 s. To fabricate a complete solar cell structure, a thin layer of Au was deposited as back contact using thermal evaporation. A schematic presentation of the as-fabricated solar cells is shown in Figure 43.

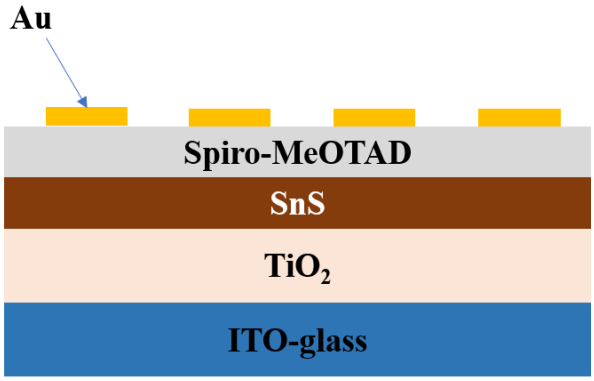

Figure 43 Structure of the as-fabricated SnS/TiO_2-based solar cell.

5 Investigation of the use of SnS as a sensitiser for 2-D chalcogenide solar cells

In order to investigate the effect of soaking time on the power conversion efficiency of SnS/TiO_2 solar cells, three mesoporous/compact TiO_2 thin films were soaked in the as-prepared SnS suspension for 1 week, 12 hours, and 3 hours, respectively. The containers used for storing the SnS suspensions and carrying out the dip-coating process were tightly sealed to reduce exposure of the suspension to air. The SnS-soaked TiO_2 films were then used for fabricating solar devices as introduced in the previous section. The solar devices were then tested by solar simulators under illumination with an AM1.5 simulator with a power of 100 mW/cm^2. On the other hand, a set of "copies" of the three SnS-soaked TiO_2 films were made for a parallel XPS analysis.

5.1 Results of solar simulation and analysis

On each as-fabricated solar device, eight individual sub-cells were distributed and numbered as shown in Figure 44.

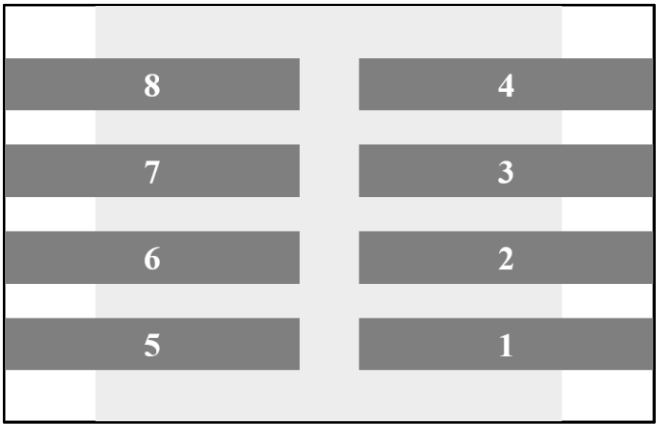

Figure 44 Schematic presentation of the planar view of the as-fabricated solar cell. Small dark grey grids represent Au deposited area. The large light grey area represents the Spiro-MeOTAD/SnS/TiO_2 structure.

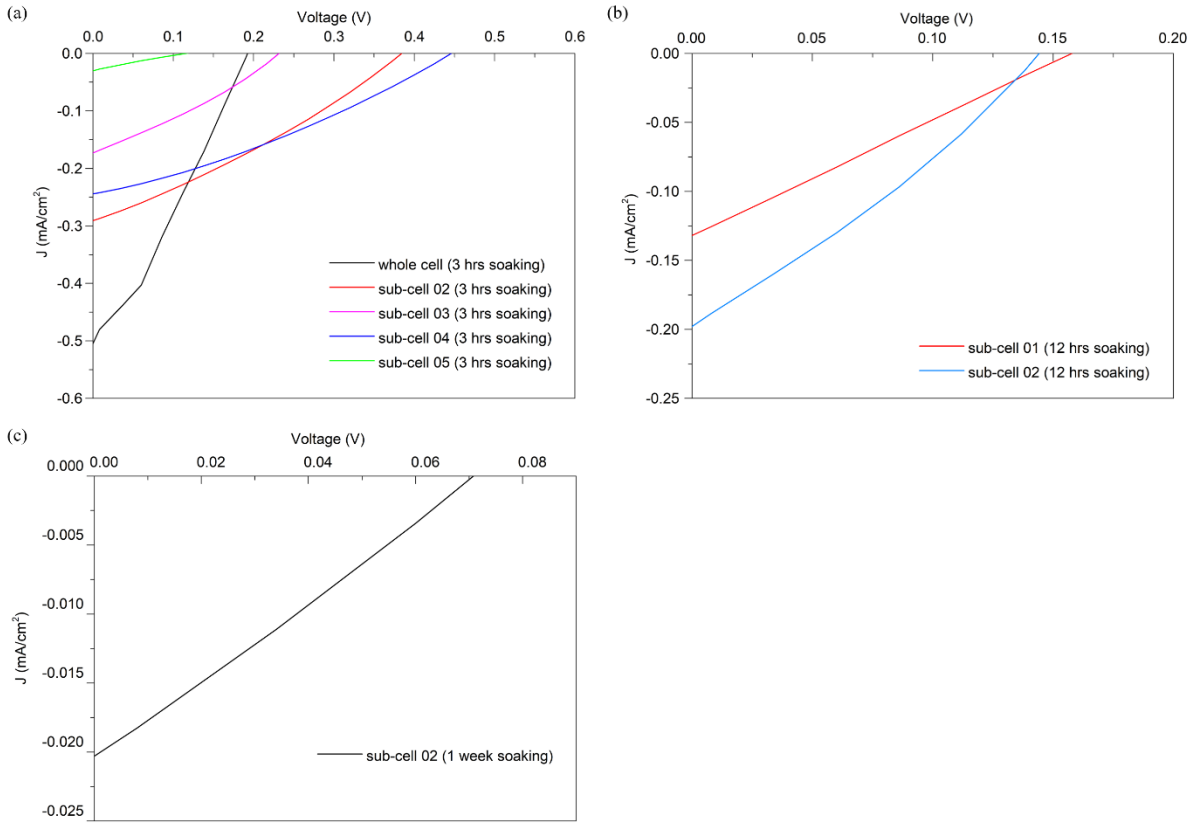

Figure 45 *J-V* curves of the subcells with PCE > 0% on solar devices based on (a) 3-hour-depositied SnS thin layer, (b) 12-hour-deposited SnS thin layer, and (c) one-week-deposited SnS thin layer.

Table 3 Solar cell parameters of the as-fabricated solar cells and the subcells.

Solar device	Subcell	J_{SC} (mA/cm^2)	V_{OC} (mV)	FF	PCE of subcell	PCE of solar device
3-hour-soaked	02	0.29	384.2	30.1 %	0.03 %	0.03 %
	03	0.17	231.6	30.0 %	0.01 %	
	04	0.24	446.1	31.6 %	0.03 %	
	05	0.03	60	21.8 %	0.00 %	
12-hour-soaked	01	0.13	157.7	24.7 %	0.01 %	0.00 %
	02	0.20	144.2	29.2 %	0.01 %	
One-week-soaked	02	0.02	70.8	26.3 %	0.00 %	0.00 %

The *J-V* characteristics of each sub-cell and each solar device were measured using a solar simulator. The *J-V* measurements showed that most of the sub-cells have PCE of 0%. The *J-V* curves of all the sub-cells with PCE > 0% are shown in Figure 45 and the

solar cell parameters of these sub-cells are measured. The result of the calculations is summarised in Table 3. According to the calculation, only the 3-hour-soaked sample exhibits a PCE of 0.03%, while the other two solar devices show PCEs of 0%. Therefore, the results obtained from the *J-V* measurement suggest that longer soaking time produces lower efficiencies. The results also show that there are two sub-cells with 0.01% efficiencies on the 12-hour-soaked solar device, while on the one-week-soaked solar device, all the sub-cells show 0% efficiencies. Taking the efficiencies of subcells of the solar device into consideration, this further confirms that the performance of the as-fabricated solar cell PCE degrades with increased dip-coating time. Additionally, the results of the *J-V* measurement show that on the 3-hour-soaked device, three adjacent subcells, Subcell 02, 03 and 04 have PCEs > 0%, and on the 12-hour-soaked device, two adjacent subcells, Subcell 01 and 02 have PCEs of 0.1%. It appears, therefore, that on each solar device, the subcells with better performance are located adjacently.

There are a number of reasons why the soaking time may have a negative effect on the performance of the fabricated solar cells. Firstly, SnS may simply not be able to transfer charge to the TiO_2 substrate. Secondly, the SnS may degrade or oxidise over time, and finally, there may be some competitive adsorption process which over time displaces SnS from the surface. It is also found that in Figure 45(a), even on the same solar device, the sub-cells have very different performance. The differences between the solar cell parameters of the sub-cells probably indicate an uneven distribution of SnS molecules on the TiO_2 substrate. In other words, in some areas, many SnS molecules are adsorbed on the TiO_2 substrate, but in other areas, few SnS molecules are adsorbed. Therefore, the effect of SnS in different areas are different, and as a result, the performance of the sub-cells is different from each other. For the 3-hour-deposited SnS thin layer, the deposition time may be insufficient for SnS to fully cover the TiO_2 substrate. Because

of the insufficient deposition time, the TiO_2 substrate was left exposed after the dip-coating process in some areas, and in the other areas, only a small amount of SnS was deposited. It means that the negative effect of SnS on the performance of the sub-cells situated in these areas is very limited. In other words, Subcell 02 and Subcell 04 are the least affected by SnS, so they show the best performance. In the area where Subcell 03 is located, more SnS molecules are deposited so that the performance of Subcell 03 is affected by SnS and it shows an efficiency lower than Subcell 02 and Subcell 04. In other subcells on the 3-hour-soaked solar device, the efficiencies are 0% since many SnS molecules are deposited in the areas where these subcells are located. For the 12-hour-soaked solar device and one-week-soaked solar device, the soaking time is long enough to allow SnS to fully cover the TiO_2 substrate, so the subcells on the two devices have PCEs of 0% or very close to 0%. The idea illustrated above can also explain why all the subcells with better performance on each solar device are located adjacently.

As mentioned above, there are three possible reasons for the negative effect of SnS on the performance of the as-fabricated solar device. One of them may be that the contact between the SnS layer and other layers is ineffective, hence, the charge carrier transport between the SnS layer and TiO_2 substrate is hindered. The other possible reason is inappropriate band alignment between the SnS layer and the TiO_2 substrate, which has been reported for thin film solar cells[49]. Finally, the SnS may degrade over time.

In order to assess the effect of band alignment between SnS and TiO_2, valence band photoelectron spectroscopy has been carried out. The valence band spectrum of a clean anatase (101) TiO_2 single crystal is measured using synchrotron radiation valence-based photoelectron spectroscopy and the result was shown in Figure 46(a). Anatase was used as it is the phase of TiO_2 thought to be present in mesoporous titania. A drop of SnS suspended in IPA was added to the sample and the valence band spectrum was

measured again after the solvent has been removed. The valence band cut off is measured from the spectrum as shown in Figure 46(a). Knowing the band gap of the two materials (TiO_2: 3.2 eV and monolayer SnS: 1.6 eV), we can calculate the band alignment as shown in Figure 46(b)[28,112]. A small tail is observed on the valence band spectrum of anatase between BE 0 – 3.1 eV by the lower energy side of the valence band peak as shown in Figure 46(b). This is due to the fact that, in anatase TiO_2 (101) single crystals, oxygen vacancies are easily created under a synchrotron beam. This leads to the creation of in-gap states between the valence band maximum and the Fermi level[113]. Figure 46(b) also shows that the interface between SnS and TiO_2 has a type II offset. Therefore, the SnS component should be able to enhance the light absorption and the charge carrier separation should not be hindered. The reason for the negative effect of soaking time to the performance of the solar device is therefore more likely related to the poor contact between SnS and the TiO_2 substrate.

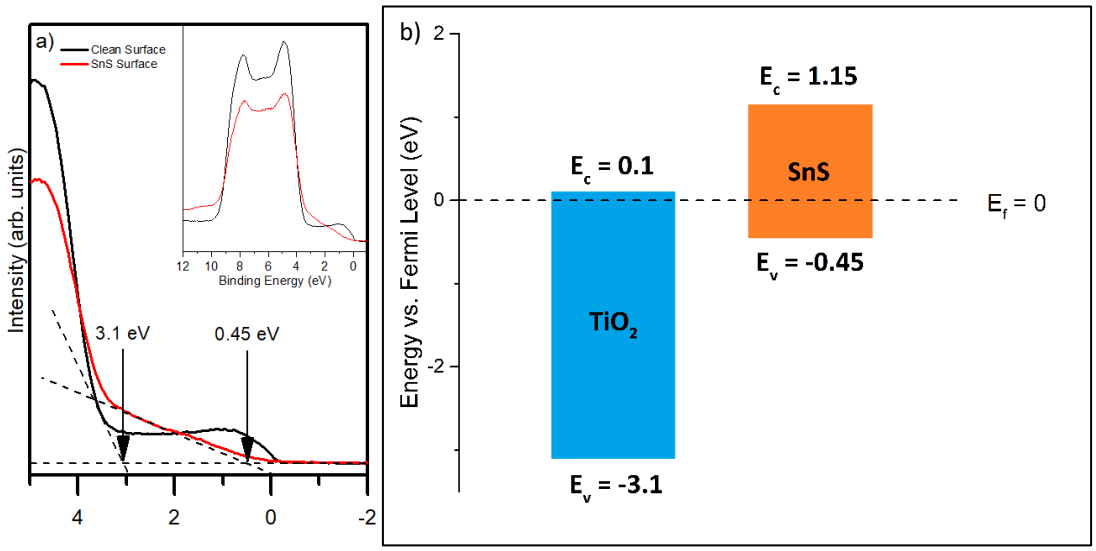

Figure 46 (a)Valence band spectra of SnS/anatase. Inset image shows the valence band spectra from BE 0 – 12 eV. (b) Band alignment between TiO_2 substrate and SnS sensitiser[28,112].

5.2 XPS results and analysis

In order to further investigate the SnS/TiO_2 interface and the chemistry of the SnS overlayer, XPS was employed to study the uptake of SnS for the different soaking times.

(a)

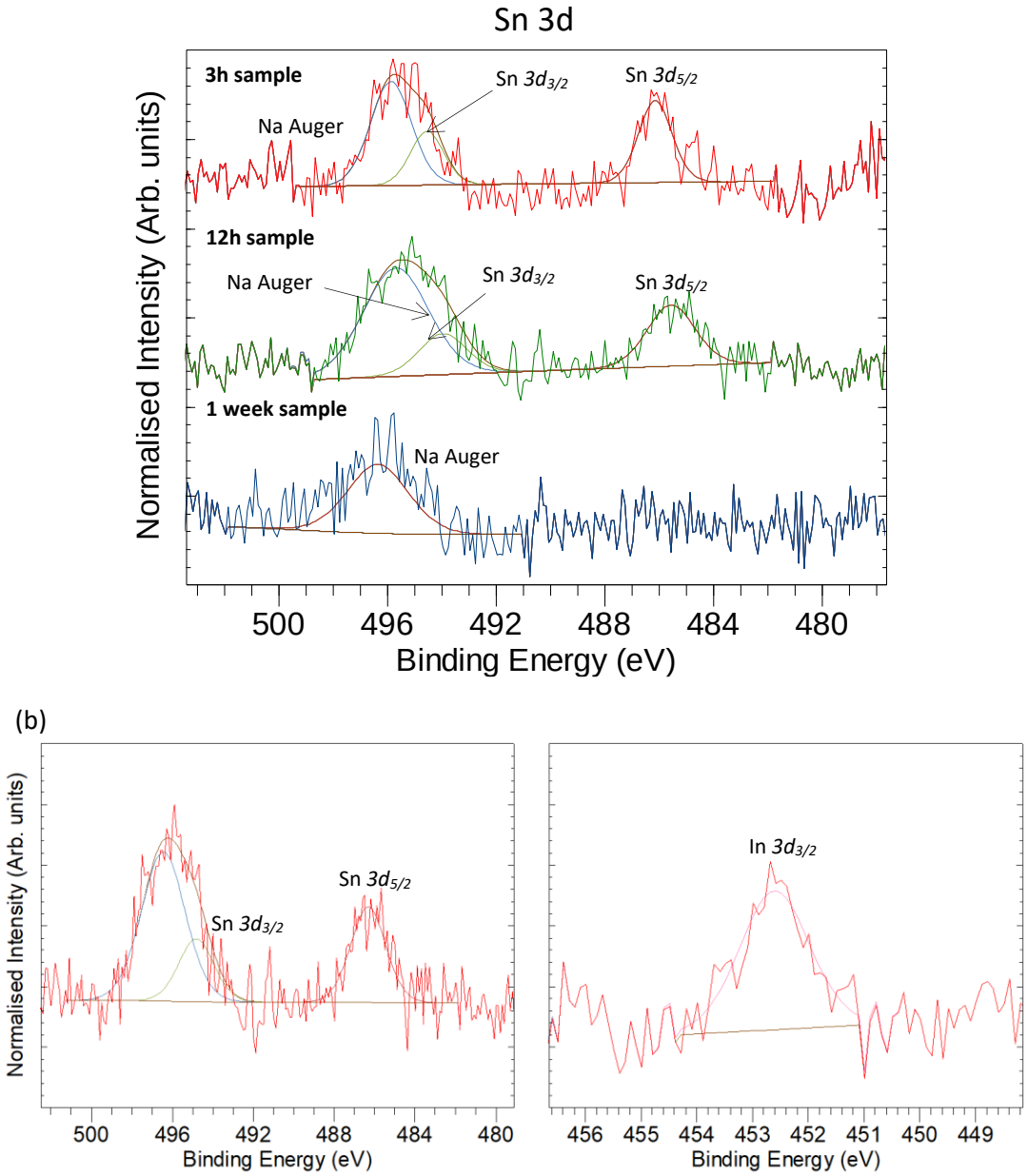

Figure 47 (a) XPS spectra and the fitted curves of the Sn *3d* region for 12-hour-soaked sample, 3-hour-soaked sample and 1-week-soaked sample. The component each fitted curve represents to is labelled above the peak or with an arrow pointing to the corresponding fitted curve. (b) Comparison of XPS spectra for Sn *3d* and In *3d* peaks of 12-hour soaked sample.

S 2p

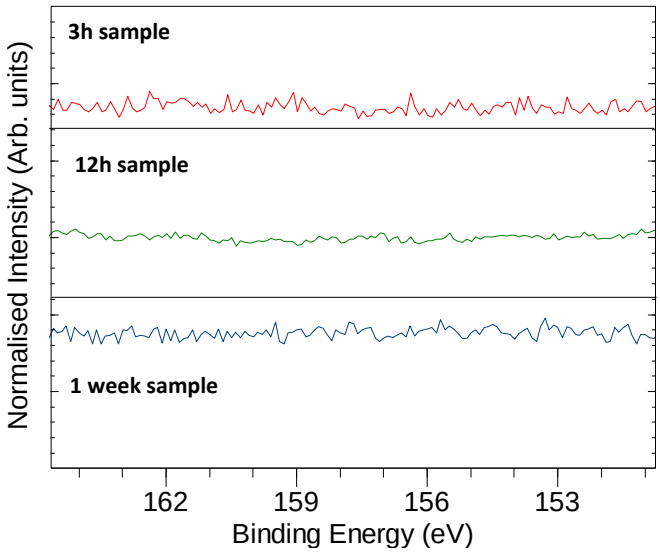

Figure 48 XPS spectra of S *2p* curves for 12-hour-soaked sample, 3-hour-soaked sample, and 1-week-soaked sample.

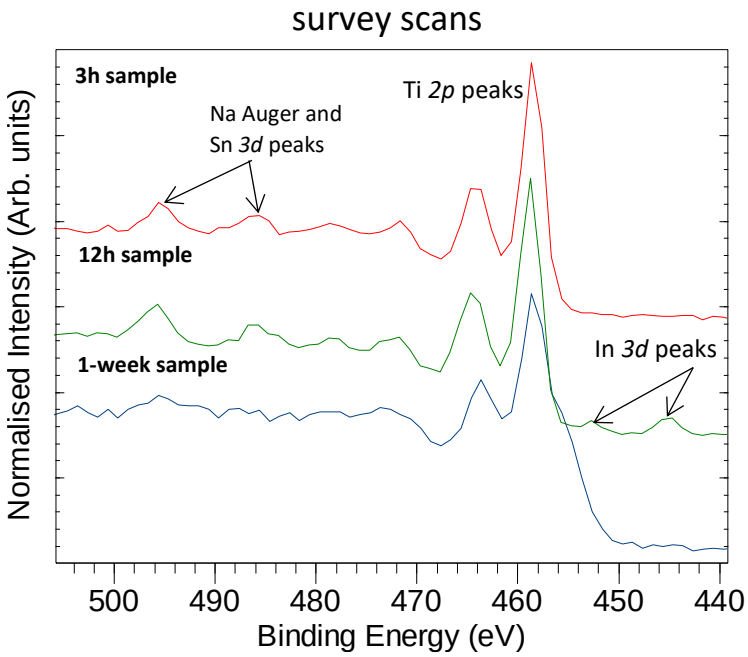

Figure 49 XPS survey scan spectra of the three samples in the Ti *2p* and In *3d* region (BE range from 424 – 510 eV)

Table 4 Atomic ratio of Sn (from SnS) and Ti for the 3-hour-soaked and 12-hour-soaked samples.

Sample	at %	
	Sn	Ti
3-hour-soaked	2.39%	97.61%
12-hour-soaked	4.69%	95.31%

Figure 47 shows Sn *3d* curves and fitting results of the three samples soaked for different time lengths. The XPS spectra displayed in this section are calibrated by adjusting Ti $2p_{3/2}$ peak to a BE of 458.7 eV[114]. On the 3-hour-soaked and 12-hour-soaked samples, Sn $3d_{5/2}$ peaks are identified at a BE of ~ 486 eV[115]. The BEs of the peaks are consistent with previous work[116]. No Sn signal is detected on the 1-week-soaked sample shown in Figure 47(e), however, all spectra show a significant Na Auger peak at a BE of ~ 496 eV[117], which overlaps with the Sn $3d_{3/2}$ peak. This implies the existence of Na containing contamination which is probably introduced into the SnS suspension during the preparation. Similar Na contamination was observed in SnS samples used in the VB spectra described above. The XPS spectra of sulfur for the three samples are shown in Figure 48. It is clear that S *2p* peaks are not observed for any of the samples in Figure 48. No evidence for the existence of either sulfide (S *2p* BE ~ 161.5 eV)[118] or sulfate (S *2p* BE ~ 169 eV)[118] is observed, which is unexpected. The most likely reason for the missing of S *2p* peaks is that SnS 2D-materials are oxidised to form tin oxides after being exposed to air. It is shown in recent work that after a long-time exposure in air, SnS nanocrystals will be oxidised to form SnO_2 rather than form tin sulfate[119]. In addition, in our own studies of MoS_2 and WS_2 discussed in Chapter 6, it appears that TiO_2 may catalyse the oxidation of TMCs. It also seems that the choice of solvent may accelerate this oxidation process. This might also explain the poor efficiency obtained in the prototype cells. The missing S peak may also be a result of the fact that SnS is not attached to the surface of the TiO_2 substrate and the Sn signals detected come from the ITO glass which contains Sn. However, as shown in Figure 49, indium *3d* peaks can only be found in the survey scan spectrum of the 12-hour-soaked sample. This indicates that the ITO glass as the main source of the Sn element detected by XPS is unlikely. Another possible reason for the missing S peak may be that, the

photoemission cross section for S is low, and it typically requires long acquisition time to obtain good-quality S *2p* spectra. It is possible that in this case, the acquisition time is insufficient for obtaining good signal-to-noise ratio[118]. The missing Sn $3d_{5/2}$ peak in the spectrum of the 1-week soaked sample suggests that the SnS may not be attached to the surface of the TiO_2 substrate for reasons discussed later in this chapter.

Ti *2p* peaks are also identified in the spectra obtained as shown in Figure 50. The doublet splitting between the Ti(IV) $2p_{3/2}$ peak and Ti(IV) $2p_{1/2}$ is set to be 5.8 eV according to the literature[120,121]. To optimise the fitting, the FWHM of the Ti(IV) $2p_{1/2}$ peak is constrained to be ~ 2 times as the FWHM of the Ti(IV) $2p_{3/2}$ peak[120]. The shoulder which appears between the two peaks in the 1-week-soaked sample, at a BE of ~ 460 eV, is due to differential charging of the sample, which could not be removed by the use of the low energy flood source. As mentioned above, in the spectrum of 12-hour-soaked sample, an In $3d_{3/2}$ peak was found, which indicates the ITO substrate also contributes to the Sn detected. In order to confirm the amount of Sn that comes from SnS, the atomic ratio between Sn/In was calculated to be 1:1.22 based on fitting results shown in Figure 47(b). Since the composition of ITO is normally SnO_2:In_2O_3 = 1:9 [122], it can be calculated that about 7% of the Sn detected in total come from the ITO substrate. The approximate quantity of Sn in each sample is calculated based on the XPS spectra and the result of the calculation is shown in Table 4. The quantity of Sn on the 1-week-soaked sample cannot be measured since Sn *3d* peak is missing in the spectrum. Additionally, from the broadened Ti *2p* peaks in the spectrum of the 1-week-soaked sample, it is seen that the sample had severe differential charging which makes it impossible to carry out precise fitting. The Sn atomic percentage of the 12-hour-soaked sample is approximately 2.3% more than that of the 3-hour-soaked sample,

which may suggest that a longer soaking time will lead to a better deposition of SnS on the TiO_2 substrate, up to a point.

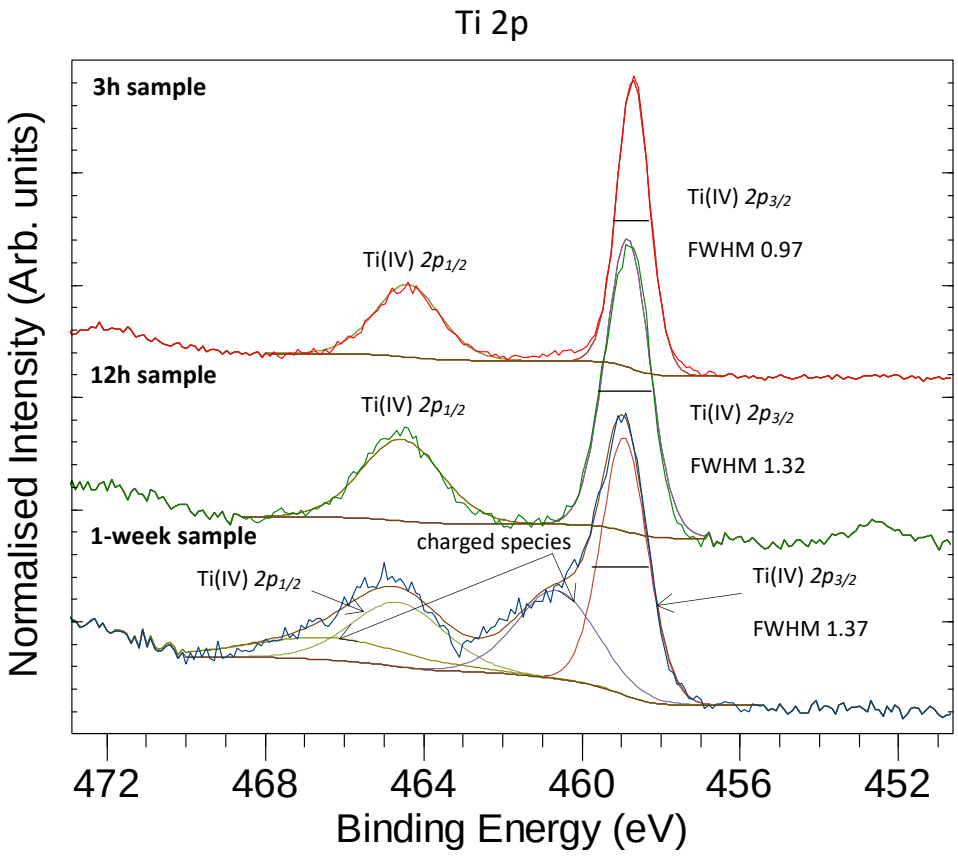

Figure 50 XPS spectra of the Ti *2p* curves and fitted curves for 12-hour-soaked sample, 3-hour-soaked sample, and 1-week-soaked sample. The component each fitted peak represents is labelled next to it or indicated with an arrow pointing to the corresponding fitting curve. The FWHM of the Ti $2p_{3/2}$ peak of each spectrum is labelled, respectively.

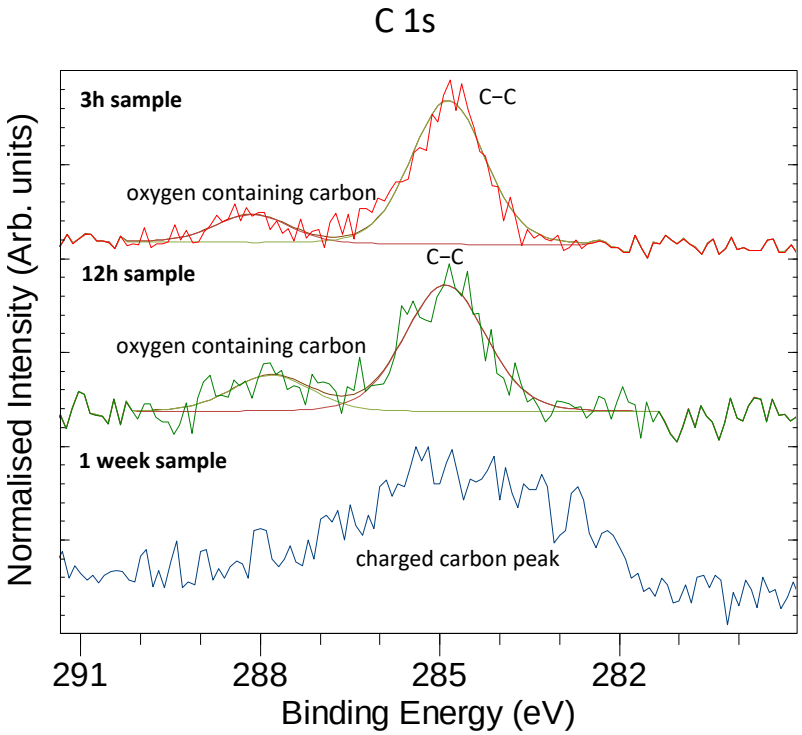

Figure 51 XPS spectra of the C *1s* curves and fitted curves for 12-hour-soaked sample, 3-hour-soaked sample and 1-week-soaked sample. The component each fitted peak represents to is labelled next to it. The C *1s* peaks are adjusted on the BE scale to hydrocarbon peak at 284.8 eV[123].

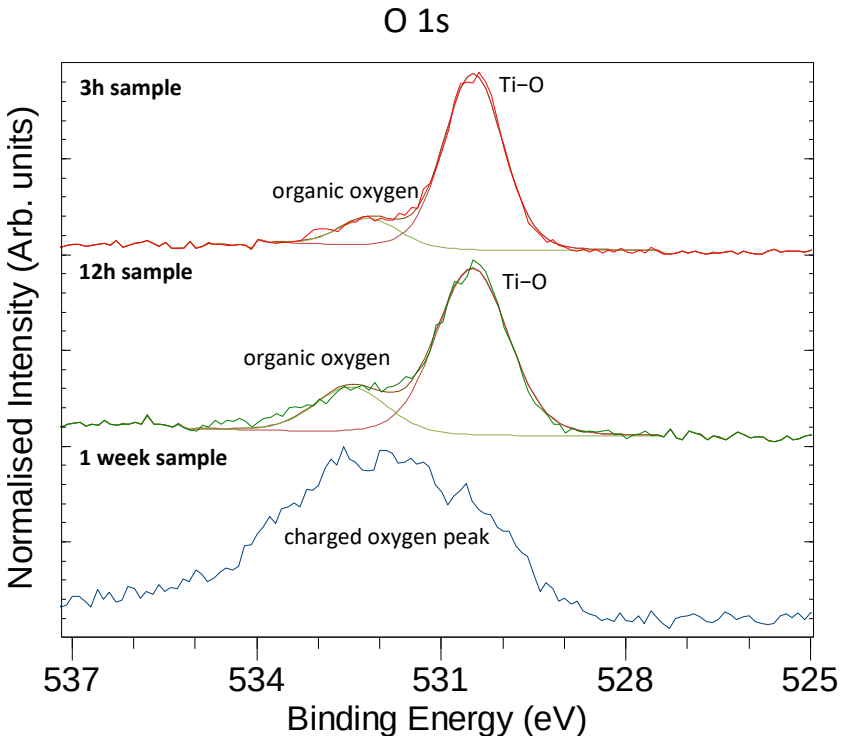

Figure 52 XPS spectra of the O *1s* curves and fitted curves for 12-hour-soaked sample, 3-hour-soaked sample and 1-week-soaked sample. The component each fitted peak represents to is labelled next to it. The O 1s spectra are aligned on the BE scale to 530.5 eV which corresponds to O *1s* in Ti–O bonding[124].

Figure 51 and Figure 52 show XPS spectra of C *1s* and O *1s* curves, respectively, for the three samples. It is seen in Figure 51 and Figure 52, the C *1s* and O *1s* peaks in the spectrum of the 1-week-soaked sample are broadened heavily because of charging. Combined with the differential charging observed in the Ti *2p* spectrum of the 1-week-soaked sample, we can infer that a long-time soaking process leads to a severe charging in the XPS spectrum. A long soaking time could give the NMP solvent enough time to attach to the surface of the TiO_2 substrate. NMP has a carbonyl oxygen, which could bind to the TiO_2 surface, and is an insulator which may induce charging. It is also possible that the TiO_2 film soaked for 1 week has poor adherence to the ITO substrate which would also lead to increased charging. It is not clear from the data here whether this poor adhesion is due to the soaking or just an artefact of this particular film. In the C *1s* spectra of the 3-hour-soaked and 12-hour-soaked samples, a small component corresponding to oxygen containing carbon is observed next to the main C *1s* peak. In the C *1s* spectrum of the 12-hour-soaked sample, the ratio of the area of the small peak to the C−C derived peak seems to be greater than it is in the C *1s* spectrum of the 3-hour-soaked sample. A similar trend is also found in the O *1s* spectra in Figure 52. A minor component sits at higher BE relative to the major oxide O *1s* peak. It should also be noticed that, for the 12-hour-soaked sample, the ITO substrate will contribute to the O *1s* spectra. However, according to the calculations, oxygen from ITO substrate only contributes about 0.2% of the total oxygen atoms detected by XPS facility. With such a small amount, it is unlikely to affect the O *1s* spectra significantly. The FWHM of the peak increases, consistent with charging after 1 week of immersion. The source of carbon atoms detected may be from the NMP solvent left on the sample or adventitious carbon from the atmosphere, but the C−O species are consistent with NMP. The approximate content of carbon containing contamination is obtained by calculating the

atomic ratio of Ti, C, and O. The result is shown in Figure 53(a). The result shows that the atomic ratio of each component is roughly stable from sample to sample, with the carbon containing contamination content also consistent with soaking time. However, if one considers the atomic ratio between C−C and oxygen containing carbon components, it is seen that the nature of the carbon containing contamination changes with soaking time. Figure 53(b) shows the area ratio of C−C and oxygen containing carbon components for the XPS spectrum of each sample. The area ratio of oxygen containing carbon increases with time. This is because oxygen containing carbon is known to easily bond to the surface of TiO_2 substrate[125,126]. SnS on the other hand is expected to be bonded to the TiO_2 substrate only by Van der Waals force. As a result, it appears that oxygen containing organic molecules may accumulate on the TiO_2 surface over time and be preferentially adsorbed on the surface, which is supposed to be occupied by SnS molecules. With more oxygen containing hydrocarbon being present, the SnS cannot form an effective contact with the TiO_2 substrate, and as a result, the performance of the as-fabricated solar devices degrades with time. One-week-long soaking time allows hydrocarbon contamination to completely take over the TiO_2 substrate that is supposed to be occupied by the SnS molecules. Hence, few SnS molecules are bonded to the TiO_2 substrate. It also explains why the Sn *3d* peak cannot be observed in the XPS spectrum for the 1-week-soaked sample.

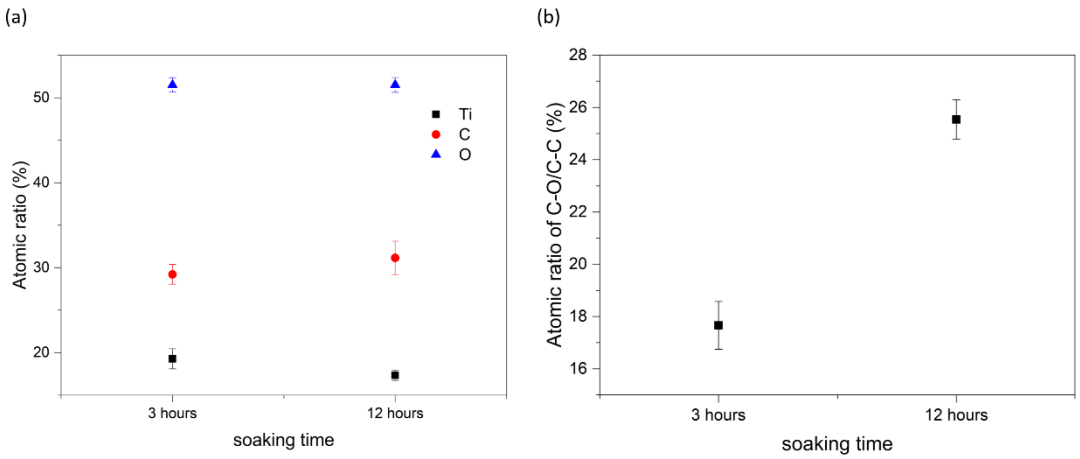

Figure 53 (a) Approximate atomic ratio of Ti, C and O calculated. (b) Approximate area ratio between the oxygen containing carbon component and the C-C component.

5.3 Summary

In summary, the results of the *J-V* measurement and analysis appear to suggest that a longer soaking time leads to a worse performance in terms of cell efficiency. It is found that the band alignment of the SnS and anatase TiO_2 is amenable to sensitise TiO_2. Based on the *J-V* measurement and PES analysis, there are two possible reasons for the negative effect of soaking time on the performance of the as-fabricated solar devices. Firstly, oxygen containing carbon contamination may accumulate on the surface of the TiO_2 substrate over time, due to its better affinity to the TiO_2 substrate. Secondly, XPS analysis of the samples where Sn is found at the surface shows a lack of S *2p* in the spectra, which may indicate significant oxidation of the SnS nanosheets.

6 The stability of MoS_2 and WS_2 nanosheets

In the previous chapter, it was found that the solvent appeared to prevent adsorption of SnS sheets onto the TiO_2 surface. Furthermore, it appears that significant oxidation of the SnS occurs. In order to investigate this further, we turned to the TMDCs, MoS_2 and WS_2, to investigate the effect of solvent on dip-coating and the possible oxidation of the TMDC materials deposited on TiO_2.

6.1 Results and analysis

Firstly, to investigate the effect of solvent on the dip-coating of WS_2 and MoS_2, four mesoporous TiO_2 layer thin films on ITO glass substrate were prepared and soaked in WS_2 NMP, WS_2 IPA, MoS_2 NMP, and MoS_2 IPA suspensions for 20 hours. The four soaked samples were characterised using XPS. All four XPS survey spectra are displayed in Figure 54. Each spectrum has been calibrated in the BE scale by adjusting the position of C *1s* line to BE 284.8 eV. The primary region of each element is defined with green shading and labelled with the core level involved, in order to measure the approximate atomic ratio of each element in each sample. It is seen in Figure 54 that C *1s* and O *1s* lines are present in the XPS spectra of all four samples. The intensities of W $4f_{7/2}$ and W $4f_{5/2}$ peaks in the spectrum of the WS_2 NMP sample are much higher than the ones in the spectrum of the WS_2 IPA sample. Similarly, the intensities of Mo $3d_{5/2}$ and Mo $3d_{3/2}$ peaks in the spectrum of the MoS_2 NMP sample are higher than the ones in the spectrum of the MoS_2 IPA sample. In Figure 54(b) and (d), the S *2p* line cannot be resolved for spectra recorded from either of the suspensions using IPA as solvent. It should also be noted that for the MoS_2/NMP sample, the Ti *2p* signal cannot be observed, suggesting a thick overlayer of > 30 nm has been deposited.

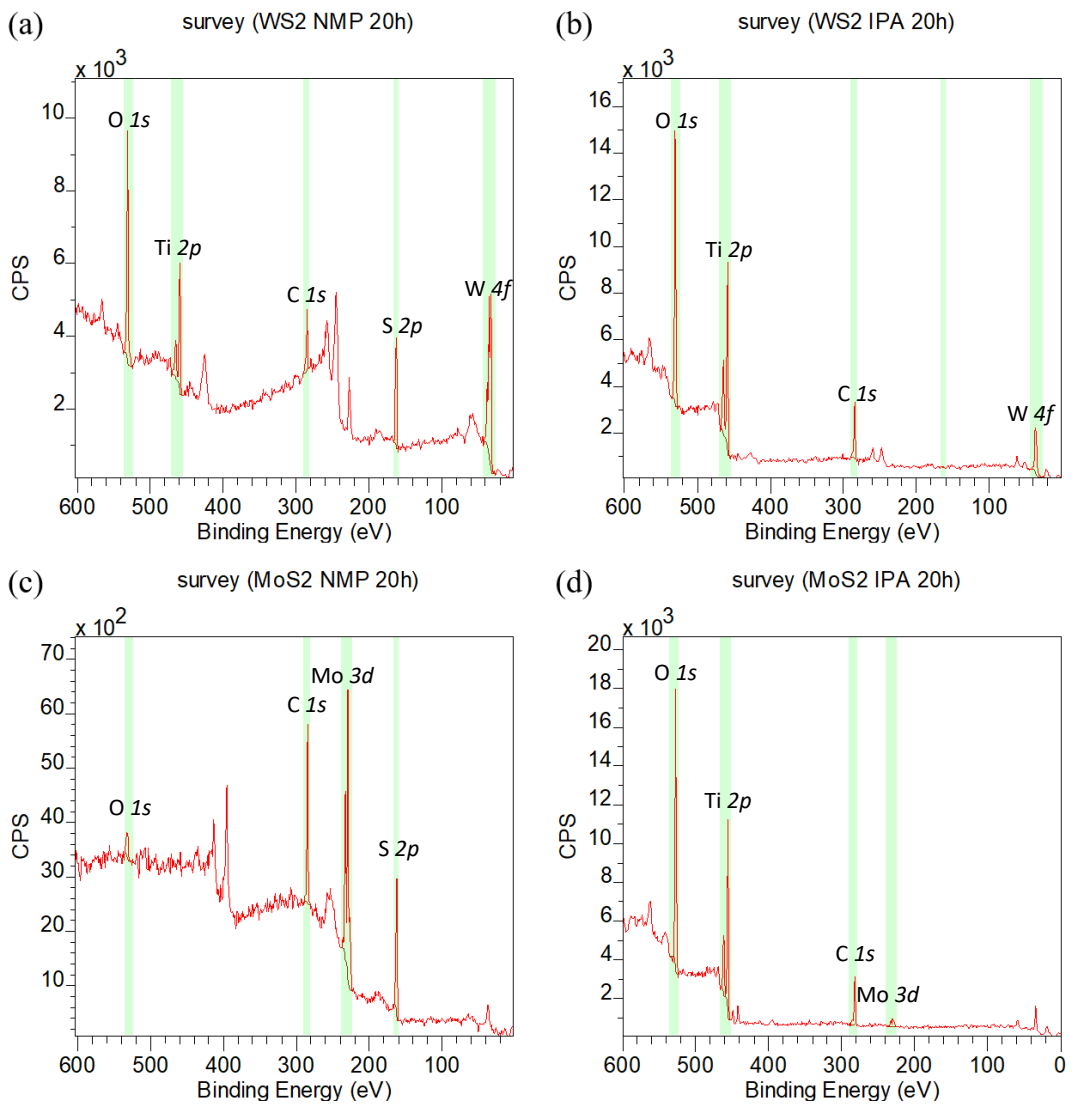

Figure 54 XPS survey spectra of (a) WS_2 NMP suspension, (b) WS_2 IPA suspension, (c) MoS_2 NMP suspension, and (d) MoS_2 IPA suspension. The primary XPS region of each element are defined and labelled with light green colour for measuring the atomic ratio of each element.

The approximate atomic ratio of each element (excluding carbon and oxygen) for each sample has been calculated from the survey spectra and the results are summarised in Figure 55. Figure 55 shows that, the atomic ratios of W or Mo are close to each other for both samples based on the same solvent, and so are the ratios of S and Ti. Additionally, it is noticed that, for the samples based on the NMP solvent, the atomic ratios of W or Mo are larger relative to the amount of Ti, than for the samples based on the IPA solvent, where the atomic ratios of W or Mo are lower than Ti. It can be inferred from the observation above that the suspensions using NMP as solvent allows a better

deposition of WS_2 and MoS_2 on the mesoporous TiO_2 substrate than the suspensions using IPA as solvent.

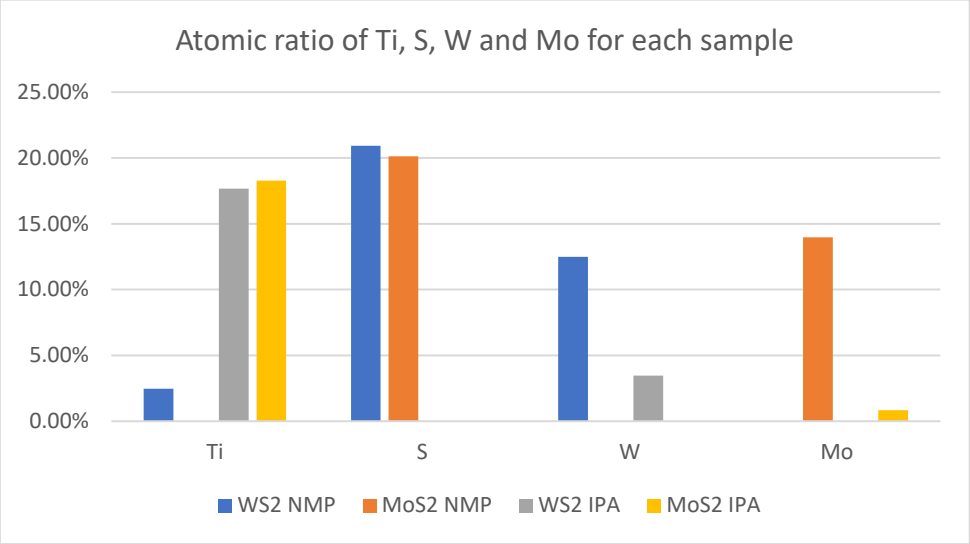

Figure 55 Approximate atomic ratio of Ti, S and W or Mo for each sample measured according to XPS survey spectra.

Narrow scans for W *4d*, Mo *3d* and S *2p* regions were carried out for further analysis. The spectra of each sample were calibrated on the BE scale by adjusting the C *1s* peak to BE 284.8 eV. Figure 56(a) and (b) show the narrow scan spectra and fitting results of W *4d* region and S *2p* region for the two WS_2 samples. In the NMP sample, the W $4d_{5/2}$ peak lies at a BE of ~ 244.5 eV[127] corresponding to W^{4+}, whereas in the IPA sample, it is at a BE of about 247.5 eV, which corresponds to W^{6+}.[128] The change observed in oxidation state suggests that oxidation has occurred on the WS_2 IPA sample, resulting in conversion of WS_2 to $W(SO_4)_3$ or WO_3. This is supported by the S *2p* spectrum in Figure 56(b) which shows the presence of a significant amount of sulfate, resulting in a spin-orbit split peak with the $2p_{3/2}$ peak at a binding energy of 168.5 eV. It is possible that the WS_2 IPA sample is oxidised in ambient atmosphere as WS_2 is very sensitive to oxygen and can be oxidised in air to form tungsten sulfate[129]. In the W *4d* spectrum of the WS_2 NMP sample, a minor peak representing S *2s* component is identified at a BE of ~ 226.5 eV[130], but the S *2s* peak cannot be observed in the spectrum

of the WS_2 IPA sample. For sulfate, the S *2s* peak is expected to be around 233 eV[131–134], but of course, the photoionisation cross-section of the S *2s* level is much lower than the S *2p*. The atomic ratio of W: S is calculated according to the fitting results shown in Figure 56(a) and (b). The calculation shows that for the WS_2 NMP sample, the atomic ratio of W: S is 1: 1.91, which is close enough to the theoretical stoichiometric number. For the WS_2 IPA sample, the atomic ratio of W: S (sulfur amount in total) is 1: 0.14. This low ratio might also suggest that some oxidation of WS_2 to WO_3 for the WS_2 IPA sample.

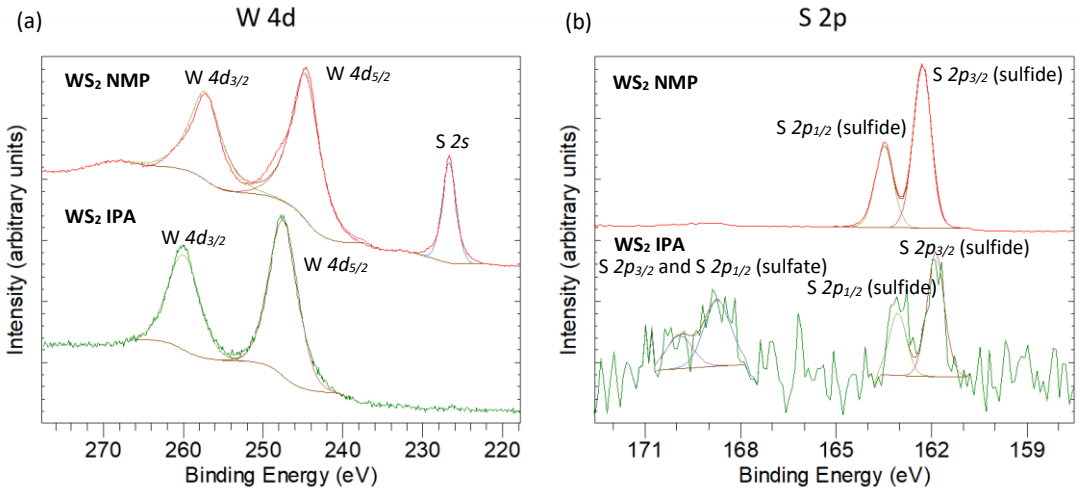

Figure 56 (a) Narrow scan spectra of WS_2 samples for W *4d* region and the corresponding fitted curves. (b) Narrow scan spectra of WS_2 samples for S *2p* region and the corresponding fitted curves. The component each peak or region represents is labelled next to it.

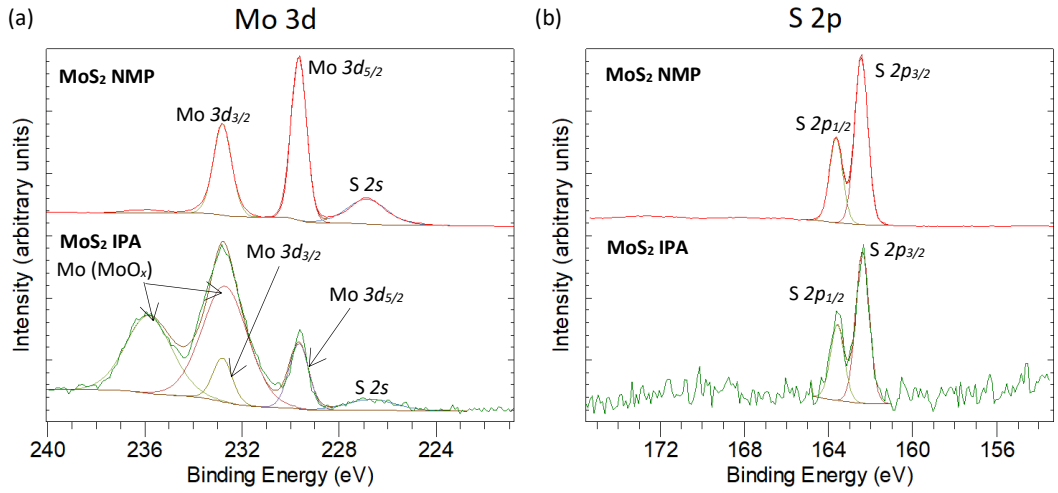

Figure 57 (a) Narrow scan spectra of MoS_2 samples for Mo *3d* region and the corresponding fitted curves. (b) Narrow scan spectra of MoS_2 IPA sample for S *2p* region and the corresponding fitted

curves. The component each peak or region represents is labelled next to the peak or region or with an arrow pointing to the corresponding fitting curve.

The narrow scan spectra and fitting results of Mo *3d* region and S *2p* region for the two MoS_2 samples are displayed in Figure 57. The fitted curves of the Mo narrow scan spectrum show that the Mo $3d_{5/2}$ peaks lie at a BE of ~ 233 eV for MoS_2 NMP and MoS_2 IPA samples[135]. The two broad Mo *3d* peaks observed at BEs of ~233 and ~236 eV may correspond to Mo species with Mo(V)[136] and Mo(VI)[137]. The S *2s* peak is observed in the spectra of both MoS_2 NMP and MoS_2 IPA samples at BE ~ 226.5 eV, next to the Mo $3d_{5/2}$ peak. This is contrary to the result for the WS_2 IPA sample, since the S *2s* line is clearly present in the spectrum of the MoS_2 IPA sample. The atomic ratio of Mo: S is calculated according to the fitting results shown in Figure 57(a) and (b). For the MoS_2 NMP sample, the atomic ratio between Mo: S is 1: 2.22. For the MoS_2 IPA sample, the atomic ratio between Mo: S is 1: 0.59. This is again suggesting a loss of S for IPA suspended sample. However, it is clear that the loss of sulfur is not as severe as observed for the WS_2 IPA sample, yet there is no evidence of the existence of sulfate at the surface. It is known that MoS_2 corrosion is an issue, especially in photocatalytic systems. It is also well-known that TiO_2 is a photocatalyst material. The mechanism of TiO_2 photocatalytic activity is thought to involve O· radical production and OH·. Recent work suggests that oxidation of MoS_2 occurs at the edges of sheets through hydroxyl formation[138]. It is not surprising that in IPA, TiO_2 functionalised with MoS_2 produces oxidising species. The 2D MoS_2 structure is particularly susceptible to oxidation, since there will be a large proportion of edge sites for hydroxyl species to attach to. This is perhaps the reason for the sulfur loss in the MoS_2 IPA sample.

In order to further investigate the degradation of MoS_2 IPA in air, we dropped MoS_2 IPA suspensions with the same volume on two ITO glass substrates and allowed them to dry in the air for 5 minutes. They were then left being exposed in the air for 20 hours

and 72 hours, respectively. The samples after exposure in air were analysed using XPS. The XPS spectra obtained and the corresponding fitting results are shown in Figure 58. As shown in the S *2p* spectra of the two samples, the S $2p_{3/2}$ (sulfide) peak and S $2p_{3/2}$ (sulfate) peak are identified at BE ~ 162.4 eV[139] and ~ 169.0 eV[135], respectively. During the fitting process, the doublet splitting was set to be 1.19 eV according to the literature[140]. The presence of an obvious sulfate component indicates that oxidation of the material has occurred during the exposure of MoS_2 to air. This sulfate formation is at odds with what is seen on the MoS_2-TiO_2-ITO sample. The reason for this is not clear, but it may be that, in the presence of the large surface area TiO_2 photocatalyst, the oxidation of MoS_2 to MoO_3 or polymolybdate complexes is very rapid. The measured atomic ratios of sulfide: sulfate are shown in Figure 59. It can be seen from Figure 59 that the atomic ratios of S *2p* (sulfide) component and S *2p* (sulfate) component vary dramatically as the exposure time is extended from 20 hours to 72 hours. The percentage of S *2p* (sulfate) component increases from 42.1% to 71.5% over this time. The variation of the atomic ratios of the two components indicates that MoS_2 will degrade with time and transform to sulfate when exposed to air. If we assume the initial atomic ratio of the S *2p* (sulfide) is 100%, the oxidation rate of sulfide can be qualitatively estimated. The atomic ratio of S *2p* (sulfide) at different exposure time is manifested in Figure 60. Within the first 20 hours, about 40% of all sulfur element in sulfide were oxidised in air, while about 30% more of all the sulfur atoms were oxidised within the next 52 hours, which implies a higher degradation rate of sulfide at the beginning of exposure to air.

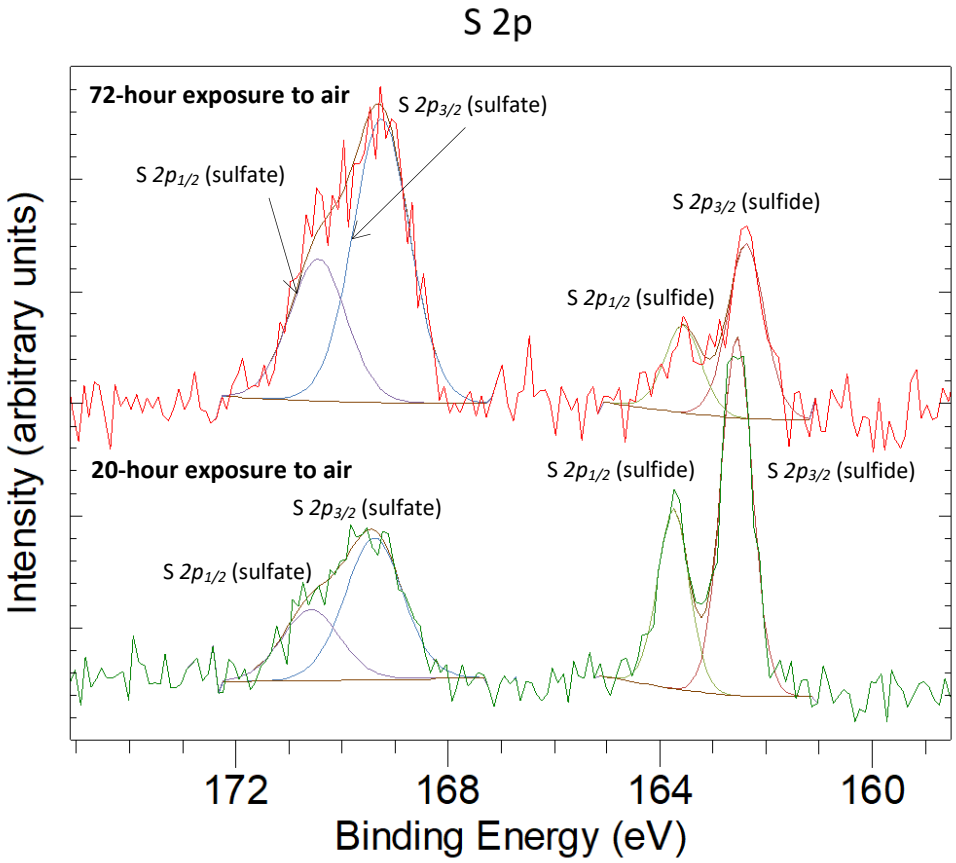

Figure 58 The XPS curves and the corresponding fitting results of S *2p* region of the 20-hour-exposed MoS_2 sample. The XPS curves and the corresponding fitting results of S *2p* region of the 72-hour-exposed MoS_2 sample. The components of each peak are labelled next to the peak or with an arrow.

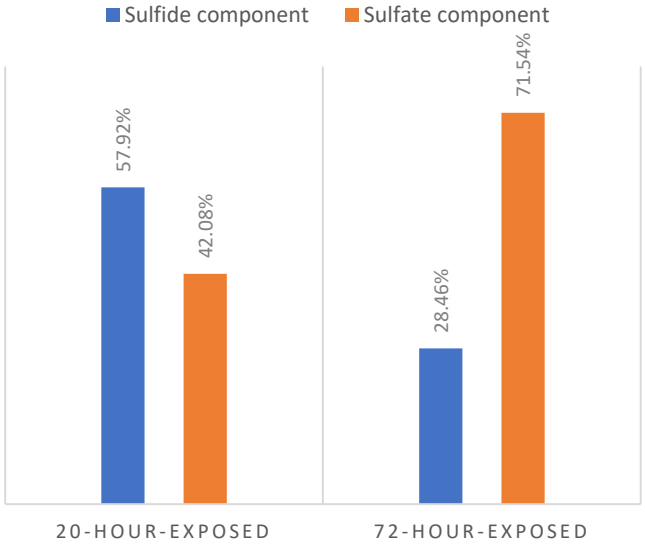

Figure 59 Area ratio of sulfide component and sulfate component calculated from the XPS fitting results of each sample.

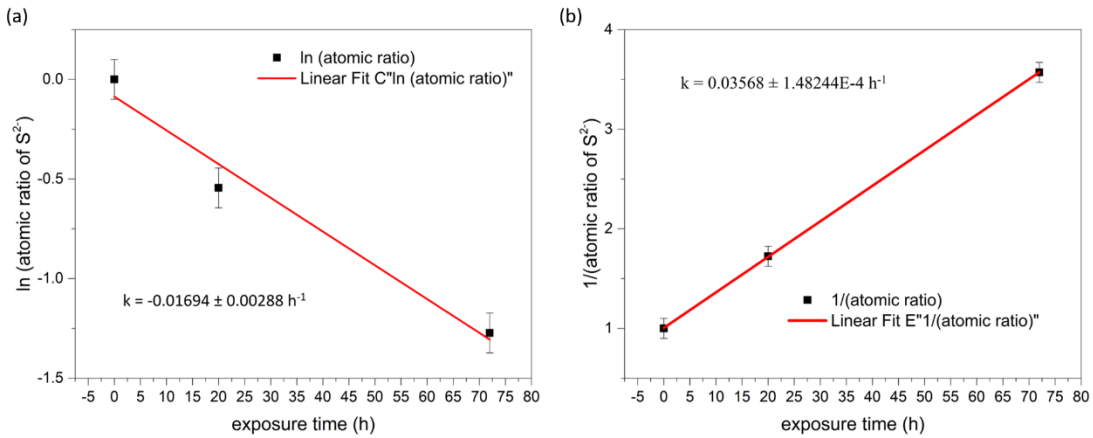

Figure 60 (a) Plot of ln(at% of S^{2-}) as a function of exposure time giving a slope of −0.01694 and therefore a rate constant of −0.01694 h^{-1}. (b) Plot of 1/(at% of S^{2-}) as a function of exposure time giving a slope of 0.03568 and therefore a rate constant of 0.03568 h^{-1}.

The XPS analysis of the two samples being exposed in air for 20 hours and 72 hours shows that degradation of MoS_2 will occur when it is in contact with oxygen containing environment. Assuming the oxidation of MoS_2 in an excess of oxygen is a first order reaction, a graph of ln(at% of S^{2-}) versus exposure time in air can be plotted and k calculated from the gradient is shown in Figure 60(a). The rate constant for the oxidation of MoS_2 is calculated from the graph to be $k = -0.01694 \pm 0.00288\ h^{-1}$. Figure 60(b) shows the graph of $1/c(S^{2-})$ versus exposure time for a second order reaction. The gradient of the graph gives a rate constant of 0.03568 h^{-1}. However, it is noted that the experiment is limited by the small number of data points in the plot, which makes it difficult to determine the rate order or rate constant. We noted that in the fabrication process of TMDC based solar cells, exposure of TMDC materials to oxygen, oxidising agents and certain solvents should be avoided to prolong the lifetime of TMDC materials.

6.2 Summary

To summarise, the XPS analysis of the deposition of WS_2 and MoS_2 based on different solvents indicates that the choice of solvent and substrate are important, since they have an impact on the oxidation of WS_2 and MoS_2. The WS_2 and MoS_2 materials deposited

using IPA as the solvent are more oxidised than those deposited using NMP. The results also indicate that, there is little difference between W and Mo regardless of solvent. The investigation of the air-induced oxidation of MoS_2/IPA deposited on ITO and TiO_2 suggests MoS_2 can be easily oxidised to molybdenum sulfates and oxides, and as the exposure time extends, more molybdenum sulfide will transform to sulfates. We believe the mechanism proposed by Afanasiev and Lorentz involving hydroxylation of the edge sites of MoS_2[138] forming first $Mo(SO_4)_x$ and then Mo oxides is in agreement with our observations. IPA and TiO_2 appear to accelerate the degradation process compared to NMP and ITO. This may imply that TiO_2 is not a suitable substrate for the photocatalytic and photovoltaic application of MoS_2 and is of interest for further study. Hence, in the fabrication process of TMDC based solar cells, exposure of TMDC materials to oxygen and other oxidising agents should be avoided to keep the quality of the TMDC materials.

When MoS_2 is deposited on ITO glass substrate, sulfate is formed, whereas on TiO_2 we never see sulfate. This might suggest that TiO_2 catalyses the oxidation process, resulting in formation of MoO_x species.

7 Conclusion and future work

7.1 Conclusion

We investigated the deposition of SnS on mesoporous TiO_2 substrate by soaking the TiO_2 substrate in the SnS suspension. The solar cells assembled based on the SnS/mesoporous TiO_2 structure have very low power conversion efficiency. Compared to the 12-hour and 1-week soaked solar cells, the 3-hour soaked solar cell, where the maximum PCE 0.03% was reached, has a better performance. A shorter soaking time allows less carbohydrate contamination to bind with the TiO_2 surface, thus, the charge

carrier transport between the SnS layer and the TiO_2 substrate are less hindered by the insulator carbohydrate contamination. As a result, the 3-hour soaked solar cell exhibits the best performance among the three samples. There are several factors leading to the general low PCE obtained on the three as-fabricated solar cells. The first factor is the poor light absorption. Though SnS has a small bandgap and it is supposed to enhance the light absorption, the SnS layer deposited is so thin that it doesn't absorb enough photons and thus generate enough electron-hole pairs. The second factor is the ineffective contact between SnS molecules and the TiO_2 substrate. Using synchrotron radiation-based valence band photoemission we determined the band alignment of the SnS-TiO_2 interface. We found that a type II offset exists between the energy levels of SnS and anatase, which indicates that effective charge carrier transport should occur between the light absorber and the TiO_2 substrate. Inorganic TMC materials such as SnS, however, can bond with TiO_2 only through Van der Waals interaction rather than being bonded to the TiO_2 substrate chemically like organic dyes. As a result, the charge carrier transport between the SnS light absorber and TiO_2 substrate is likely to be less effective than it is between organic dyes and the TiO_2 buffer layer. Additionally, the hydrocarbon contamination appears to adsorb preferentially on the TiO_2 substrate compared to the SnS molecules. This may be another factor leading to the low PCE observed.

The effect of solvent choice on the dip-coating of WS_2 and MoS_2 was also studied. The result of the XPS analysis shows that, the dip-coating based on NMP solvent allows a better deposition of TMDC materials on the surface of TiO_2 than IPA, as NMP does not only allow more TMDC molecules to be loaded on the TiO_2 substrate but also results in less oxidation of WS_2 and MoS_2 than in IPA. It appears that TiO_2 can catalyse the oxidation of these 2D TMCs and that the solvent can accelerate the process.

The degradation of TMDC material without TiO_2 was also investigated. The XPS analysis indicates that sulfur in TMDC material is oxidised when exposed to air, and longer exposure will lead to a higher proportion of oxidised sulfur to all sulfur atoms. In the fabrication process of TMDC based solar cells, exposure of TMDC to air must be avoided in order to maintain the properties of TMDC material.

We found a rate constant of $-0.017\ h^{-1}$ assuming first order reaction kinetics or $0.036\ h^{-1}$ assuming second order reaction kinetics, but we also noted that only very few data points obtained.

7.2 Future work

The reason for the low PCE still needs to be further investigated. UV-Vis spectroscopy could be used to find out if the poor light absorption is the predominant reason which leads to the low PCE obtained. If it is the case, the performance of the cell could be improved by producing thicker SnS light absorber layer. On the other hand, the effectiveness of the contact between SnS layer and TiO_2 substrate also requires a further analysis by SEM images of the cross section of the sample. If the SEM images show that the adhesion between the SnS layer and TiO_2 substrate is ineffective, an annealing process in the atmosphere of H_2S or Ar could be applied to create an effective adhesion between the two layers.

Based on some recent research, an annealing process in H_2S atmosphere can be a measure to control the oxidation of SnS material[41,141]. Therefore, a study on the effect of H_2S annealing process to the adhesion between the SnS layer and the TiO_2 substrate using PES can be interesting.

To investigate the degradation of TMDC materials in air and obtain a definitive rate constant and reaction order, the number of samples should be increased, and more

exposure times should be investigated. The effect of TiO_2 and the choice of solvent on oxidation rate is also worth further investigation as this may be important in the design of water splitting catalysts based on MoS_2 or WS_2 particularly.

8 References

1. Anderson, T. R., Hawkins, E. & Jones, P. D. CO_2, the greenhouse effect and global warming: from the pioneering work of Arrhenius and Callendar to today's Earth System Models. *Endeavour* **40**, 178–187 (2016).

2. Lu, Q., Yu, Y., Ma, Q., Chen, B. & Zhang, H. 2D Transition-Metal-Dichalcogenide-Nanosheet-Based Composites for Photocatalytic and Electrocatalytic Hydrogen Evolution Reactions. *Adv. Mater.* **28**, 1917–1933 (2016).

3. Rogner, H. Chapter 5: Energy Resources. in *Energy and the challenge of sustainability* (United Nations Development Programme, 2000).

4. Arons, A. B. & Peppard, M. B. Einstein's Proposal of the Photon Concept—a Translation of the Annalen der Physik Paper of 1905. *Am. J. Phys.* **33**, 367–374 (1965).

5. Latunussa, C. E. L., Ardente, F., Blengini, G. A. & Mancini, L. Life Cycle Assessment of an innovative recycling process for crystalline silicon photovoltaic panels. *Sol. Energy Mater. Sol. Cells* **156**, 101–111 (2016).

6. 3 Generations of Solar Cells: Solar Facts and Advice. Available at: http://www.solar-facts-and-advice.com/solar-cells.html. (Accessed: 5th January 2019)

7. Matthews, P. D., McNaughter, P. D., Lewis, D. J. & O'Brien, P. Shining a light on transition metal chalcogenides for sustainable photovoltaics. *Chem. Sci.* **8**, 4177–4187 (2017).

8. Rafati Rahimzadeh, M., Rafati Rahimzadeh, M., Kazemi, S. & Moghadamnia, A.-A. Cadmium toxicity and treatment: An update. *Casp. J. Intern. Med.* **8**, 135–145 (2017).

9. Di Mare, S. *et al.* SnS thin film solar cells: Perspectives and limitations. *Coatings* **7**, 34 (2017).

10. Singh, G. K. Solar power generation by PV (photovoltaic) technology: A review. *Energy* **53**, 1–13 (2013).

11. Markvart, T. & Castañer, L. Chapter I-1-A: Principles of solar cell operation. in *McEvoy's Handbook of Photovoltaics: Fundamentals and Applications* 3–28 (Elsevier Ltd, 2017). doi:10.1016/B978-0-12-809921-6.00001-X

12. Kitai, A. Chapter 1: Semiconductor Physics. in *Principles of Solar Cells, LEDs and Diodes: The role of the PN junction* 2–63 (John Wiley & Sons, Ltd, 2011). doi:10.1002/9781119974543

13. The P-N Junction. Available at: http://hyperphysics.phy-astr.gsu.edu/hbase/Solids/pnjun.html. (Accessed: 11th March 2019)

14. P N Junction Theory Behind P N Junction | Electrical4U. *https://www.electrical4u.com/* Available at: https://www.electrical4u.com/p-n-junction-theory-behind-p-n-junction/. (Accessed: 12th March 2019)

15. Solar Cell | Electrical4U. *https://www.electrical4u.com/* Available at: https://www.electrical4u.com/solar-cell/. (Accessed: 22nd January 2019)

16. Neville, R. C. Chapter 6: Solar Cell Configuration and Performance. in *Solar Energy Conversion* (Elsevier, 1995). doi:10.1016/B978-044489818-0/50006-5

17. Mahato, N., Ansari, M. O. & Cho, M. H. Production of Utilizable Energy from Renewable Resources: Mechanism, Machinery and Effect on Environment. *Adv. Mater. Res.* **1116**, 1–32 (2015).

18. Silicon Solar Cells. Available at: http://large.stanford.edu/courses/2015/ph240/zhao-a1/. (Accessed: 22nd January 2019)

19. Shockley, W. & Queisser, H. J. Detailed balance limit of efficiency of p-n junction solar cells. *J. Appl. Phys.* **32**, 510–519 (1961).

20. Kondepudi, D. K. & Prigogine, I. Chapter 11: Thermodynamics of Radiation. in *Modern thermodynamics : from heat engines to dissipative structures* 486 (Chichester: John Wiley, 1998).

21. Solanki, C. S. & Beaucarne, G. Advanced solar cell concepts. *Energy Sustain. Dev.* **11**, 17–23 (2007).

22. Rühle, S. Tabulated values of the Shockley-Queisser limit for single junction solar cells. *Sol. Energy* **130**, 139–147 (2016).

23. O'Regan, B. & Gratzel, M. A Low-Cost, High-Efficiency Solar-Cell Based on Dye-Sensitized Colloidal TiO_2 Films. *Nature* **353**, 737–740 (1991).

24. Gong, J., Sumathy, K., Qiao, Q. & Zhou, Z. Review on dye-sensitized solar cells (DSSCs): Advanced techniques and research trends. *Renew. Sustain. Energy Rev.* **68**, 234–246 (2017).

25. He, Z., Que, W., Xing, Y. & Liu, X. Reporting performance in MoS_2–TiO_2 bilayer and heterojunction films based dye-sensitized photovoltaic devices. *J. Alloys Compd.* **672**, 481–488 (2016).

26. SnS (Herzenbergite). Available at: https://www.pveducation.org/pvcdrom/materials/sns-herzenbergite. (Accessed: 2nd April 2019)

27. Mariano, A. N. & Chopra, K. L. Polymorphism in some IV-VI compounds induced by high pressure and thin-film epitaxial GROWTH. *Appl. Phys. Lett.* **10**, 282–284 (1967).

28. Brent, J. R. *et al.* Tin(II) Sulfide (SnS) Nanosheets by Liquid-Phase Exfoliation of Herzenbergite: IV-VI Main Group Two-Dimensional Atomic Crystals. *J. Am. Chem. Soc.* **137**, 12689–12696 (2015).

29. Gao, C., Shen, H., Wu, T., Zhang, L. & Jiang, F. Preparation and the growth mechanism of zinc blende structure tin sulfide films by successive ionic layer adsorption and reaction. *J. Cryst. Growth* **312**, 3009–3013 (2010).

30. Ray, S. C., Karanjai, M. K. & Dasgupta, D. Structure and photoconductive properties of dip-deposited SnS and SnS2thin films and their conversion to tin

dioxide by annealing in air. *Thin Solid Films* **350**, 72–78 (1999).

31. Reddy, N. K. & Reddy, K. T. R. SnS films for photovoltaic applications: Physical investigations on sprayed Sn_xS_y films. *Phys. B Condens. Matter* **368**, 25–31 (2005).

32. Schneikart, A., Schimper, H. J., Klein, A. & Jaegermann, W. Efficiency limitations of thermally evaporated thin-film SnS solar cells. *J. Phys. D. Appl. Phys.* **46**, 305109 (2013).

33. Reddy, B. P., Sekhar, M. C., Vattikuti, S. V. P., Suh, Y. & Park, S. H. Solution-based spin-coated tin sulfide thin films for photovoltaic and supercapacitor applications. *Mater. Res. Bull.* **103**, 13–18 (2018).

34. Hartman, K. *et al.* SnS thin-films by RF sputtering at room temperature. *Thin Solid Films* **519**, 7421–7424 (2011).

35. Nassary, M. M. Temperature dependence of the electrical conductivity, Hall effect and thermoelectric power of SnS single crystals. *J. Alloys Compd.* **398**, 21–25 (2005).

36. Miles, R. W., Ogah, O. E., Zoppi, G. & Forbes, I. Thermally evaporated thin films of SnS for application in solar cell devices. *Thin Solid Films* **517**, 4702–4705 (2009).

37. Calixto-Rodriguez, M. *et al.* Structural, optical, and electrical properties of tin sulfide thin films grown by spray pyrolysis. *Thin Solid Films* **517**, 2497–2499 (2009).

38. Tanuševski, A. & Poelman, D. Optical and photoconductive properties of SnS thin films prepared by electron beam evaporation. *Sol. Energy Mater. Sol. Cells* **80**, 297–303 (2003).

39. Turan, E., Kul, M., Aybek, A. S. & Zor, M. Structural and optical properties of SnS semiconductor films produced by chemical bath deposition. *J. Phys. D. Appl. Phys.* **42**, 245408 (2009).

40. Cheng, S., He, Y. & Chen, G. Structure and properties of SnS films prepared by electro-deposition in presence of EDTA. *Mater. Chem. Phys.* **110**, 449–453 (2008).

41. Sinsermsuksakul, P. *et al.* Overcoming Efficiency Limitations of SnS-Based Solar Cells. *Adv. Energy Mater.* **4**, 1–7 (2014).

42. Reddy, N. K. & Reddy, K. T. R. Growth of polycrystalline SnS films by spray pyrolysis. *Thin Solid Films* **325**, 4–6 (1998).

43. Ramakrishna Reddy, K. T., Koteswara Reddy, N. & Miles, R. W. Photovoltaic properties of SnS based solar cells. *Sol. Energy Mater. Sol. Cells* **90**, 3041–3046 (2006).

44. Avellaneda, D., Nair, M. T. S. & Nair, P. K. Photovoltaic structures using chemically deposited tin sulfide thin films. *Thin Solid Films* **517**, 2500–2502 (2009).

45. Guo, W., Shen, Y., Wu, M. & Ma, T. Highly efficient inorganic-organic

heterojunction solar cells based on SnS-sensitized spherical TiO_2 electrodes. *Chem. Commun.* **48**, 6133–6135 (2012).

46. Sinsermsuksakul, P. *et al.* Enhancing the efficiency of SnS solar cells via band-offset engineering with a zinc oxysulfide buffer layer. *Appl. Phys. Lett.* **102**, 053901 (2013).

47. Kawano, Y., Chantana, J. & Minemoto, T. Impact of growth temperature on the properties of SnS film prepared by thermal evaporation and its photovoltaic performance. *Curr. Appl. Phys.* **15**, 897–901 (2015).

48. Ristov, M., Sinadinovski, G., Grozdanov, I. & Mitreski, M. Chemical deposition of TIN(II) sulphide thin films. *Thin Solid Films* **173**, 53–58 (1989).

49. Burton, L. A. & Walsh, A. Band alignment in SnS thin-film solar cells: Possible origin of the low conversion efficiency. *Appl. Phys. Lett.* **102**, 132111 (2013).

50. Sinsermsuksakul, P., Heo, J., Noh, W., Hock, A. S. & Gordon, R. G. Atomic layer deposition of tin monosulfide thin films. *Adv. Energy Mater.* **1**, 1116–1125 (2011).

51. Nair, M. T. S. & Nair, P. K. Simplified chemical deposition technique for good quality SnS thin films. *Semicond. Sci. Technol.* **6**, 132 (1991).

52. Avellaneda, D., Delgado, G., Nair, M. T. S. & Nair, P. K. Structural and chemical transformations in SnS thin films used in chemically deposited photovoltaic cells. *Thin Solid Films* **515**, 5771–5776 (2007).

53. Gao, C. *et al.* Preparation of SnS films with zinc blende structure by successive ionic layer adsorption and reaction method. *Mater. Lett.* **64**, 2177–2179 (2010).

54. Wang, Y., Gong, H., Fan, B. & Hu, G. Photovoltaic Behavior of Nanocrystalline SnS/TiO_2. *J. Phys. Chem. C* **114**, 3256–3259 (2010).

55. Kang, J. yoon *et al.* Control of the microstructure of SnS photovoltaic absorber using a seed layer and its impact on the solar cell performance. *J. Alloys Compd.* **711**, 294–299 (2017).

56. Kalpana, S., Sampath Krishnan, S., Bhaskaran, A., Senthil, T. S. & Elangovan, S. V. Effect of chromium doping on structural, optical and photocatalytic properties of ZnO nanoparticles. *Optoelectron. Adv. Mater. Rapid Commun.* **12**, 353–359 (2018).

57. Ikuno, T. *et al.* SnS thin film solar cells with $Zn_{1-x}Mg_xO$ buffer layers. *Appl. Phys. Lett.* **102**, 193901 (2013).

58. Park, H. H. *et al.* Co-optimization of SnS absorber and Zn(O,S) buffer materials for improved solar cells. *Prog. Photovoltaics Res. Appl.* **23**, 901–908 (2015).

59. Steinmann, V. *et al.* 3.88% Efficient Tin Sulfide Solar Cells using Congruent Thermal Evaporation. *Adv. Mater.* **26**, 7488–7492 (2014).

60. Solar Panel Efficiency: What Panels Are Most Efficient? | EnergySage. Available at: https://news.energysage.com/what-are-the-most-efficient-solar-panels-on-the-market/. (Accessed: 11th February 2019)

61. Han, B. & Hu, Y. H. MoS_2 as a co-catalyst for photocatalytic hydrogen

production from water. *Energy Sci. Eng.* **4**, 285–304 (2016).

62. Pandey, K. *et al.* First step to investigate nature of electronic states and transport in flower-like MoS_2: Combining experimental studies with computational calculations. *Sci. Rep.* **6**, 32690 (2016).

63. Novoselov, K. S. *et al.* Electric field in atomically thin carbon films. *Science (80-.).* **306**, 666–669 (2004).

64. Li, X. & Zhu, H. Two-dimensional MoS_2: Properties, preparation, and applications. *J. Mater.* **1**, 33–44 (2015).

65. Li, H. *et al.* Single-Layer Semiconducting Nanosheets: High-Yield Preparation and Device Fabrication. *Angew. Chemie Int. Ed.* **50**, 11093–11097 (2011).

66. Coleman, J. N. *et al.* Two-dimensional nanosheets produced by liquid exfoliation of layered materials. *Science (80-.).* **331**, 568–571 (2011).

67. Lin, T.-W. *et al.* Synthesis of Large-Area MoS_2 Atomic Layers with Chemical Vapor Deposition . *Adv. Mater.* **24**, 2320–2325 (2012).

68. Yu, Y. *et al.* Controlled scalable synthesis of uniform, high-quality monolayer and few-layer MoS_2 films. *Sci. Rep.* **3**, 1866 (2013).

69. Zhan, Y., Liu, Z., Najmaei, S., Ajayan, P. M. & Lou, J. Large-area vapor-phase growth and characterization of MoS_2 atomic layers on a SiO_2 substrate. *Small* **8**, 966–971 (2012).

70. Lin, Y. C. *et al.* Wafer-scale MoS_2 thin layers prepared by MoO_3 sulfurization. *Nanoscale* **4**, 6637–6641 (2012).

71. Li, H. *et al.* Growth of Large-Area and Highly Crystalline MoS_2 Thin Layers on Insulating Substrates. *Nano Lett.* **12**, 1538–1544 (2012).

72. Aivazian, G. *et al.* Vapor–Solid Growth of High Optical Quality MoS_2 Monolayers with Near-Unity Valley Polarization. *ACS Nano* **7**, 2768–2772 (2013).

73. Hao, L. *et al.* Electrical and photovoltaic characteristics of MoS_2/Si p-n junctions. *J. Appl. Phys.* **117**, 114502 (2015).

74. Ganatra, R. & Zhang, Q. Few-layer MoS_2: A promising layered semiconductor. *ACS Nano* **8**, 4074–4099 (2014).

75. Mak, K. F., Lee, C., Hone, J., Shan, J. & Heinz, T. F. Atomically thin MoS_2: A new direct-gap semiconductor. *Phys. Rev. Lett.* **105**, 136805 (2010).

76. Bülbül, F., Efeoğlu, I. & Arslan, E. The effect of bias voltage and working pressure on S/Mo ratio at MoS_2-Ti composite films. *Appl. Surf. Sci.* **253**, 4415–4419 (2007).

77. Kim, S. K. & Cha, B. C. Deposition of CrN-MoS_2 thin films by D.C. magnetron sputtering. *Surf. Coatings Technol.* **188**–**189**, 174–178 (2004).

78. Late, D. J. *et al.* Pulsed laser-deposited MoS_2 thin films on W and Si: Field emission and photoresponse studies. *ACS Appl. Mater. Interfaces* **6**, 15881–15888 (2014).

79. Tsai, M.-L. *et al.* Monolayer MoS_2 Heterojunction Solar Cells. *ACS Nano* **8**, 8317–8322 (2014).

80. Du, T. *et al.* TiO2-based solar cells sensitized by chemical-bath-deposited few-layer MoS_2. *J. Power Sources* **275**, 943–949 (2015).

81. Theerthagiri, J. *et al.* Recent advances in MoS_2 nanostructured materials for energy and environmental applications – A review. *J. Solid State Chem.* **252**, 43–71 (2017).

82. Gusakova, J. *et al.* Electronic Properties of Bulk and Monolayer TMDs: Theoretical Study Within DFT Framework (GVJ-2e Method). *Phys. Status Solidi Appl. Mater. Sci.* **214**, 1700218 (2017).

83. Dongelmans, A. Superconductivity in multilayered WS_2 and preparation of BSCCO From multilayered flake to device. (University of Groningen, 2017).

84. Behura, S. *et al.* WS_2/Silicon Heterojunction Solar Cells: A CVD Process for the Fabrication of WS_2 Films on p-Si Substrates for Photovoltaic and Spectral Responses. *IEEE Nanotechnol. Mag.* **11**, 33–38 (2017).

85. Hertz, H. Ueber einen Einfluss des ultravioletten Lichtes auf die electrische Entladung. *Ann. Phys.* **267**, 983–1000 (1887).

86. Vickerman, J. C. & Gilmore, I. S. Electron Spectroscopy for Chemical Analysis. in *Surface Analysis* (John Wiley & Sons, Ltd, 2009).

87. Swinehart, D. F. The Beer-Lambert Law. *J. Chem. Educ.* **39**, 333–335 (1962).

88. Hüfner, S. Chapter 2: Core Levels and Final States. in *Photoelectron Spectroscopy* (Springer-Verlag Berlin Heidelberg GmbH, 2003).

89. Koopmans, T. Über die Zuordnung von Wellenfunktionen und Eigenwerten zu den Einzelnen Elektronen Eines Atoms. *Physica* **1**, 104–113 (1934).

90. Hu, Y. Two-dimensional (2D) Fuctional Molecular Networks. (University College London, 2016).

91. Moulder, J. F., Stickle, W. F., Sobol, P. E. & Bomben, K. D. Standard Spectra of the Elements: Carbon. in *Handbook of X-ray photoelectron spectroscopy: a reference book of standard spectra for identification and interpretation of XPS data* 261 (1992).

92. Franinović, M. X-ray Photoelectron Spectroscopy. (University of Ljubljana, 2012).

93. X-ray Photoelectron Spectroscopy (XPS) Reference Pages: Shake Up Structure. Available at: http://www.xpsfitting.com/2012/08/shake-up-structure.html. (Accessed: 14th February 2019)

94. Thermo Scientific XPS. X-ray Generation in XPS. Available at: https://xpssimplified.com/xray_generation.php. (Accessed: 15th February 2019)

95. Watts, J. F. X-ray photoelectron spectroscopy. *Vacuum* **45**, 653–671 (1994).

96. Xia, P. *et al.* Impact and Origin of Interface States in MOS Capacitor with Monolayer MoS_2 and HfO_2 High-k Dielectric. *Sci. Rep.* **7**, 1–9 (2017).

97. XPS: X-ray source. Available at: http://www.thermo.com.cn/article6417.html. (Accessed: 3rd October 2019)

98. Zhao, Z. Chapter 1: Synchrotron Light Sources. in *Synchrotron Radiation in Materials Science* 1–33 (Wiley-VCH, 2018).

99. How Diamond Works - Diamond Light Source. Available at: https://www.diamond.ac.uk/Home/About/How-Diamond-Works.html. (Accessed: 3rd October 2019)

100. Diamond Light Source. Available at: https://www.diamond.ac.uk/Instruments/Structures-and-Surfaces/I09.html. (Accessed: 20th March 2020)

101. Cross, Y. M. & Castle, J. E. The Relationship between Transmission Efficiencies in the FRR and FAT Modes of an Electron Spectrometer. *Jounal Electron Spectrosc. Relat. Phenom.* **22**, 53–60 (1981).

102. Alternative & renewable enrgy. Solar Cell I-V Characteristic and Solar I-V Curves. 1 (2017). Available at: http://www.alternative-energy-tutorials.com/energy-articles/solar-cell-i-v-characteristic.html. (Accessed: 22nd January 2019)

103. Emery, K. A. Solar simulators and I-V measurement methods. *Sol. Cells* **18**, 251–260 (1986).

104. Cuevas, A. The recombination parameter J_0. in *Energy Procedia* **55**, 53–62 (2014).

105. Levy, M. Y. & Honsberg, C. Rapid and precise calculations of energy and particle flux for detailed-balance photovoltaic applications. *Solid. State. Electron.* **50**, 1400–1405 (2006).

106. Baruch, P., De Vos, A., Landsberg, P. T. & Parrott, J. E. On some thermodynamic aspects of photovoltaic solar energy conversion. *Sol. Energy Mater. Sol. Cells* **36**, 201–222 (1995).

107. Sinton, R. A. & Cuevas, A. Contactless determination of current-voltage characteristics and minority-carrier lifetimes in semiconductors from quasi-steady-state photoconductance data. *Appl. Phys. Lett.* **69**, 2510–2512 (1996).

108. Solar Cell Efficiency | PVEducation. Available at: https://www.pveducation.org/pvcdrom/solar-cell-operation/solar-cell-efficiency. (Accessed: 24th January 2019)

109. Solar Performance and Efficiency | Department of Energy. Available at: https://www.energy.gov/eere/solar/articles/solar-performance-and-efficiency. (Accessed: 24th January 2019)

110. Chen, Q. *et al.* A one-step laser process for rapid manufacture of mesoscopic perovskite solar cells prepared under high relative humidity. *Sustain. Energy Fuels* **2**, 1216–1224 (2018).

111. Hawash, Z., Ono, L. K. & Qi, Y. Recent Advances in Spiro-MeOTAD Hole Transport Material and Its Applications in Organic–Inorganic Halide Perovskite Solar Cells. *Adv. Mater. Interfaces* **5**, 1700623 (2017).

112. Kavan, L., Rathouský, J., Grätzel, M., Shklover, V. & Zukal, A. Surfactant-Templated TiO_2 (Anatase): Characteristic Features of Lithium Insertion Electrochemistry in Organized Nanostructures. *J. Phys. Chem. B* **104**, 12012–12020 (2000).

113. Rödel, T. C. *et al.* Engineering two-dimensional electron gases at the (001) and (101) surfaces of TiO_2 anatase using light. *Phys. Rev. B - Condens. Matter Mater. Phys.* **92**, 41106 (2015).

114. Burke, A. R. *et al.* Ignition mechanism of the titanium–boron pyrotechnic mixture. *Surf. Interface Anal.* **11**, 353–358 (1988).

115. Morgan, W. E. & Van Wazer, J. R. Binding energy shifts in the X-ray photoelectron spectra of a series of related group IV-a compounds. *J. Phys. Chem.* **77**, 964–969 (1973).

116. Cheng, C. H. *et al.* Catalytically solid-phase self-organization of nanoporous SnS with optical depolarizability. *Nanoscale* **8**, 4579–4587 (2016).

117. XPS Interpretation of Sodium. Available at: https://xpssimplified.com/elements/sodium.php. (Accessed: 8th April 2019)

118. XPS Interpretation of Sulfur. Available at: https://xpssimplified.com/elements/sulfur.php. (Accessed: 9th April 2019)

119. De Kergommeaux, A. *et al.* Surface oxidation of tin chalcogenide nanocrystals revealed by 119Sn-Mössbauer spectroscopy. *J. Am. Chem. Soc.* **134**, 11659–11666 (2012).

120. XPS Interpretation of Titanium. Available at: https://xpssimplified.com/elements/titanium.php. (Accessed: 9th April 2019)

121. Bharti, B., Kumar, S., Lee, H. N. & Kumar, R. Formation of oxygen vacancies and Ti^{3+} state in TiO_2 thin film and enhanced optical properties by air plasma treatment. *Sci. Rep.* **6**, 32355 (2016).

122. Szörényi, T., Laude, L. D., Bertóti, I., Kántor, Z. & Geretovszky, Z. Excimer laser processing of indium-tin-oxide films: An optical investigation. *J. Appl. Phys.* **78**, 6211–6219 (1995).

123. Ke, J. C. R. *et al.* Ambient-air-stable inorganic Cs_2SnI_6 double perovskite thin films: Via aerosol-assisted chemical vapour deposition. *J. Mater. Chem. A* **6**, 11205–11214 (2018).

124. Jackman, M. J., Thomas, A. G. & Muryn, C. Photoelectron spectroscopy study of stoichiometric and reduced anatase TiO<inf>2</inf>(101) surfaces: The effect of subsurface defects on water adsorption at near-ambient pressures. *J. Phys. Chem. C* **119**, 13682–13690 (2015).

125. Thomas, A. G. & Syres, K. L. Adsorption of organic molecules on rutile TiO_2 and anatase TiO_2 single crystal surfaces. *Chem. Soc. Rev.* **41**, 4207–4217 (2012).

126. Köppen, S. & Langel, W. Adsorption of small organic molecules on anatase and rutile surfaces: a theoretical study. *Phys. Chem. Chem. Phys.* **10**, 1907–1915 (2008).

127. Ansari, M. A., Chandrasekaran, J. & Sarkar, S. One Pot Synthesis of Dinuclear Tungsten(V) Compounds Containing $[W_2XY(\mu\text{-}S)_2]^{2+}$ (X=O,S; Y=O,S) Cores by Thermally Induced Internal Electron-Transfer Processes . *Bull. Chem. Soc. Jpn.* **61**, 2265–2267 (2006).

128. Sarma, D. D. & Rao, C. N. R. XPES studies of oxides of 2nd row and 3rd row transition-metals including rare-earths. *J. Electron Spectros. Relat. Phenomena* **20**, 25–45 (1980).

129. Kang, K. *et al.* Graphene-Assisted Antioxidation of Tungsten Disulfide Monolayers: Substrate and Electric-Field Effect. *Adv. Mater.* **29**, 1603898 (2017).

130. Turner, N. H. & Single, A. M. Determination of peak positions and areas from wide-scan XPS spectra. *Surf. Interface Anal.* **15**, 215–222 (1990).

131. Strohmeier, B. R. & Hercules, D. M. Surface spectroscopic characterization Mn/Al_2O_3 catalysts. *J. Phys. Chem.* **88**, 4922–4929 (1984).

132. Zingg, D. S. & Hercules, D. M. Electron spectroscopy for chemical analysis studies of lead sulfide oxidation. *J. Phys. Chem.* **82**, 1992–1995 (1978).

133. Chin, R. L. & Hercules, D. M. Surface spectroscopic characterization of cobalt-alumina catalysts. *J. Phys. Chem.* **86**, 360–367 (1982).

134. Strohmeier, B. R. & Hercules, D. M. Surface spectroscopic characterization of the interaction between zinc ions and γ-alumina. *J. Catal.* **86**, 266–279 (1984).

135. Suzuki, K., Soma, M., Onishi, T. & Tamaru, K. Reactivity of molybdenum disulfide surfaces studied by XPS. *J. Electron Spectros. Relat. Phenomena* **24**, 283–287 (1981).

136. Anwar, M., Hogarth, C. A. & Bulpett, R. Effect of substrate temperature and film thickness on the surface structure of some thin amorphous films of MoO_3 studied by X-ray photoelectron spectroscopy (ESCA). *J. Mater. Sci.* **24**, 3087–3090 (1989).

137. Choi, J. G. & Thompson, L. T. XPS study of as-prepared and reduced molybdenum oxides. *Appl. Surf. Sci.* **93**, 143–149 (1996).

138. Afanasiev, P. & Lorentz, C. Oxidation of Nanodispersed MoS_2 in Ambient Air: The Products and the Mechanistic Steps. *J. Phys. Chem. C* **123**, 7486–7494 (2019).

139. Korányi, T. I., Manninger, I., Paál, Z., Marks, O. & Gunter, J. R. Activation of Unsupported Co-Mo Catalysts in Thiophene Hydrodesulfurization. *Stud. Surf. Sci. Catal.* **116**, 422–439 (1989).

140. Peisert, H., Chassé, T., Streubel, P., Meisel, A. & Szargan, R. Relaxation energies in XPS and XAES of solid sulfur compounds. *J. Electron Spectros. Relat. Phenomena* **68**, 321–328 (1994).

141. Choi, H. *et al.* Fabrication of high crystalline SnS and SnS_2 thin films, and their switching device characteristics. *Nanotechnology* **29**, 215201 (2018).